LUND UNIVERSITY

Simulations of cavitation - from the large vapour structures to the small bubble dynamics

Vallier, Aurélia

2013

[Link to publication](#)

Total number of authors:
1

Simulations of cavitation – from the large vapour structures to the small bubble dynamics

Aurélia Vallier

June 2013

Division of Fluid Mechanics
Department of Energy Sciences
Faculty of Engineering
Lund University
Box18
S-221 00 LUND
Sweden

Populärvetenskaplig sammanfattning

Mycket få människor omkring oss vet innebörden av ordet *kavitation*, förutom de som såg filmen "The Hunt for Red October" och kan relatera kavitation till Sean Connery i en ubåt. Kavitation motsvarar bildandet av bubblor, som kan likna kokande vatten i en kastrull. Men den uppstår inte på grund av en hög temperatur utan på grund av ett lågt tryck. Den finns i de flesta tekniska anläggningar som innehåller vätska i rörelse. Problemet med kavitation är dess negativa konsekvenser. Till exempel orsakar den oljud vilket inte är onskvärt för en ubåt. Den kan också leda till förstörelse av ytor, vilket inte är onskvärt i en vattenturbin.

Kavitation i vattenturbiner orsakar förändringar och instabilitet i strömningen, och implosion av bubblor. Detta resulterar i en minskning i effektivitet, vibrationer och erosion (skador på ytor). Kavitation kan undvikas om turbinen ställts tillräckligt låg, så att det statiska trycket är tillräckligt högt för att förhindra att vatten övergår till gasform. Men byggkostnaderna för en sådan låg inställning är mycket höga. Därför måste man hitta en kompromiss mellan motstridiga krav på en låg installationskostnad och undvikande av negativa effekter från kavitation.

Kavitation är mycket komplex. En stor mängd forskning har gjorts under de senaste 30 åren för att förbättra förståelsen för detta fenomen. För att få mer kunskap om kavitation i vattenturbiner, kan man använda sig av numeriska modeller. Genom att lösa lämpliga ekvationer kan man beskriva hur kavitation börjar och utvecklas. Det finns modeller för varje specifik företeelse. Dock är kavitationsmodellering fortfarande mycket utmanande eftersom fenomenet leder till snabba variationer av strömingsegenskaper och samspelet mellan vatten, ånga och gas. Ångan som bildas vid kavitation kan uppträda i varierande storlek och form, från mikroskopiska sfäriska bubblor, till stora sammanhängande strukturer. Dessutom är strömningen turbulent. Alla dessa egenskaper kräver lämpliga modeller för att exakt förutsäga kaviterande strömningar.

I detta arbete utförs beräkningar för att utvärdera resultaten av olika modeller. En ny flerskalig modell utvecklas och används på en kaviterande strömning kring en vingprofil. Den nya modellen omfattar både små sfäriska bubblor, stora icke-sfäriska ånga strukturer och övergången mellan dessa regimer. Det är mycket intressant att ha en modell som kan förutsäga hur dem minsta bubblorna transporteras till regioner med lågt statiskt tryck, där de växer och sen imploderar. Genom att mäta tryckvågen som släpps från bubblan, kan man förutse risken för att närliggande ytor ska skadas. Tack vare den förbättrade modellen, kan man förutse där kavitation orsakar skador. Denna kunskap kan i ett senare skede hjälpa till att utforma geometrier som minskar de negativa effekterna av kavitation. Särskild omsorg kan då tas, så att bubbelimplosionerna sker långt ifrån ytor. Detta skulle minimera skador på ytorna, och därmed minska underhållskostnaderna.

Abstract

Very few people around us know the meaning of the word *cavitation*, except from those who saw the movie *The Hunt for Red October* and can relate cavitation to Sean Connery in a submarine. Some of them know that it corresponds to the formation of bubbles, due to a pressure drop, and causes erosion and noise. However, cavitation is much more complex. A large amount of research work has been done over the last thirty years in order to improve the understanding of the interactions between the various physical processes involved.

The present work aims at gaining more knowledge about cavitation in water turbines. Some of the properties of cavitation at a water turbine runner blade are similar to those at a hydrofoil in a water test tunnel. Therefore, the overall purpose of this work is to improve the numerical models for cavitation inception and development on a hydrofoil. The focus of this thesis lies on numerical methodologies that include the broad range of cavity sizes, using appropriate models for each specific phenomenon.

The smallest bubbles, called nuclei, are tracked in the flow with the Discrete Bubble Model, and their dynamics is resolved with the Rayleigh-Plesset equation. This approach can predict how the nuclei are transported over a hydrofoil to regions of low static pressure, where they grow and either collapse or contribute to the formation of large-scale vapour cavities.

The large non-spherical structures are commonly modelled using the Volume-Of-Fluid method together with a mass transfer model for vaporisation and condensation. This approach predicts the development of the vapour cavity, such as its breakup and the shedding process observed experimentally in the context of cavitating hydrofoils.

The present work implements the above-mentioned models in the OpenFOAM C++ library, and performs simulations to assess the performance of the models. A new multi-scale model is developed, implemented and used on a cavitating hydrofoil. The multi-scale model includes both the small spherical bubbles, the large non-spherical vapour structures, and the transition between those regimes.

List of publications

This thesis is based on the following papers.

1. **Comparisons of numerical and experimental results for rising air bubbles.**
   Aurélia Vallier and Johan Revstedt.
   Submitted to Journal of Fluids.

2. **Modelling of bubble dynamics related to cavitation.**
   Aurélia Vallier, Johan Revstedt and Håkan Nilsson.
   Submitted to Computers and Fluids.

3. **Mass transfer cavitation model with variable density of nuclei.**
   Aurélia Vallier, Johan Revstedt and Håkan Nilsson.
   7th International Conference on Multiphase Flow, ICMF 2010, Tampa, Florida, 2010

4. **Numerical procedure for simulating the break-up of cavitation sheet.**
   Aurélia Vallier, Johan Revstedt and Håkan Nilsson.
   4th International meeting on Cavitation and Dynamic Problems in Hydraulic Machinery and Systems, Belgrade, Serbia, 2011.

5. **A new multi-scale approach for modelling cavitation on hydrofoils.**
   Aurélia Vallier, Johan Revstedt and Håkan Nilsson.
   Submitted to International Journal for Numerical Methods in Fluids.

Acknowledgements

Contents

Nomenclature

Roman symbols

C_{drag}	Drag coefficient $[-]$
C_{lift}	Lift coefficient $[-]$
c_0	Chord length [m]
D	Diameter [m]
F	Force $[\mathrm{kg\,m\,s^{-2}}]$
g	Gravitational constant $[\mathrm{m\,s^{-2}}]$
m	Mass [kg]
n	Unit normal vector $[-]$
n_{nuc}	Nuclei density $[\mathrm{m^{-3}}]$
p	Pressure $[\mathrm{kg\,m^{-1}\,s^{-2}}]$
R	Radius [m]
S	Source term $[\mathrm{kg\,m^{-2}\,s^{-2}}]$ or $[\mathrm{s^{-1}}]$
t	Time [s]
t	Unit tangential vector $[-]$
U	Velocity $[\mathrm{m\,s^{-1}}]$
V	Volume $[\mathrm{m^3}]$
x	Position [m]

Greek symbols

α	Liquid volume fraction $[-]$
η	Efficiency $[-]$
ϵ	Coefficient of restitution $[-]$
κ	Curvature $[\mathrm{m^{-1}}]$
μ	Dynamic viscosity $[\mathrm{kg\,m^{-1}\,s^{-1}}]$
ν	Kinematic viscosity $[\mathrm{m^2\,s^{-1}}]$
ρ	Density $[\mathrm{kg\,m^{-3}}]$
σ_{st}	Surface tension coefficient $[-]$
σ	Cavitation number $[-]$
θ	Angle $[-]$
τ	Stress tensor $[\mathrm{kg\,m^{-1}\,s^{-2}}]$

Subscripts

a	Acoustic wave
B	Bubble
E	Eulerian
g	Gas

l	Liquid
L	Lagrangian
nuc	Nuclei
v	Vapour
w	Wall

Chapter 1

Introduction

Cavitation in water turbines causes flow alterations and instabilities, and collapses of bubbles. This results in a drop in efficiency, vibration, erosion and noise. Cavitation can be avoided if the setting of the turbine (i.e. its location with respect to tailwater elevation) is sufficiently low, yielding a static pressure at the runner that is high enough to prevent evaporation. However, construction costs for such a low setting are very high. Therefore, the setting is a compromise between the conflicting demands of a low cost installation, and a few negative effects from cavitation.

A better knowledge of the cavitation phenomenon would help when designing geometries that reduce the negative effects of cavitation. Special care can be taken, such that the bubble collapse energy is reduced, or that the collapse occurs far away from surfaces. This would minimise the damages on the surfaces, and thus reduce the maintenance costs. Computational Fluid Dynamics (CFD) simulations is an alternative to prototype experiments in order to improve the understanding of how to avoid cavitation problems. CFD has been used, for example, to study the influence of modifications of the shape of the trailing edge, the runner or the curvature of the blade by Göde [20], Zobeiri et al [78], Ingvarsdottir et al. [31] and Mishima [48] respectively.

Several numerical cavitation models have recently been introduced in the literature and in general-purpose CFD codes. However, modelling cavitation is still very challenging since it involves the interactions between liquid, vapour and undissolved gas, and moreover rapid temporal and spatial variations of the flow properties. The cavities range in size from microscopic spherical bubbles, to large-scale coherent structures. Furthermore, the flow is turbulent, and highly dynamic and unstable. All these features require appropriate models in order to accurately predict cavitating flow.

Many of the cavitation properties found in a water turbine are similar to those at a hydrofoil in a water test tunnel. The numerical models for cavitation inception and development are thus in the present work evaluated for cavitation at a hydrofoil. The focus is on the mechanisms of sheet and cloud cavitation, and the transition between those phenomenon. A sheet cavity is a large attached structure which covers a part of the hydrofoil, while cloud cavitation corresponds to a large number of small bubbles being transported with the flow. The sheet cavity length may oscillate if the rear part is periodically detached from the cavity, and the detached part turns into a cloud of small bubbles. Therefore, the present work has a focus on including the broad range of cavity sizes, using appropriate models for each specific phenomenon.

The large-scale cavitation inception, development and break up is frequently modelled using the Volume-Of-Fluid (VOF) method, with a mass transfer model for the vaporisation and condensation [30, 41]. In the mass transfer model developed by Sauer and Schnerr [62], the vaporisation is governed by the number of cavitation nuclei per unit volume in the fluid. The cavitation inception is modelled by a linearized Rayleigh-Plesset equation for the rate of growth of the nuclei. This approach successfully predicts the attached sheet cavity, the re-entrant jet which breaks up the cavity, and the shedding process. The part of the cavity that breaks off is however transported downstream as a large coherent structure rather than a cloud of bubbles.

For the small bubbles, a more relevant approach is to use the Discrete Bubble Model (DBM) to track individual bubbles, and a Rayleigh-Plesset equation to resolve the bubble dynamics and model the collapse of individual bubbles. With a four-way coupling method, the interaction between the bubbles is accounted for and the flow is affected by the presence of the bubbles.

In the present work, simulations are performed to assess the accuracy of the VOF model, with and without the mass transfer model of Sauer and Schnerr [62]. The mass transfer model is modified to account for a non-uniform distribution of nuclei, and simulations are performed to show the effects on the cavitation development. The DBM approach and the Rayleigh-Plesset equation are implemented, and used to investigate the sensitivity to the model parameters. Finally, a new multi-scale model is described, implemented and used on a cavitating hydrofoil. It models both the small spherical bubbles (using DBM and the Rayleigh-Plesset bubble dynamics model), the large non-spherical vapour structures (using VOF and the Sauer and Schnerr mass transfer model), and the transition between those regimes.

1.1 Objectives

The overall purpose of this work is to investigate and improve the numerical models that are suitable for modelling cavitation inception and development on a hydrofoil. The work is performed within the OpenFOAM C++ library [53]. The objectives of this thesis are therefore

- to evaluate the accuracy of the VOF model implemented in OpenFOAM,

- to investigate the behaviour of the predicted cavitation on a hydrofoil, using the VOF and Sauer and Schnerr mass transfer model in OpenFOAM,

- to implement and evaluate an improvement of the Sauer and Schnerr mass transfer model, taking into account a non-uniform nuclei distribution,

- to implement and investigate the behaviour of the Rayleigh-Plesset equation for bubble dynamics,

- to implement the DBM model, with four-way coupling and the Rayleigh-Plesset equation for bubble dynamics, and evaluate it under academic and realistic conditions,

- to implement an interaction between the VOF and DBM methodologies, and evaluate it in academic and realistic conditions.

1.2 Achievements

An overview of the main achievements of this work is given below.

- The **Volume-Of-Fluid (VOF)** method is assessed under non-cavitating conditions. Simulations are performed for deformable air bubbles in a water channel and for the breakup of a liquid jet. The results obtained with OpenFOAM are compared to experimental data and numerical results from an in-house code.

- The **Discrete Bubble Model (DBM)** approach is implemented and used under non-cavitating conditions to study the nuclei distribution at a hydrofoil.

- The **non-uniform nuclei distribution** is included in the mass transfer model of Sauer and Schnerr [62] in order to highlight its effects on the cavity shape and behaviour.

- The **Rayleigh-Plesset equation** is implemented to model the bubble dynamics. It is used to study the influence of the various model parameters on the results.

- The Discrete Bubble Model and the Rayleigh-Plesset equation are coupled into a **cavitation bubble model**. This model is used under cavitating condition in the case of nuclei travelling above a rectangular cylinder. The results include the trajectory of the bubbles, the evolution of their radius and the pressure wave emitted at collapse.

- A method is developed to **couple the VOF model and the Discrete Bubble model** under non-cavitating condition. It is based on the detection of the small bubbles and their conversion from the VOF description to the DBM approach. This model is implemented and used for modelling the breakup of large vapour bubbles by a liquid jet and the formation of small Lagrangian bubbles.

- A **multi-scale cavitation model** is developed and implemented. It uses

  - the VOF model with the mass transfer model of Sauer and Schnerr [62] to predict the large vapour structures,
  - the cavitation bubble model (the Discrete Bubble Model with the Rayleigh-Plesset equation) to predict the small spherical bubbles,
  - the model for the detection of the small bubbles and the conversion from the VOF description to the DBM approach,
  - a model for the conversion from the DBM approach to the VOF description.

This model is used in the case of a cavitating hydrofoil.

Chapter 2

Cavitation description

Cavitation involves many complex phenomena. Here some of them are discussed, such as the initiation (inception), the effect on efficiency, and the development which includes the forms commonly taken, the transition from sheet and cloud cavitation, and the dynamics of the smallest bubbles.

2.1 Cavitation inception

Cavitation inception can be described as the transition of a liquid into vapour due to a local reduction in static pressure. It requires the presence of **nuclei** in the fluid. Nuclei are small bubbles containing gas and vapour with diameters in the range of 10^{-3} to 10^{-1} mm. They are present in most technical systems where liquids are transported. If a nucleus enters a zone of low static pressure its radius grows. This may yield cavitation, which can take different forms, depending on the flow conditions.

During the process, only nuclei over a certain size are stimulated into growth. Indeed the behaviour of a single nucleus influences the flow, and therefore it also influences the behaviour and the stability of the nuclei nearby. Masato [42] studied the interaction between nuclei and concluded that when the largest nuclei affects the flow, the smaller ones do not grow anymore or do not even become unstable. Other authors, such as Arora et al. [2] , Brennen [8] and Morch [49] point out the nuclei content and size as crucial factors for cavitation inception.

Apart from the free stream nuclei mentioned above, nuclei can also exist on the surface. They are small attached cavities which develop on the **roughness** of the surface. Therefore the type of surface influences cavitation inception and development.

Another important parameter for cavitation inception is the **turbulence** because turbulence mixing may enhance the presence of nuclei in the turbulent boundary layer, and affect the form of the cavitation at inception. Franc [16] considered three different configurations to show that the type of the boundary layer affects the influence of the nuclei content and distribution on cavitation inception. In the case described in Figure 2.1(a), the laminar boundary layer separates from the wall and instabilities develop in the shear layer downstream separation. In that case, cavitation inception occurs in the core of the vortices, where the nuclei are trapped. In the case described in Figure 2.1(b), the separation of the laminar boundary layer is followed by the transition to turbulence and the reattachment of

the turbulent boundary layer to the wall. In that case, cavitation inception occurs in this small recirculation region, where the nuclei are trapped. In the case of an attached turbulent boundary layer, cavitation inception occurs as isolated bubbles, originating from the nuclei attached to the wall or transported by the fluid.

Figure 2.1: (a) The nuclei are trapped in the core of the vortices, downstream the laminar separation. (b) The nuclei are trapped in the small recirculation region, between the laminar separation and the reattachment of the turbulent boundary layer to the wall.

2.2   Cavitation effect on efficiency

Different types of cavitation can be visualised in experimental tests on a blade profile by varying the angle of attack and the cavitation number σ,

$$\sigma = \frac{p_\infty - p_v}{\frac{1}{2}\rho \mathbf{U}_\infty^2}.$$

where ρ is the fluid density, p_v is the vapour pressure, p_∞ and $\mathbf{U}_\infty$ are the pressure and the velocity at the inlet of the test section, far upstream from the blade.

Cavitation tests on hydraulic turbine models are performed to determine the values of a critical cavitation number in relation to the operating regime. Figure 2.2 shows a typical result obtained from a cavitation test. One can observe that when the cavitation number σ decreases, it doesn't have any influence on the efficiency until a critical value σ_c is reached. For a cavitation number in the range $[\sigma_c, \sigma_p]$, cavitation may appear but the turbine can sustain a certain amount of cavitation without consequences on the efficiency. Under the critical value however, a performance drop is observed. This is due to the strong instabilities generated by the large cavitating structures, as illustrated in Figure 2.3.
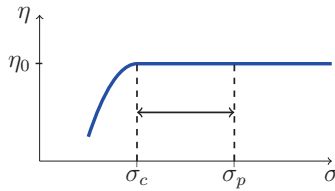

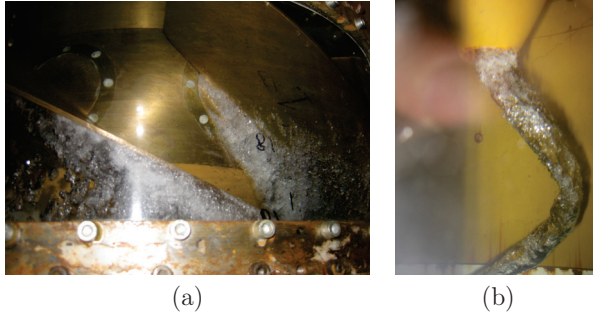**Figure 2.2:** Turbine efficiency as a function of cavitation number.

(a)   (b)

Figure 2.3: Large cavitating structures in a Kaplan turbine, at a cavitation number lower than the critical value σ_c. (a) Attached cavitation on the runner and the blade. (b) Hub vortex cavitation. (These personal photos are from a cavitation test which was conducted on the model of a Kaplan turbine at Vattenfall Research and Development, Älvkarleby.)

2.3   Cavitation development

Cavitation in a water turbine can take different forms as it develops from inception, e.g. bubble, sheet, cloud, tip vortex, hub vortex and tip clearance cavitation [16].

The different types of cavitation are briefly described below and illustrated in the pictures of Figure 2.4.

1. **Bubble cavitation** corresponds to bubbly structures convected by the flow. They appear in the region of low pressure as a result of a rapid growth of nuclei.

2. **Sheet cavitation** corresponds to an attached structure which covers a part of the blade. It is smooth and transparent. The closure region of the sheet cavity can be cloudy and turbulent.

3. **Cloud cavitation** corresponds to a foamy and unsteady structure. The cloud contains a large amount of bubbles which may collapse when they are advected by the flow.

4. **Tip and hub vortex cavitation** corresponds to a vaporisation of the vortex core.

5. **Tip clearance cavitation** takes place in the gap between the runner blades and the machine casing in the case of a Kaplan turbine. This type of cavitation is driven by the flow shear layer in this gap [26].

Transition from sheet to cloud cavitation

The attached sheet may develop into a cavitating cloud. Experimental and numerical studies highlight the following features [16].

- An adverse flow is initiated from the rear part of the cavity. It acts as a **re-entrant jet** that impacts and splits the cavity interface.
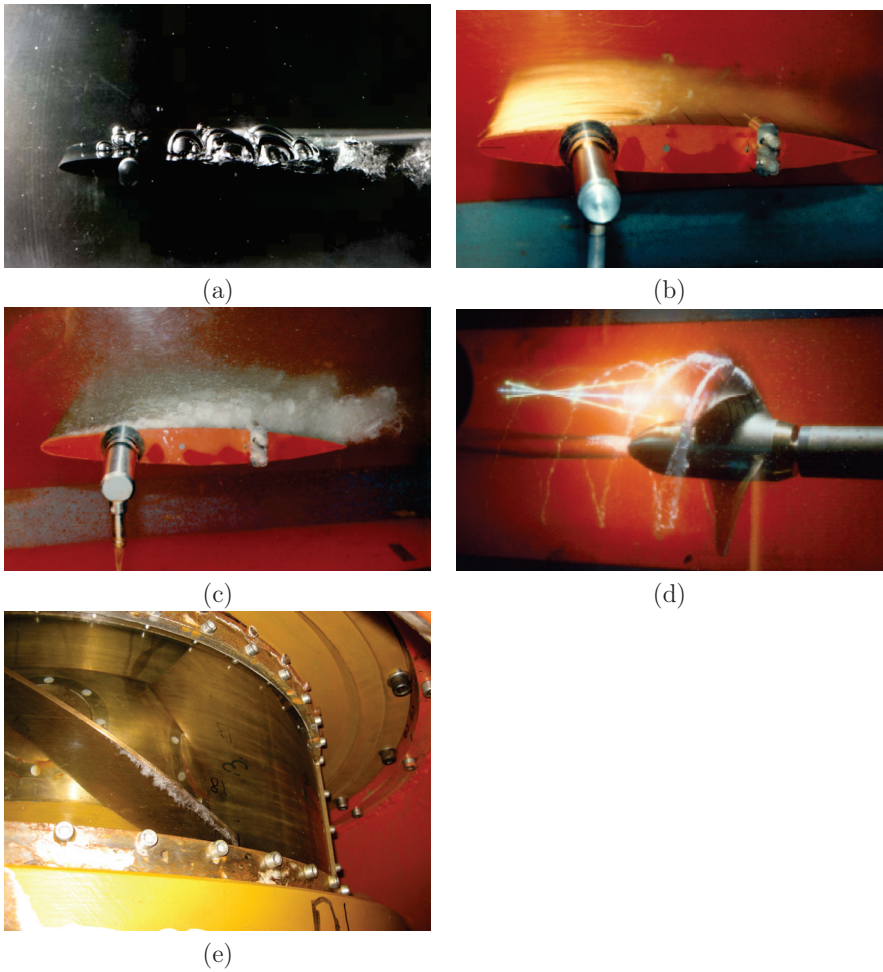
Figure 2.4: Different types of cavitation: (a) bubble cavitation; (b) sheet cavitation; (c) cloud cavitation; (d) tip and hub cavitation; (e) tip clearance cavitation. (Photo (a), courtesy of Applied Fluid Engineering Laboratory at The University of Tokyo, www.fluidlab.sys.t.u-tokyo.ac.jp. Photos (b), (c) and (d) are from experiments performed at MIT's Variable Pressure Water Tunnel, courtesy of Dr. S. Kinnas. The personal photo (e) is from a cavitation test conducted on the model of a Kaplan turbine at Vattenfall Research and Development, Älvkarleby.)

- The upstream part, still attached to the blade, grows into a new sheet cavity.

- The downstream part turns into a cloud of small bubbles advected by the flow. The small bubbles **collapse** when they reach a region with higher pressure.

Bubble collapse and erosion

Depending on their properties and the pressure applied on them, the small bubbles may stay in equilibrium, collapse, or grow into macroscopic bubbles. Studies in the context of cavitation erosion focus on the bubble collapses and their damaging effects. Rayleigh [59] originally explained that a single collapsing spherical bubble emits a large pressure peak which can be directly responsible for surface damages. The shock wave radiated in the liquid may however also influence the collapse of the surrounding bubbles and cause a focus of energy [22]. Thus, erosion is in reality a result of a complex interaction within a cloud of bubbles. The shock waves emitted by collapsing bubbles affect bubbles close to walls, causing them to collapse and damage the surface [44]. Near a solid surface, a bubble is deformed and the acoustic wave emitted by the collapse of an asymmetrical bubble is weaker than the one issued from an unbounded collapse [73]. The erosion process is therefore explained by the co-existence of a shock wave and a strong liquid jet which penetrates through the bubble and impacts the surface upon collapse [5, 9, 58]. The damaging effect of the liquid jet is related to the tremendous velocity and temperature involved. The relative contribution from the shock wave and the liquid jet, on surface damage, depends on the shape of the bubble and its distance from the surface [55, 67]. Furthermore, the presence of a vapour jet induced by gravity may be observed, and yields asymmetric rebounds [70]. These observations and theories still don't fully explain the mechanism of erosion because of the diversity of factors that influence the way bubbles approach the solid surface and the way they collapse [4].

Chapter 3

Modelling of multiphase flow

Cavitation is a multiphase phenomenon. A brief survey of the available approaches to model multiphase flow is given here, followed by specific descriptions of those used in the present work, in section 3.1 and 3.2.

A multiphase flow involves at least two phases with different properties and their interaction. For sake of simplicity, only two phases are considered here. There are three different modelling approaches, depending on the properties of the flow.

1. The phases are **interpenetrating**, i.e. both phases occupy the same macroscopic space. This is modelled using two sets of mass and momentum equations, one for each phase, and they are coupled by the void fraction and by additional source terms in the momentum equations. This method is the Euler-Euler approach.

2. There is **a continuous phase and a dilute/disperse phase** where the dispersed phase occupies a *low volume fraction*. This is modelled by treating the continuous phase (typically a fluid) as a continuum while the dispersed phase is considered as particles/bubbles that are tracked individually. This method is the Euler-Lagrange approach. The mass and momentum equations are solved for the continuous phase while the dispersed phase is solved by tracking the particles/bubbles through the calculated flow field. The approach is called Lagrangian Particle Tracking (LPT) in the case of solid particles, and Discrete Bubble Model (DBM) in the case of bubbles. The dispersed phase exchanges momentum, mass and energy with the fluid phase. The trajectory of the particles/bubbles are calculated individually at specified intervals during the fluid phase calculations. The mathematical approach is presented in detail in section 3.2 and illustrated in Figure 3.1(b).

3. The phases are not interpenetrating, i.e. there is only one phase in each macroscopic position, and there is an **interface** between the phases. This is modelled by a single set of momentum and continuity equations that are shared by the two phases. The equation properties in each position is determined by which phase is present in that position. There is a sharp spatial switch (interface) between the phases that must be tracked. In numerical algorithms for interface tracking, the interfaces are updated using fixed or moving grid.

   (a) When using a **fixed (Eulerian) grid**, an implicit description of the interface must be used. The interface arbitrarily cuts and moves through the computational

9

cells. The interface is tracked by surface methods (distance function (Level-set method)) or volume methods (cell marker (MAC method) or volume fraction (VOF method)).

   i. In the **Level-set methods** the interface is represented by a distance function and a scalar convection equation is solved for this function. The function is commonly defined as the signed distance of the cell center to the interface, being positive in one phase and negative in the other phase. Based on the representation of the level-set function, no reconstruction of the interface is necessary and the curvature and normal vectors can be computed with high accuracy. However, limitations arise when merging or breakup of interface occurs, and mass conservation is not necessarily fulfilled.

   ii. In the **method of marked particles, MAC**, a cell without marker particles is considered empty, a cell with marker particles and adjacent to an empty cell is considered as a part of the interface, and other cells are considered filled with fluid. This method gives a smeared interface but can treat complex phenomena. The computing effort is significantly increased because the equations of motion for a large number of particles need to be solved.

   iii. In the **VOF method**, a scalar volume fraction is used to distinguish between the two fluids. A general mass conservative transport equation is solved for the volume fraction. The VOF method can handle severe topological changes of the interface since it requires no a priori assumptions on the nature of the interface. Its disadvantage is the difficulty of preserving a sharp interface, and that the curvature and orientation of the interface are not determined accurately. The mathematical approach of the VOF method is presented in section 3.1 and illustrated in Figure 3.1(a).

(b) A **moving grid** treats the interface explicitly. With an adaptive grid method, the grid moves with the interface so that pre-defined cell faces follow the interface. It gives a sharp interface but only small interface deformations can be considered, and modelling breakup and merging is very difficult.
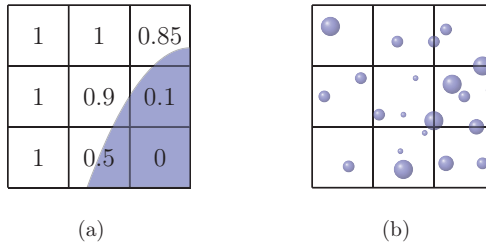

(a)   (b)

Figure 3.1: Different approaches to treat two-phase flow. (a) The Volume-Of-Fluid (VOF) method is designed to track the interface between two fluids. (b) The Discrete Bubble Model (DBM) consists of tracking bubbles smaller than the cell size.

3.1 The Volume-Of-Fluid (VOF) method

The Volume-Of-Fluid (VOF) method, introduced by Hirt and Nichols [28], is a numerical technique for tracking the sharp interface between two or more fluid phases. This method is suitable for modelling structures larger than the grid size. For sake of simplicity, only two phases are considered here. In VOF, the liquid volume fraction α takes values between 0 to 1 within a computational cell. The interface is defined to exist in the cells with intermediate values. The mixture density ρ and viscosity μ are calculated using the liquid volume fraction α, as

$$\rho = \alpha \rho_l + (1 - \alpha)\rho_v, \tag{3.1.1}$$
$$\mu = \alpha \mu_l + (1 - \alpha)\mu_v,$$

where subscripts l and v stand for liquid and vapour.

The transport equation for the volume fraction α reads

$$\frac{\partial \alpha}{\partial t} + \nabla \cdot (\alpha \mathbf{U}) = 0, \tag{3.1.2}$$

where $\mathbf{U}$ is the velocity of the mixture. Extreme care should be taken in advecting the volume fraction so as to preserve the interface sharpness. The treatment of the advection term is discussed in section 3.1.1.

Within the context of the VOF method, the mass and momentum equations read

$$\frac{\partial \rho}{\partial t} + \nabla \cdot (\rho \mathbf{U}) = 0, \tag{3.1.3}$$

$$\frac{\partial \rho \mathbf{U}}{\partial t} + \nabla \cdot (\rho \mathbf{U} \otimes \mathbf{U}) = -\nabla p + \nabla \cdot [\mu(\nabla \mathbf{U} + \nabla \mathbf{U}^T)] + \rho \mathbf{g} - \mathbf{S_{st}}, \tag{3.1.4}$$

where p is the pressure of the mixture. The additional source term $\mathbf{S_{st}}$ in the momentum equation models the effect of surface tension. This term is described in section 3.1.2.

3.1.1 Treatment of the advection term

Over the years a number of advection schemes have been developed for solving equation (3.1.2). The two possible approaches are Interface Tracking methods and Interface Capturing methods.

Interface Tracking methods

The interface is explicitly reconstructed and used in the evaluation of the advection scheme. In other words, the advected fluxes depend explicitly on the position of the interface within the cell. With this method, the performance of the advection scheme depends mainly on the accuracy of the reconstructed interface. The representation of the interface can be done by different methods, as shown in Figure 3.2. In the SLIC algorithm of Noh [52], the interface is represented by a piecewise constant line either vertically or horizontally (see Figure 3.2(b)). Youngs [74] introduced an improved model with a piecewise linear method PLIC, using information from the neighbour cells to determine the orientation of the line (see Figure 3.2(c)).
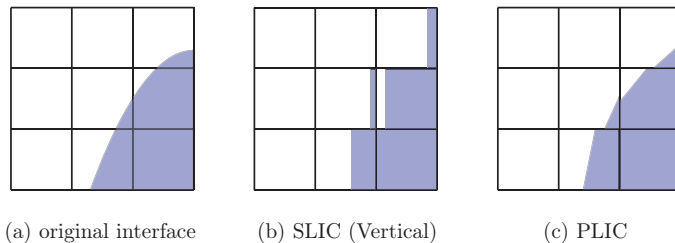
(a) original interface   (b) SLIC (Vertical)   (c) PLIC

Figure 3.2: Interface reconstruction for Interface Tracking methods.

The main drawback of these methods is the complexity of reconstructing the interface in a continuous manner across the whole domain and the extension to three dimensional problems.

Interface Capturing methods

The volume fraction at a face is formulated algebraically without reconstructing the interface and a suitable scheme is used to avoid smearing of the interface and loss of curvature. The choice of the suitable scheme has to account for the following characteristics.

- An upwind scheme is stable and diffusive. It will smear the interface.

- A downwind scheme is unstable and sharpen the interface. However the interface may be over-compressed with a downwind scheme, leading to stepping and distortion of the interface whenever the flow is not aligned with the computational grid [12].

A blending strategy is used in order to address the shortcoming of each scheme: it switches between a compressive and a non-compressive scheme depending on some criterion. This criterion can be based on the angle θ formed between the interface normal direction and the grid orientation (Figure 3.3). For an interface aligned with the cell face ($\theta = 0$) the compressive scheme is used (Figure 3.4(a)). For an interface perpendicular to the cell face, the diffusive scheme is used (Figure 3.4(b)). Hence the value at the interface is obtained from the relation

$$\tilde{\alpha_f} = \tilde{\alpha_f}^{compressive} f(\theta) + \tilde{\alpha_f}^{diffusive}(1 - f(\theta)),$$

where $f(\theta)$ varies between 0 and 1, and $\tilde{\alpha_f}$ is the normalised value of α_f,

$$\tilde{\alpha_f} = \frac{\alpha_f - \alpha_U}{\alpha_D - \alpha_U},$$

where U and D refer to the upwind and downwind cell center neighbour of the cell with center C. In order to avoid unphysical oscillations in the solution, α_f and α_C should be locally bounded between α_U and α_D. For the normalized variable, this corresponds to the coloured zone in the NVD diagram of Figure 3.5(a). It is seen in this figure that the only scheme that satisfies the boundedness criterion is the upwind scheme.

Hirt and Nichols [28] introduced a blending of first order upwind and downwind fluxes with their donor-acceptor scheme. This approach has also been followed in the derivation

of the High Resolution Interface Capturing (HRIC) scheme [51]. Figure 3.5(b) displays the normalized function of the bounded downwind scheme of the HRIC model, the Gamma [33] and the Inter-Gamma [32] differencing scheme. The InterGamma scheme is similar to the HRIC scheme but it introduces a smooth change from upwind to downwind differencing. In the Gamma differencing scheme, the smooth change is done with central differencing.

In Rusche's model [61], the compression of the surface is achieved by introducing an extra artificial compression term active only in the interface region $\nabla \cdot (\alpha(1-\alpha)\mathbf{U}_r)$, where $\mathbf{U}_r$ is the relative velocity between the two fluids.

The main concern with these schemes is the deterioration in performance observed for high Courant numbers. Indeed in that case, they become more and more diffusive because the normalized variable function reverts to the upwind scheme.
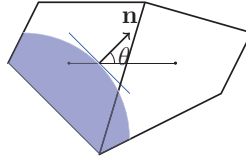

Figure 3.3: Angle between interface and cell face.
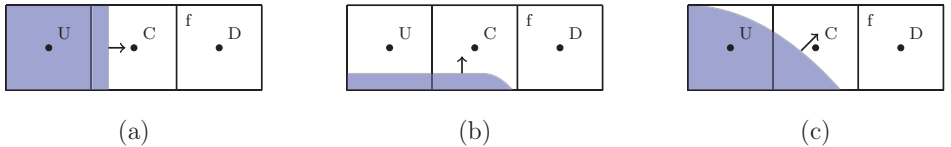

| (a) | (b) | (c) |

Figure 3.4: Blending strategy for Interface Capturing schemes. (a) Only the fluid at the downstream cell should be convected through the cell face f. A compressive scheme should be used. (b) The convected fluid is expected to be of the same composition as the upwind cell. An upwind scheme should be used. (c) Blending of the compressive and diffusive scheme.

3.1.2 Treatment of the surface tension

In the CSF (continuum surface force) method of Brackbill [7], the surface tension forces are reformulated into an equivalent volume force. In this way, the discontinuous interfacial jump condition is modelled as smooth: instead of considering the interface as a sharp discontinuity, it is considered to have a finite thickness which is a smooth transition from one fluid to the other. The dispersion of the surface tension across the transition region is obtained with the gradient of the volume fraction $\nabla\alpha$. The source term in the momentum equation reads

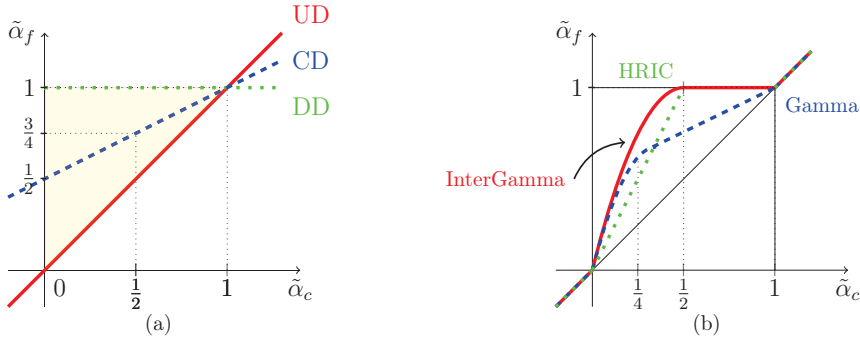$$\mathbf{S_{st}} = \sigma_{st}\kappa\delta\mathbf{n},$$

Figure 3.5: (a) The boundedness criterion is represented in the NVD diagram. It corresponds to the following conditions. For $0 \leq \tilde{\alpha}_c \leq 1$, $\tilde{\alpha}_c$ is bounded below by $\tilde{\alpha}_f = \tilde{\alpha}_c$, and above by $\tilde{\alpha}_f = 1$ (colored region). For $\tilde{\alpha}_c < 0$ or $\tilde{\alpha}_c > 1$, $\tilde{\alpha}_f = \tilde{\alpha}_c$. The upwind UD, downwind DD and central CD are shown in the diagram. (b) The HRIC, InterGamma and Gamma differencing schemes are shown in the NVD diagram. The smooth change in the Gamma and InterGamma schemes is obtained with $\tilde{\alpha}_f = -2\tilde{\alpha}_c^2 + 3\tilde{\alpha}_c$.

where σ_{st} is the surface tension coefficient, δ is the function that ensures that the force is only applied at the interface ($\delta = |\nabla\alpha|$), $\mathbf{n}$ is the normal vector of the interface ($\mathbf{n} = \frac{\nabla\alpha}{|\nabla\alpha|}$) and κ is the curvature at the interface ($\kappa = -\nabla \cdot \mathbf{n}$).

The original form of the CSF method may lead to formation of vortex-like flow in the neighbourhood of the interface. These perturbations called spurious currents may cause instabilities and destroy the interface if the surface tension is dominant. In an effort to reduce these effects, different approaches have been introduced such as improving the curvature calculation with an estimator function [45], or height function [54]. Brackbill [7] suggested to simply add a density scaling factor $\frac{2\rho}{\rho_l + \rho_v}$ to the force.

3.2 The Discrete Bubble Model (DBM)

The discrete bubble modelling consist of tracking individual bubbles in a fluid flow. This method is relevant for bubbles smaller than the grid size. The DBM approach includes the description of the motion of the bubbles, their influence on the flow, their interaction with the solid surface and with other bubbles. These models are exposed here.

3.2.1 Bubble equations of motion

A bubble B is considered as a point source when modelling its transport in the surrounding fluid, while the bubble finite volume is accounted for when modelling its interaction with other bubbles or with the solid surface. A bubble B is defined by the position of its center, $\mathbf{x_B}$, its diameter, $D = 2R$, its velocity, $\mathbf{U_B}$ and its density, ρ_B. Its volume is $V_B = \frac{4}{3}\pi\left(\frac{D}{2}\right)^3$ and its mass is $m_B = \rho_B V_B$. The surrounding liquid has a density ρ_l, a velocity $\mathbf{U}_l$ and a pressure p_l. In a Lagrangian frame, each bubble position vector $\mathbf{x}_B$ is calculated from the

equation

$$\frac{d\mathbf{x}_B}{dt} = \mathbf{U}_B,$$ (3.2.5)

and the motion of each bubble is governed by Newton's second law

$$m_B\frac{d\mathbf{U}_B}{dt} = \mathbf{F_a} + \mathbf{F}_p + \mathbf{F}_{buoy} + \mathbf{F_{drag}} + \mathbf{F}_{vol} + \mathbf{F}_{lift}.$$ (3.2.6)

The forces acting on the bubble are the added mass force, the pressure gradient force, the buoyancy force, the drag force, the force due to volume variation of the bubble and the lift force.

$$\mathbf{F}_a = \frac{1}{2}\rho_l\frac{m_B}{\rho_B}\left(\frac{D\mathbf{U}_l}{Dt} - \frac{d\mathbf{U}_B}{dt}\right),$$

$$\mathbf{F}_p = -\frac{m_B}{\rho_B}\nabla p_l,$$

$$\mathbf{F}_{buoy} = m_B(1 - \frac{\rho_l}{\rho_B})\mathbf{g},$$

$$\mathbf{F}_{drag} = C_{drag}\rho_l\frac{m_B}{\rho_B}\frac{3}{8R}(\mathbf{U}_l - \mathbf{U}_B)|\mathbf{U}_l - \mathbf{U}_B|,$$

$$\mathbf{F}_{vol} = \frac{1}{2}\rho_l\frac{dV_B}{dt}(\mathbf{U}_l - \mathbf{U}_B) = \rho_l\frac{m_B}{\rho_B}\frac{3\dot{R}}{2R}(\mathbf{U}_l - \mathbf{U}_B),$$

$$\mathbf{F}_{lift} = C_{lift}\rho_l\frac{m_B}{\rho_B}(\mathbf{U}_l - \mathbf{U}_B) \times \omega_l.$$

Empirical relations of drag, lift and added mass effect for spherical non-rotating particles are considered in this model and

- $\frac{D\mathbf{U}_l}{Dt}$ is the total acceleration of the fluid as seen by the bubble ($\frac{D\mathbf{U}_l}{Dt} = \frac{d\mathbf{U}_l}{dt} + \mathbf{U}_l\cdot\nabla\mathbf{U}_l$) evaluated at the bubble position,

- $\mathbf{g}$ is the gravitational acceleration,

- C_{lift} is the lift coefficient, assumed to take the value 0.5 according to Auton [3],

- ω_l is the vorticity of the fluid, $\omega_l = \nabla \times \mathbf{U}_l = (\frac{\partial w}{\partial y} - \frac{\partial v}{\partial z})\mathbf{n}_x + (\frac{\partial u}{\partial z} - \frac{\partial w}{\partial x})\mathbf{n}_y + (\frac{\partial v}{\partial x} - \frac{\partial u}{\partial y})\mathbf{n}_z$,

- C_{drag} is the drag coefficient, and it depends on the bubble Reynolds number

$$\text{Re}_B = \frac{2\rho_l R|\mathbf{U}_l - \mathbf{U}_B|}{\mu_l}.$$

The experimental study of Haberman and Morton [25] indicates that the drag coefficient of a bubble is equal to the drag of a rigid sphere for $Re_B{<}40$. The discrepancy at higher Reynolds number is due to the internal circulatory motion and the deformation of the bubble. This range is out of the scope of this study because strictly spherical bubbles are considered. For very small Reynolds number (≤ 0.1), the Stokes law is valid and the drag coefficient is $C_{drag} = \frac{24}{Re_B}$. For larger Reynolds number, an empirical law [64] is used:

$$C_{drag} = \frac{24}{Re_B}\left(1 + 0.15Re_B^{0.687}\right) \quad \text{for } 0.1 < Re \leq 1000,$$
$$= 0.44 \quad \text{for } Re > 1000.$$

Equation (3.2.6) was introduced in the context of solid particles by Stokes [69] and modified by Boussinesq [6] and Maxey and Riley [43] among others. Besides rotation, the present model also neglects the Basset history force, as well as the Faxen correction on the drag force that accounts for non uniform flow effects. In order to account for the specificity of a bubble compare to a solid particle, Johnson and Hsieh [34] introduced a force due to the variation of the volume. They assumed that this force was negligible except at the time of collapse. Hence this force was not included in their numerical computations of bubble trajectories. This force was accounted for by Giannadakis et al. [19], Hsiao et al. [29] and Shams and Apte [66], among others, without further comments. However, the analysis performed in Paper II shows that this force has an erroneously large contribution at collapse. It is therefore advised to neglect the force F_{vol} when bubble dynamics is included.

The fluid velocity $\mathbf{U}_l$, acceleration $\frac{D\mathbf{U}_l}{Dt}$, pressure p_l and vorticity ω_l, calculated in the Eulerian reference frame, are needed for the calculation of the forces in the Lagrangian frame. Therefore they have to be interpolated to the position of the bubble from the neighbouring cells. These terms evaluated at the bubble position are denoted with the subscript @B.

After rearranging terms, equation (3.2.6) becomes

$$
\begin{aligned}
\frac{d\mathbf{U}_B}{dt} =& \frac{1}{\frac{\rho_B}{\rho_l} + \frac{1}{2}} \Big[\frac{1}{2} \frac{D\mathbf{U}_{l@B}}{Dt} - \frac{1}{\rho_l} \nabla p_{l@B} + (\frac{\rho_B}{\rho_l} - 1)\mathbf{g} \\
&+ \big(\frac{3C_{drag}|\mathbf{U}_{l@B} - \mathbf{U}_B|}{8R} + \frac{3\dot{R}}{2R}\big)(\mathbf{U}_{l@B} - \mathbf{U}_B) + C_{lift}(\mathbf{U}_{l@B} - \mathbf{U}_B) \times \omega_{l@B} \Big].
\end{aligned}
\tag{3.2.7}
$$

Finally the discrete bubble model consists in solving the system of 6 first-order ODEs given by equations (3.2.5) and (3.2.7) with a time integration method, such as a Runge-Kutta method. During the Eulerian time step dt, each bubble is tracked by solving these equations at least once and at most as many times as the times the bubble trajectory crosses a cell. A Lagrangian time step is defined as the time it takes for the particle to leave the cell it occupied. Therefore, there is a specific distribution of the Lagrangian time steps $\Delta t_{k,i}$, $k = 1..K_i$ within an Eulerian time step dt for each bubble B_i such that $dt = \sum_{k=1}^{K_i} \Delta t_{k,i}$ for any B_i .

3.2.2   Influence from the bubbles on the flow

The fluid phase is governed by the incompressible Navier-Stokes equations

$$
\nabla \cdot \mathbf{U}_l = 0,
\tag{3.2.8}
$$

$$
\rho_l \frac{\partial \mathbf{U}_l}{\partial t} + \rho_l (\mathbf{U}_l \cdot \nabla)\mathbf{U}_l = -\nabla p_l + \mu_l \nabla^2 \mathbf{U}_l + \rho_l \mathbf{g} - \mathbf{S_B}.
\tag{3.2.9}
$$

The additional source term $\mathbf{S}_B$ in the momentum equation (3.2.9) is due to the influence of the bubbles on the flow. According to the Lagrangian theory, a momentum source contribution is generated by a Lagrangian bubble in each cell visited along its path. Each bubble B_i which is in a cell $cell_k^0$ of volume V_k^0 generates a contribution during a time specific to this bubble, $\Delta t_{k,i}$. Thus, the contribution of all bubbles B_i, $i = 1 : I$, crossing the cell $cell_k^0$ is commonly written as

$$
\mathbf{S}_B[cell_k^0] = \frac{-1}{V_k^0} \sum_{i=1}^{I} m_{B_i} \frac{\Delta \mathbf{U}_{B_i}}{\Delta t_{k,i}}.
\tag{3.2.10}
$$

If the volume of the bubble is smaller than the cell $cell_k^0$ that hosts the bubble centroid, then equation (3.2.10) is accurate. However, if the volume of the bubble is larger than $cell_k^0$, then the point-particle theory is violated. This shortcoming is a common issue when modelling Lagrangian bubbles in a turbulent flow because both approaches imply conflicting assumption on the grid size. The point-particle theory requires that the cells are much larger than the bubbles while the turbulent modelling requires very small cells. In order to account for the fact that the bubble is not a point-particle but has a finite volume, the contribution S_B is also distributed in the neighbouring cells of $cell_k^0$, $\{cell_k^j, j = 1 : J\}$, yielding

$$\mathbf{S}_B[cell_k^j] = \frac{-1}{V_k^j} \sum_{i=1}^{I} m_{B_i} \frac{\Delta \mathbf{U}_{B_i}}{\Delta t_{k,i}} H(\mathbf{x}_B - \mathbf{x}_k^j) \text{ for } j = 0 : J \qquad (3.2.11)$$

where $\mathbf{x}_k^j$ is the center of cell $cell_k^j$ and the function H is a Gaussian function centred in $\mathbf{x}_B$ with variance R,

$$H(\mathbf{x}_B - \mathbf{x}_k^j) = \frac{1}{(R\sqrt{2\pi})^3} exp\left(-\frac{1}{2}\left[\frac{|\mathbf{x}_k^j - \mathbf{x}_B|}{R}\right]^2\right). \qquad (3.2.12)$$

This method is illustrated in Figure 3.6. If the contribution is applied to the cells that fulfil $|\mathbf{x}_B - \mathbf{x}_k^j| < 3R$, then 99.9% of the source term is distributed with this approach.
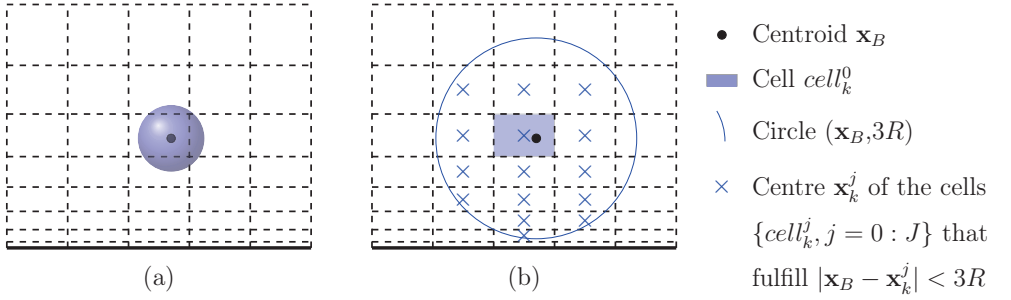

Figure 3.6: (a) A Lagrangian bubble larger than the host cell. (b) The circle with center $\mathbf{x}_B$ and radius $3R$ shows the zone of influence of the function $H(\mathbf{x}_B - \mathbf{x}_k^j)$ for $|\mathbf{x}_B - \mathbf{x}_k^j| < 3R$, in 2D.

Depending on the particle concentration, Elghobashi [14] defined different flow regimes in particle-laden flow. It is assumed that these results can be extended to the case of bubbles. In the case of a dilute suspension (which means that $|\mathbf{x}_{B_i} - \mathbf{x}_{B_j}| > 10D$) with a volume fraction of bubbles lower than 10^{-6}, their effects on the flow and turbulence are negligible. This is usually denoted one-way coupling, i.e. the flow affects the bubbles but the bubbles don't affect the flow. In that case, the additional source term $\mathbf{S}_B$ in the momentum equation is neglected. As a consequence of the very low volume fraction of bubbles, inter-bubble collisions are also neglected. For a higher volume fraction (in the range $[10^{-6}, 10^{-3}]$), the bubbles enhance production or dissipation of turbulence. In that case the source term is included in equation (3.2.9) and this is a two-way coupling approach. For a dense suspension

$(|\mathbf{x}_{B_i} - \mathbf{x}_{B_j}| < 10D)$ the bubble-bubble interactions must also be taken into account with a model for collision. Models for collision detection and outcome are presented in section 3.2.4

3.2.3 Bubble-wall collisions

A bubble colliding with a wall either bounces, sticks or slides depending whether inertia or dissipation dominates the process. Experiments show the presence of a liquid film between the bubble and the wall at collision [57]. Zenit [77] showed that the behaviour of a bubble colliding with a wall is different from that of a solid sphere, due to the liquid film and the bubble deformation. It was found that the coefficient of restitution ϵ_w depends on the capillary number $Ca = \frac{\mu_l U^{0n}}{\sigma_{st}}$ and the modified Stokes number $St^* = \frac{(\rho_B + \frac{1}{2}\rho_l)DU^{0n}}{9\mu_l}$, it reads

$$\epsilon_w = e^{-30\sqrt{Ca/St^*}}.$$

In practice, an impact with a wall is modelled when the bubble trajectory crosses a face f_w of the wall boundary. Neglecting the actual flattening of the bubble when it approaches a surface boundary, it is assumed that a collision occurs when the distance from the spherical bubble center to the center of the face is equal to the bubble radius. Denoting the normal and tangential unit vectors of f_w as $\mathbf{n}_w$ and $\mathbf{t}_w$, respectively, the bubble velocity before the impact is written as

$$\mathbf{U}_B^0 = U_B^{0n}\mathbf{n}_w + U_B^{0t}\mathbf{t}_w.$$

The normal component of the bubble velocity after the impact is evaluated as $U_B^n = -\epsilon_w U_B^{0n}$ and the tangential component is unchanged as friction is neglected.

3.2.4 Bubble interactions

A deterministic model for collision detection and its outcome are described here.

Collision detection

Consider a bubble pair with respective radius R_1 and R_2, respective initial velocities $\mathbf{U}_{B1}^0$ and $\mathbf{U}_{B2}^0$, and at a distance $|\mathbf{x}_{B1}^0 - \mathbf{x}_{B2}^0| = d_{12}^0 > (R_1 + R_2)$ from each other. Figure 3.7 shows that the angle θ is the angle between the line (1,2) joining the bubble centres and the relative velocity $\mathbf{U}_{B12}^0 = \mathbf{U}_{B1}^0 - \mathbf{U}_{B2}^0$. The distance d is the projection on line (1,2) of the distance travelled during the time step dt,

$$d = |\mathbf{U}_{B12}^0| \cos\theta dt.$$

A collision occurs within the time dt if $\theta < \theta_c$ and $d \geq d_c$, where the critical angle and distance are given by

$$\theta_c = \arctan\left(\frac{R_1 + R_2}{\sqrt{(d_{12}^0)^2 - (R_1 + R_2)^2}}\right),$$

$$d_c = \frac{d_{12}^0 - \sqrt{(d_{12}^0)^2 - (1 + \tan\theta^2)\left((d_{12}^0)^2 - (R_1 + R_2)^2\right)}}{(1 + \tan\theta^2)}.$$
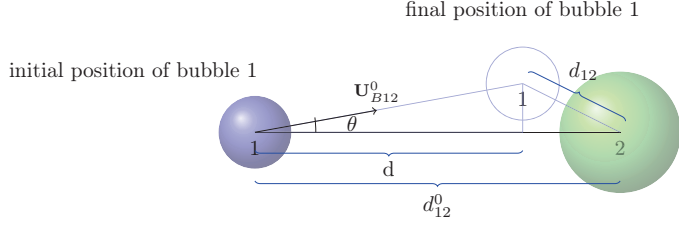
Figure 3.7: The distance d is the projection on the line (1,2) of the distance travelled by the bubble 1 with respect to the bubble 2.

Collision outcome

The outcome of a collision between a bubble pair is either bouncing or coalescence depending on two parameters, the size of the bubbles and the collision speed. Experimental results [13] suggest that coalescence is enhanced when both parameters have a small value. This corresponds to a small Weber number. The Weber number based on the equivalent diameter, $D_{eq} = \frac{4R_1 R_2}{R_1 + R_2}$, is given by

$$We_{eq} = \frac{\rho_l |\mathbf{U}_{B2}^n - \mathbf{U}_{B1}^n|^2 D_{eq}}{2\sigma_{st}}, \qquad (3.2.13)$$

where the collision speed is $|\mathbf{U}_{B2}^n - \mathbf{U}_{B1}^n|$, and $\mathbf{U}_{Bi}^{0n}$ is the normal component of the velocities before impact, as shown in Figure 3.8.
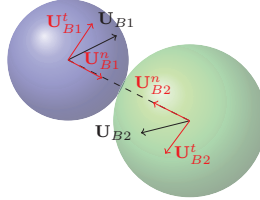

Figure 3.8: Decomposition of the velocities into normal and tangential components.

The theoretical models that have been developed to predict the coalescence efficiency (i.e. the probability that a collision results in coalescence) are based on the observation that a liquid film is trapped between the bubbles at impact [10, 68]. The bubbles coalesce if the liquid film has time to drain during the time the bubble pair interacts. The outcome of collision is therefore assumed to be a function of two time-scales, the interaction time t_i and the drainage time t_d. The resulting coalescence probability for a head-on collision is theoretically $P_c = 0$ if $t_i < t_d$ and $P_c = 1$ if $t_i \geq t_d$. In order to account for the the fact that the collision may not be frontal, a smooth semi-empirical function is used [10], and the coalescence probability is expressed as $P_c = e^{-t_d/t_i}$. If a uniform random number in the range [0,1] becomes smaller than the coalescence probability then coalescence occurs, otherwise

bouncing happens. According to Chester [11], the time-scales are given by $t_i = \left(\frac{\rho_l D_{eq}^3}{16\sigma_{st}}\right)^{\frac{1}{2}}$ and $t_d = \frac{\rho_l |\mathbf{U}_{B2}^n - \mathbf{U}_{B1}^n| D_{eq}^2}{8\sigma_{st}}$. Thus, the probability is given by

$$P_c = e^{-\sqrt{\frac{We_{eq}}{2}}}. \tag{3.2.14}$$

Bouncing

In the case of bouncing, the momentum and trajectory of both bubbles are altered. It is assumed that bubble deformation and friction are neglected in the present work. Using the notations of Figure 3.8, the unit normal vector is given by

$$\mathbf{n}_{12} = \frac{\mathbf{x}_{B2}^0 - \mathbf{x}_{B1}^0}{|\mathbf{x}_{B2}^0 - \mathbf{x}_{B1}^0|},$$

and the velocity normal components are expressed as

$$\mathbf{U}_{Bi}^{0n} = (\mathbf{U}_{Bi}^0 \& \mathbf{n}_{12}) \cdot \mathbf{n}_{12}.$$

The normal component of the velocities after impact changes according to

$$\mathbf{U}_{Bi}^n = \frac{m_{Bi}\mathbf{U}_{Bi}^{0n} + m_{Bj}\mathbf{U}_{Bj}^{0n} - m_{Bj}\epsilon(\mathbf{U}_{Bi}^{0n} - \mathbf{U}_{Bj}^{0n})}{m_{Bi} + m_{Bj}}, \tag{3.2.15}$$

where ϵ is the coefficient of restitution, and the tangential component is unchanged after collision because friction is neglected.

Coalescence

In the case of coalescence of two bubbles, 1 and 2, a new bubble is formed with properties R, $\mathbf{x}_B$ and $\mathbf{U}_B$. Conservation of mass, momentum and energy yields

$$R = \left(R_1^3 + R_2^3\right)^{\frac{1}{3}},$$

$$\mathbf{x}_B = \frac{m_{B1}\mathbf{x}_{B1} + m_{B2}\mathbf{x}_{B2}}{m_{B1} + m_{B2}},$$

$$\mathbf{U}_B = \frac{m_{B1}\mathbf{U}_{B1} + m_{B2}\mathbf{U}_{B2}}{m_{B1} + m_{B2}}.$$

Chapter 4

Cavitation modelling

4.1 Cavitation models

There are various computational approaches to predict cavitation with different levels of complexity. A short review of the methods used for cavitation prediction and simulation is given here.

Empirical methods: These methods consist of empirical correlations. It is used to determine the allowable suction head for a turbine and the critical cavitation coefficient. This simple method is still indispensable for design.

Boundary methods: These methods are applicable to steady sheet cavitation. The shape of an attached cavity is determined iteratively from an initial guess until the pressure in the cavity is equal to the vapour pressure. The initial form is determined by vapour pressure isosurface or by the envelope of a travelling bubble. The computational time is short but it can not predict accurately the pressure distribution. Improvement and modifications have been implemented to increase the accuracy of the method [27].

Bubble model: This model is used for bubble cavitation [37]. It is based on the Rayleigh-Plesset equation, which describes the dynamics of the bubble. This model is presented in section 4.3.

Multiphase methods: These models are based on the classical modelling of multiphase flow as presented in section 3. They use continuity and momentum equations and are suitable for turbulent flow. Therefore they are intensively used for the modelling of sheet, cloud and vortex cavitation.

> **Euler-Euler model:** The mathematical model is based on the two-fluid model where a separate set of mass and momentum conservation equations are solved for each phase. The interfacial mass and momentum transfer require modelling. The mass transfer is given by a simplified Rayleigh equation. This method can account for compressibility of both phases. It is used by Kunz et al. [40] and Saurel and Lemetayer [63].

> **Mixture model:** This model is based on the concept of phase averaging and consider an homogeneous mixture of vapour and liquid. This approach handles the two-phase mixture as a single fluid with variable fluid properties and solve the mass

and momentum conservation equations for the mixture. The pressure and density are connected explicitly or implicitly:

1. An explicit way to relate pressure and density is an **equation of states** $\rho = f(p)$, as done by Wallis [75] for instance. Reboud and Delannoy [60] use a barotropic equation of state $\frac{\partial \rho}{\partial p} = \frac{1}{a^2}$, where a is the speed of sound in the mixture. Such models are mainly used for cavitation in nozzles and give poor results for cavitation on hydrofoils. This method models the cavity attached to the hydrofoil and fails to capture the dynamics of the cavity with the re-entrant jet and the cloud shedding [21].

2. A **transport equation for the volume fraction** is used with appropriate source terms to regulate the mass transfer between the vapour and liquid phases. Thus, the pressure and density are connected implicitly via the source term in the volume fraction transport equation. Among the various modelling approaches, the cavitation models based on a transport equation have received growing interests and they will be described further in the next section.

Apart from the multiphase approach chosen to model production, destruction and transport of cavitation structures, one should also pay attention to the turbulence model. Running two dimensional RANS simulations is fast but it leads to unrealistic results because the actual interactions between the non-isotropic turbulent vortex and the cavitation structures are not considered. Therefore three dimensional LES simulations are more suitable in the context of cavitation modelling.

4.2   Mass transfer models

The mass transfer models account for the mass transfer between liquid and vapour. These models are based on the transport equation of the liquid volume fraction α and use the same principles as the VOF method described in section 3.1.

The transport equation for the liquid volume fraction reads

$$\frac{\partial \alpha}{\partial t} + \nabla \cdot (\alpha \mathbf{U}) = S_\alpha, \tag{4.2.1}$$

where the source term $S_\alpha = -\frac{\dot{m}}{\rho_l}$ accounts for evaporation and condensation, and $\dot{m}$ is the mass transfer rate between the liquid and the vapour phase. Summing the transport equations for liquid volume fraction α and the vapour volume fraction $(1 - \alpha)$, yields the non divergence free continuity equation,

$$\nabla \cdot \mathbf{U} = (\frac{1}{\rho_v} - \frac{1}{\rho_l})\dot{m}. \tag{4.2.2}$$

The difficulty lies in the modelling of the mass transfer $\dot{m}$. Several models have been proposed, based on this concept of mass transfer with differences in the source terms. The evaporation and condensation terms are function of the pressure and the volume fraction in the model proposed by Merkle et al. [47] and Kunz et al. [38]. Senocak and Shyy [65] also account for the interfacial velocity. In the model of Kunz et al. [39], the non-condensable gas volume fraction α_g is also considered such that the mixture density is given

by $\rho = \alpha_v \rho_v + \alpha_l \rho_l + \alpha_g \rho_g$, and α_l is replaced by $(\alpha_l - \alpha_g)$ in the evaporation term. It is important to take into account the non-condensable gas because these bubbles persist longer in the downstream flow compare to the water vapour that condense quickly when it reaches the higher pressure region [1]. This feature has been included by Lu [41] in a new formulation of the Sauer and Schnerr model.

4.2.1 The model of Sauer and Schnerr [62]

In order to derive the mass transfer rate, $\dot{m}$, Sauer and Schnerr [62] stated that the inception of cavitation is due to the presence and growth of nuclei in the liquid. The nuclei are assumed to be spherical micro-bubbles filled solely with water vapour. These micro-bubbles are assumed to be uniformly distributed in the liquid and to have the same radius, R_{nuc}. The number of micro-bubbles per unit volume is denoted n_{nuc} and the vapour volume fraction is therefore expressed as

$$(1 - \alpha) = \frac{\frac{4}{3}\pi R_{nuc}^3 n_{nuc}}{1 + \frac{4}{3}\pi R_{nuc}^3 n_{nuc}}. \tag{4.2.3}$$

Furthermore, Sauer and Schnerr [62] assumed that the dynamics of each micro-bubble is governed by a simplified Rayleigh-Plesset equation, obtained by neglecting the second-order derivative, the viscosity and the surface tension. The pressure inside the nuclei is the saturated vapour pressure, p_v, and the liquid pressure at the micro-bubble position is set to the local mixture pressure, p. Thus the nuclei growth rate is given by

$$\dot{R}_{nuc} = sign(p_v - p)\sqrt{\frac{2}{3}\frac{|p_v - p|}{\rho_l}}.$$

In order to formulate the mass transfer rate as a function of α and $\dot{R}_{nuc}$, equation (4.2.2) is written as

$$\dot{m} = \frac{\rho_l \rho_v}{\rho_v - \rho_l}\nabla \cdot \mathbf{U}. \tag{4.2.4}$$

The mass conservation equation (3.1.3) yields

$$\nabla \cdot \mathbf{U} = -\frac{1}{\rho}\frac{d\rho}{dt}. \tag{4.2.5}$$

The mixture density ρ in equation (3.1.1) depends on α, and its time derivative is expressed as

$$\frac{d\rho}{dt} = (\rho_l - \rho_v)\frac{d\alpha}{dt}. \tag{4.2.6}$$

Using the definition of (1-α) in equation (4.2.3), it is possible to write its time derivative as a function of α and $\dot{R}_{nuc}$, as

$$-\frac{d\alpha}{dt} = \frac{4\pi R_{nuc}^2 \dot{R}_{nuc} n_{nuc}}{(1 + \frac{4}{3}\pi R_{nuc}^3 n_{nuc})^2}$$

$$= \alpha \frac{4\pi R_{nuc}^2 \dot{R}_{nuc} n_{nuc}}{1 + \frac{4}{3}\pi R_{nuc}^3 n_{nuc}}$$

$$= (1 - \alpha)\alpha \frac{3\dot{R}_{nuc}}{R_{nuc}}. \tag{4.2.7}$$

23

Combining equations (4.2.4), (4.2.5), (4.2.6) and (4.2.7) yields a mass transfer rate of

$$\dot{m} = \frac{\rho_l \rho_v}{\rho}(1 - \alpha)\alpha \frac{3\dot{R}_{nuc}}{R_{nuc}}. \tag{4.2.8}$$

These models agree well with experimental observations of cavitation on hydrofoils. With an appropriate model for the turbulence, they predict the mechanism of the inception, the development into a sheet cavity, the re-entrant jet breaking the cavity and the cloud shedding. However, they do not model the collapse of bubbles and its consequences (pressure wave, pitting on the surface, etc). The vapour cloud shrinks when it comes to the region with higher pressure, but since the cloud is treated as a volume fraction of vapour, the collapse of individual bubbles is not represented. To take account for this, the model should include the presence and the dynamic of the bubbles contained in the cloud of vapour.

4.3 The cavitation bubble model

Rayleigh and Plesset [56, 59] analysed the dynamics of a single spherical bubble in a stagnant fluid. First, this analysis is described. Next, the approach is extended for modelling bubble dynamics in the context of the cavitation bubble model.

4.3.1 Dynamics of a still bubble in an unbounded domain

The bubble is defined by a radius $R(t)$, a rate of growth $\dot{R} = \frac{dR}{dt}$, a density ρ_B and a constant internal pressure p_B. The surrounding liquid has a density ρ_l, a velocity $\mathbf{U}_l(r, t)$ and a pressure $p_l(r, t)$ at a distance r from the bubble. Far from the bubble the liquid pressure is $p_l(\infty, t)$. It is the sum of a constant reference pressure p_0 and a time varying pressure $p(t)$. The bubble is initially in equilibrium at liquid pressure p_0, in a stagnant fluid. Thus, the initial conditions are

$$p_l(r, 0) = p_l(\infty, 0) = p_0 \ \ \forall r$$
$$\mathbf{U}_l(r, 0) = \mathbf{0} \ \ \forall r$$
$$R(0) = R_0$$
$$\dot{R}(0) = 0$$

Any variation of the pressure $p(t)$ acts as a disturbance on the bubble stability. Therefore the radius of the bubble $R(t)$ evolves and it induces a velocity $\mathbf{U}_l \neq \mathbf{0}$ in the surrounding liquid, as shown in Figure 4.1. In order to express the radius R and the rate of growth $\dot{R}$ as a function of time, the analysis of the bubble dynamics is performed under the following assumptions:

- the bubble remains spherical,

- the bubble is composed of vapour only,

- the internal pressure is uniform, $p_B = p_v$,

- the liquid density is large ($\rho_l \gg \rho_B$),

- the liquid is assumed incompressible,

- the surface tension σ_{st} and the liquid viscosity ν_l are accounted for.

The assumption of strict sphericity implies that the bubble surface moves only in the radial direction. Therefore the motion induced in the liquid is strictly radial:

$$U_{l,r}(r,t) \neq 0, \ U_{l,\theta} = U_{l,\phi} = 0.$$

Furthermore, the velocity in the bubble is denoted $\mathbf{u}_B$, in order to distinguish it from the velocity of the bubble centroid, $\mathbf{U}_B$, introduced in section 3.2.
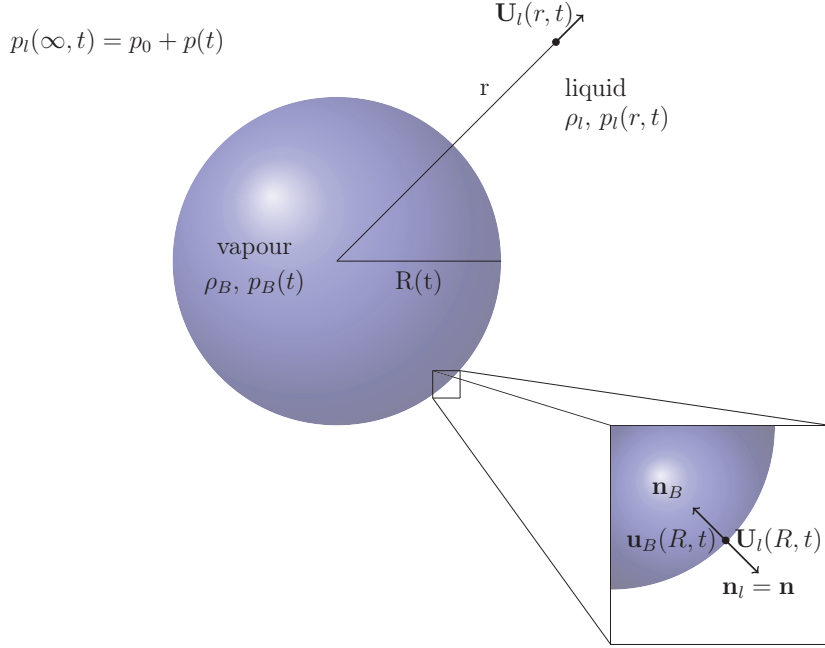

Figure 4.1: Schematic diagram of a bubble with radius R(t) in an initially stagnant liquid

The analysis of the bubble dynamics consists in first writing the mass balance across the bubble interface in order to express the liquid velocity at the interface $r = R$. Then the continuity equation yields the liquid velocity at a distance $r > R$ from the bubble. Finally, the momentum equation gives a relation between the radius R, the rate of growth $\dot{R}$, and the liquid pressure at the interface. This pressure is related to the pressure inside the bubble by writing the stress balance at the interface. This analysis yields the Raleigh-Plesset equation and is presented in detail here.

The mass balance across the bubble interface

The radial velocity of the bubble interface is $\dot{R}$, and the radial velocity at the bubble interface in the bubble and in the liquid are $u_{B,r}(R,t)$ and $U_{l,r}(R,t)$, respectively (see Figure

4.1). When the bubble size evolves, mass is transferred across the interface by evaporation or condensation. The vapour and liquid mass flow rate through the interface are denoted $\dot{m}_v$ and $\dot{m}_l$, and are expressed as

$$\dot{m}_v = \rho_B \left(u_{B,r}(R, t) - \dot{R} \right), \tag{4.3.9}$$

$$\dot{m}_l = \rho_l \left(U_{l,r}(R, t) - \dot{R} \right). \tag{4.3.10}$$

Mass conservation gives

$$\dot{m}_v = \dot{m}_l. \tag{4.3.11}$$

Combining equations (4.3.9)-(4.3.11) yields the liquid velocity at the interface,

$$U_{l,r}(R, t) = \frac{\rho_B}{\rho_l} u_{B,r}(R, t) + \left(1 - \frac{\rho_B}{\rho_l} \right) \dot{R}(t) \tag{4.3.12}$$

According to the assumption $\frac{\rho_B}{\rho_l} \ll 1$, a good approximation for the liquid radial velocity at the interface is

$$U_{l,r}(R, t) = \dot{R}(t) \tag{4.3.13}$$

The continuity equation

The spherically symmetric form of the continuity equation is

$$\frac{\partial [r^2 U_{l,r}(r, t)]}{\partial r} = 0. \tag{4.3.14}$$

Thus, by definition, the function $[r^2 U_{l,r}(r, t)]$ does not depend on r. Therefore, it is only a function of time, denoted $C(t)$. In particular, at $r = R$, it is $C(t) = R^2 U_{l,r}(R, t)$. Using equation (4.3.13) yields

$$C(t) = R^2(t)\dot{R}(t). \tag{4.3.15}$$

Therefore, the liquid velocity at a distance $r > R$ from the bubble is

$$U_{l,r}(r, t) = \frac{R(t)^2}{r^2} \dot{R}(t). \tag{4.3.16}$$

The momentum equation

The spherically symmetric form of the momentum equation is

$$\frac{\partial \mathbf{U}_l(r, t)}{\partial t} + \mathbf{U}_l(r, t) \frac{\partial \mathbf{U}_l(r, t)}{\partial r} = -\frac{1}{\rho_l} \frac{\partial p_l}{\partial r} + \nu_l \left[\frac{\partial^2 \mathbf{U}_l(r, t)}{\partial r^2} + \frac{2}{r} \frac{\partial \mathbf{U}_l(r, t)}{\partial r} - \frac{2\mathbf{U}_l(r, t)}{r^2} \right]. \tag{4.3.17}$$

Substituting the liquid velocity by $C(t)/r^2$ in the radial component of (4.3.17) gives

$$\frac{1}{r^2} \frac{\partial C(t)}{\partial t} - \frac{2C^2(t)}{r^5} = -\frac{1}{\rho_l} \frac{\partial p_l}{\partial r}. \tag{4.3.18}$$

Integrating with respect to r from R to ∞ yields

$$\frac{1}{R} \frac{\partial C(t)}{\partial t} - \frac{C^2(t)}{2R^4} = \frac{1}{\rho_l} [p_l(R, t) - p_l(\infty, t)]. \tag{4.3.19}$$

Combining equations (4.3.15) and (4.3.19) gives a relation between the radius R, the rate of growth $\dot{R}$, and the liquid pressure at the interface, as

$$R(t)\ddot{R}(t) + \frac{3}{2}\dot{R}^2(t) = \frac{1}{\rho_l}\left[p_l(R,t) - p_l(\infty,t)\right]. \tag{4.3.20}$$

Stress balance at the interface

In equation (4.3.20), the liquid pressure $p_l(R,t)$ is not known. The relationship between the pressure at the bubble surface in the liquid, $p_l(R,t)$, and inside the bubble, $p_B(t)$, is determined from the normal stress balance at the bubble interface. It reads

$$\mathbf{n}_l \cdot \tau_l + \mathbf{n}_B \cdot \tau_B = \sigma_{st}\kappa\mathbf{n}_l - \nabla_t\sigma_{st} + \dot{m}_l\mathbf{U}_l \cdot \mathbf{n}_l + \dot{m}_v\mathbf{u}_B \cdot \mathbf{n}_B, \tag{4.3.21}$$

where $\mathbf{n}_l$ and $\mathbf{n}_B$ are the unit normal vector at the interface pointing outward and inward the bubble, respectively (see Figure 4.1). τ_l and τ_B are the stress tensor in the liquid and the bubble, respectively.

$$\tau_l = -p_l(R,t)\mathbf{I} + \mu_l\left(\nabla\mathbf{U}_l + \nabla\mathbf{U}_l^T\right)\Big|_{r=R}. \tag{4.3.22}$$

$$\tau_B = -p_B(t)\mathbf{I}. \tag{4.3.23}$$

The curvature of the interface, κ, is

$$\kappa = \nabla \cdot \mathbf{n}_l = \nabla \cdot \mathbf{r}\Big|_{r=R} = \left(\frac{1}{r^2}\frac{\partial r^2}{\partial r}\right)\Big|_{r=R} = \frac{2}{R}. \tag{4.3.24}$$

The 4th term in equation (4.3.21) is the tangential stress associated with gradients in surface tension, and $\mathbf{t}$ is the unit tangent vector at the interface. The 5th and 6th terms are the temporal mass fluxes across the interface. Using the notations $\mathbf{n} = \mathbf{n}_l = -\mathbf{n}_B$ and $\dot{m} = \dot{m}_v = \dot{m}_l$, equation (4.3.21) becomes

$$\mathbf{n} \cdot \tau_l - \mathbf{n} \cdot \tau_B = \frac{2\sigma_{st}}{R}\mathbf{n} - \nabla_t\sigma_{st} + \dot{m}(\mathbf{U}_l - \mathbf{u}_B) \cdot \mathbf{n}. \tag{4.3.25}$$

The scalar product of equation (4.3.25) with the interfacial normal vector $\mathbf{n}$ gives

$$-p_l(R,t) + 2\mu_l\frac{\partial U_{l,r}(r,t)}{\partial r}\Big|_{r=R} + p_B(t) = \frac{2\sigma_{st}}{R} + \dot{m}\left(U_{l,r}(R,t) - u_{B,r}(r,t)\right). \tag{4.3.26}$$

The second term is determined from equation (4.3.16), as

$$\frac{\partial U_{l,r}}{\partial r}\Big|_{r=R} = -\frac{2}{R(t)}\dot{R}(t),$$

and the velocities that appear in the last term are rewritten with help of equations (4.3.9) and (4.3.10), as

$$U_{l,r}(R,t) = \frac{\dot{m}}{\rho_l} + \dot{R}(t),$$

$$u_{B,r}(R,t) = \frac{\dot{m}}{\rho_B} + \dot{R}(t).$$

Therefore the liquid pressure at the bubble surface is

$$p_l(R,t) = -4\mu_l\frac{\dot{R}(t)}{R(t)} + p_B(t) - \frac{2\sigma_{st}}{R(t)} - \dot{m}^2\left(\frac{1}{\rho_l} - \frac{1}{\rho_B}\right). \tag{4.3.27}$$

27

The final form of the Rayleigh-Plesset equation

Combining equations (4.3.20) and (4.3.27) yields the Rayleigh-Plesset equation,

$$R(t)\ddot{R}(t) + \frac{3}{2}\dot{R}^2(t) = \frac{p_B(t) - p_l(\infty, t)}{\rho_l} - 4\nu_l \frac{\dot{R}(t)}{R(t)} - \frac{2\sigma_{st}}{\rho_l R(t)} - \dot{m}^2 \frac{1}{\rho_l}\left(\frac{1}{\rho_l} - \frac{1}{\rho_B}\right), \quad (4.3.28)$$

where $p_l(\infty, t) = p_0 + p(t)$.

4.3.2 Bubble dynamics in the cavitation bubble model

When modelling bubble dynamics with the cavitation bubble model, the bubbles evolve in space in a finite domain. Their trajectory is solved with the Discrete Bubble Model (section 3.2) and their dynamics is solved with a modified version of equation (4.3.28). In this equation, the mass flow rate through the interface is neglected, and the varying pressure far from the bubble, $p(t)$, is replaced by the liquid pressure at the bubble position, $p_l(\mathbf{x}_B, t)$ because it is more representative of the pressure variations seen by the bubble along its trajectory. Therefore, the modified equation is given as

$$R(t)\ddot{R}(t) + \frac{3}{2}\dot{R}^2(t) = \frac{p_B(t) - p_0 - p_l(\mathbf{x}_B, t)}{\rho_l} - 4\nu_l \frac{\dot{R}(t)}{R(t)} - \frac{2\sigma_{st}}{\rho_l R(t)}. \quad (4.3.29)$$

The presence of non-condensable gas

Moreover, the bubble contains water vapour and a non-condensable gas of which the mass is assumed constant during the evolution of the bubble size. The presence of the gas ensures that a collapsing bubble cannot disappear, i.e. $R(t) > 0$. The collapse phase ends when the compression stops, and is followed by a rebound of the bubble. The pressure inside the bubble, $p_B(t)$, is the sum of the saturated vapour pressure p_v and the gas pressure $p_g(t)$. The gas pressure is related to the equilibrium state gas pressure p_{g0}, at (R_0, p_0), as $p_g(t) = p_{g0}\left(\frac{R_0}{R(t)}\right)^{3\gamma}$. Moss [50] suggested to use different values for the polytropic coefficient γ during the process of growth and collapse. The bubble growth phase preceding a collapse is sufficiently slow to be assumed isothermal and during this process, when $R \geq R_0$, γ is unity. On the other hand, the collapse occurs within an extremely short time, therefore the compression of gas is assumed adiabatic during this phase, and γ takes the value of the ratio of the heat capacities of the gas, $\gamma = 1.4$, when $R < R_0$.

Equations (4.3.29) at the equilibrium state, (R_0, p_0), gives the gas pressure p_{g0} as

$$p_{g0} = p_0 + \frac{2\sigma_{st}}{R_0} - p_v. \quad (4.3.30)$$

The initial equilibrium radius

In practice, the known parameters to solve equation (4.3.29) are the initial radius R, the initial liquid pressure interpolated at the location $\mathbf{x}_B$ and the reference pressure p_0. It is important to make sure that the bubble is initially in equilibrium in order to avoid unphysical

oscillations at the beginning of the bubble lifetime. It is therefore necessary to determine the equilibrium radius R_0 corresponding to the reference pressure p_0 which satisfies the condition

$$R_0^{3\gamma} + \frac{2\sigma_{st}}{p_0 - p_v} R_0^{3\gamma-1} + \frac{R^{3\gamma}}{p_0 - p_v}\left(p_v - \frac{2\sigma_{st}}{R} - p_l(\mathbf{x}_B, t)\right) = 0. \tag{4.3.31}$$

The pressure wave

The collapse and rebound intensity may be estimated with the value of the pressure of the acoustic wave radiated by the bubble. It is estimated by Mettin et al. [44] as

$$p_a(r) = \frac{\rho_l}{r}(R^2\ddot{R} + 2R\dot{R}^2), \tag{4.3.32}$$

where $r \geq R$ is the distance from the center of the bubble.

Chapter 5

The new multi-scale model

The VOF method, presented in section 3.1, is suitable for modelling large resolvable vapour structures, such as sheet cavitation. The drawback of this method is that it can not describe structures that are smaller than the cell size. A significantly higher mesh resolution is required to capture the small cavitation bubbles that are present in the case of cloud cavitation. If also the bubble dynamics at the collapse phase is to be resolved by VOF (and in that case also including compressibility effects), the required mesh resolution would rapidly grow out of reach. That is the reason why results are not sufficiently accurate regarding the breakup process when bubble clouds are formed and advected with the VOF method. Therefore, the VOF method with the mass transfer model of Sauer and Schnerr, presented in section 4.2.1, is improved to give a more realistic prediction of the whole range of bubble sizes. Small bubbles are identified from the VOF representation, and transferred to a Lagrangian frame. The small bubbles are treated with the cavitation bubble model, i.e. they are tracked individually with the DBM approach (section 3.2) and the bubble dynamics is resolved by the Rayleigh-Plesset equation (4.3.29), in order to model the collapse of individual bubbles. The interaction between the bubbles is accounted for and the flow is affected by the presence of the bubbles. Furthermore, the bubbles may also be transferred back from the Lagrangian to the Eulerian frame, based on the size of the Lagrangian bubbles or on their distance to the interface of the VOF structures.

The difference with the bubble cavitation model presented in section 4.3.2, is that the fluid properties (ρ_l, ν_l, $\mathbf{U}_l$ and p_l) are replaced by the properties of the mixture (ρ, ν, $\mathbf{U}$ and p), and the fluid phase equations (3.2.8) and (3.2.9) are replaced by equations (3.1.3) and (3.1.4).

The new multi-scale approach uses the strength of the VOF method to model the large structures and the strength of the DBM approach to model the small structures. The bubbles are modelled in a *Lagrangian* framework, and the VOF representation is also referred to as the *Eulerian* framework. The new approach is schematically shown in Figure 5.1 and 5.2, and the methods used for the transition between these frameworks are presented in detail here.
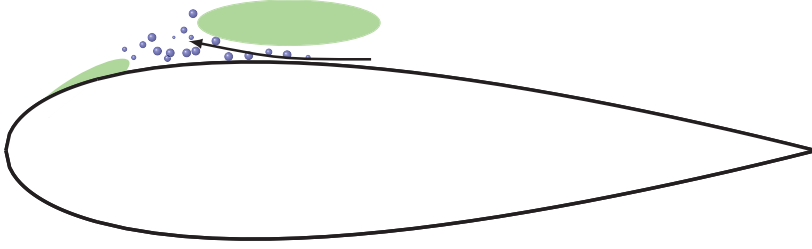
Figure 5.1: Schematic view of the cavitation development on a hydrofoil, with the attached cavity, the re-entrant jet, the shedding cloud and the small Lagrangian bubbles (coloured in blue) that break off the large-scale structures (coloured in green).
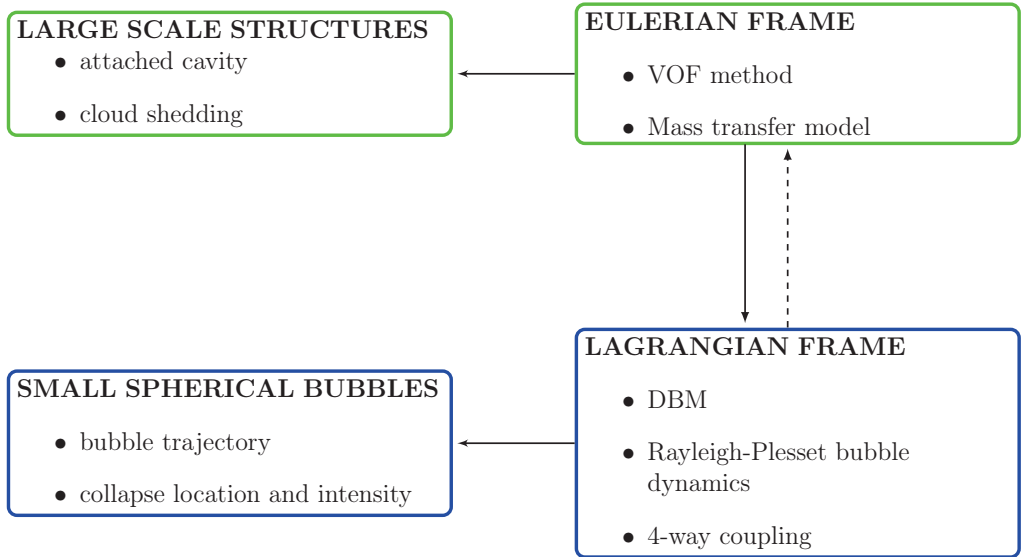

Figure 5.2: Schematic representation of the multi-scale approach.

5.1 Transition from the Eulerian to the Lagrangian frame

Vapour structures that are too small for the VOF resolution requirements, are transformed to Lagrangian bubbles. The strategy used to identify the bubbles is inspired from the technique used by Tomar et al. [71] to identify small droplets created during the breakup of a turbulent liquid jet in gas. At each time step, the droplets are identified with a so-called connected components technique. It consists in associating the adjacent cells for which the liquid volume fraction meets a given criterion. The size of the coherent liquid structure can be estimated, and small structures are transformed into droplets. In the case of breakup of vapour structures, the condition used for the connected components technique is that the the cell contains some vapour, i.e. the liquid volume fraction is below a threshold value, $\alpha_{lim} < 1$. The adjacent cells that fulfill this condition are stored together with the number of the coherent structure (bubbleID) they belong to. The algorithm efficiency is optimised by using a hash table, which is a table with two parameters, a key and an associated value. Here the key is the cell label and the value is its bubbleID. In this way, it is easy and fast to retrieve data (cell label) because the search algorithm does not use time consuming loops. Once the bubble identification is completed, the bubbles that are too small to be resolved by VOF are converted to Lagrangian bubbles.

A given minimum numbers of connected cells are required to represent the smallest vapour structure. This threshold value is denoted N_{E-L}, and it is thus assumed that any vapour structure described in the Eulerian frame by less than N_{E-L} cells is a candidate for being handled in the Lagrangian frame.

The position, size and velocity of the identified bubbles are deduced from the Eulerian data and the vapour volume fraction is removed from the VOF representation. These bubbles are small enough to be considered as spherical due to the surface tension. Therefore, their diameter is derived from the equivalent volume of a sphere.

5.1.1 Algorithm

The algorithm of the coupling method implemented in the OpenFOAM C++ library is here presented in detail.

- Create a list (L) of cells that contains vapour. i.e. with $\alpha < \alpha_{lim}$.

- Identify coherent structures:

  1. Initialise bubbleID counter (maxID=0).
  2. Create a hash-table HT that will contain the couples (cell label, bubbleID).
  3. For all cell$_i$ ∈ (L), create a list (Ln) of neighbours.
     (a) If none element of (Ln) is a key of HT,
         i. Add cell$_i$ label as a new key in HT, with value bubbleID= maxID,
         ii. Increment maxID.
     (b) If only one element of (Ln), (cell$_k$), is a key of HT,
         i. Get the value bubbleID$_k$ associated to the key cell$_k$,
         ii. Add cell$_i$ label as a new key in HT, with value bubbleID= bubbleID$_k$.

(c) If several elements of (Ln), ($cell_k$, k=1:K; K>1), are keys in HT
   i. Get the values {$bubbleID_k$, k=1:K} associated to the keys {$cell_k$, k=1:K},
   ii. Find the minimum value minID=min($bubbleID_k$, k=1:K),
   iii. Add $cell_i$ label as a new key in HT, with value bubbleID= minID.
   iv. For all elements of (Ln) with associated value ($bubbleID_k >$ minID) in HT, change the value to minID in HT (i.e. $cell_i$ connects coherent structures together)

- For each coherent structure identified, get its properties:

  1. Create a list (L_B) of cell labels {$cell_j$, j=1:J}, associated to the same bubbleID in HT.

  2. If $J < N_{E-L}$ (i.e. the structure is too small to be described by the Eulerian approach),

  3. Evaluate the bubble volume, $V_B = \sum_j (1 - \alpha[cell_j]) V[cell_j]$.

  4. Evaluate the bubble centroid position, $\mathbf{x}_B = \frac{1}{V_B} \sum_j \mathbf{x}[cell_j](1 - \alpha[cell_j]) V[cell_j]$.

  5. Evaluate the bubble velocity, $\mathbf{U}_B = \frac{1}{V_B} \sum_j \mathbf{U}[cell_j](1 - \alpha[cell_j]) V[cell_j]$.

  6. Evaluate the bubble radius, $R = \left(\frac{3V_B}{4\pi}\right)^{\frac{1}{3}}$.

  7. Add the bubble in the Lagrangian cloud.

  8. Delete the corresponding structure from the VOF simulation, $\alpha[cell_j] = 1$, j=1:J.

5.2 Transition from the Lagrangian to the Eulerian frame

A bubble described in the Lagrangian frame may become very large. It can happen after coalescence or due to an explosive growth when the bubble is subjected to a pressure lower than its critical pressure.

Bubbles that are too large for the DBM requirements, or large enough to be tracked by VOF, should be moved to the Eulerian framework. The criterion for this is that the bubble has a volume larger than a group of N_{L-E} neighbouring Eulerian cells, where the innermost cell hosts the bubble centroid. The threshold value N_{L-E} is a model parameter that is chosen larger than N_{E-L}. Thus, the Lagrangian bubbles can grow, and it is possible to capture the collapse and rebounds following the growth phase.

The transition from Lagrangian to Eulerian also happens when a bubble comes close enough to the Eulerian isosurface where $\alpha = 0.5$. The method to determine if a bubble is close to an Eulerian isosurface consists in estimating the location of the Lagrangian bubble surface at the six points with coordinates ($x_B \pm R, y_B \pm R, z_B \pm R$). If $\alpha \leq 0.5$ in any of those points, the Lagrangian bubble is in contact with a resolved vapour structure, and is converted to the Eulerian representation.

The method for the conversion from the Lagrangian to the Eulerian framework consists in filling with vapour the cell hosting the centroid $\mathbf{x}_B$ and its closest neighbours. The number of cells concerned depends on the volume V_B and also on the volume available in these cells that can be converted into vapour.

Chapter 6

Unpublished results

This chapter presents results that are not included in the appended papers.

6.1 Liquid jet breakup

Numerical simulations of the breakup of a liquid jet were performed to assess the performance of the VOF method and the requirements in term of order of discretization schemes and grid size. A liquid jet that is injected into a chamber interacts, due to friction forces, with the surrounding gas. Vortical structures are formed in the gas which again interact with the jet. Instabilities caused by aerodynamic forces wrinkle the jet on the surface and lead it to disintegrate at some point downstream. This yields the formation of relatively large irregular liquid structures which break up further downstream into smaller more spherically shaped droplets. This process of forming a spray from a liquid jet is of industrial interest, for instance for Diesel fuel injection, injection in gas turbines or for spray drying.

The geometrical set-up is shown in Figure 6.1. The inlet diameter is $D = 10^{-4}$ m, the inlet velocity $U_{in} = 500$ m/s, the density and viscosity liquid/gas ratio are $\rho_l/\rho_g = 10$ and $\mu_l/\mu_g = 3.419$, respectively. It yields a Reynolds number $Re = 14964$ and a Weber number $We = 10000$.

The breakup of the liquid jet has been simulated with LES for the turbulence, and the VOF method to handle the two phases of the flow. Simulations performed with OpenFOAM are compared to simulations performed with an in-house code, which uses high order finite differences. The in-house simulations and the analysis of the results were performed by H. Grosshans [23, 24]. The order of discretization used in the computations are listed in Table 6.1 and the simulations are performed for different grid resolutions : 10, 20 and 40 cells/D. Figure 6.2 shows the instantaneous picture of the jet at the non-dimensional time $t\star = tU_{in}/D = 14.2$, for the high order cases and the different grid resolutions. The in-house code creates a larger amount of small liquid structures. The length of the liquid penetration, in Figure 6.3, shows that the results for the low order case in the in-house code is similar to the OpenFOAM cases. They predict a linear liquid penetration and no breakup in the domain, while the high order cases in the in-house code suggest that the jet breaks-up and the penetration length converges to $24D$. Differences in the results of both simulations lead back to the different numerical implementations. It highlights that the OpenFOAM 2nd order discretization schemes create high numerical diffusion and dampen instabilities. However,

the major instabilities that cause the jet breakup are captured with OpenFOAM with a higher grid resolution.
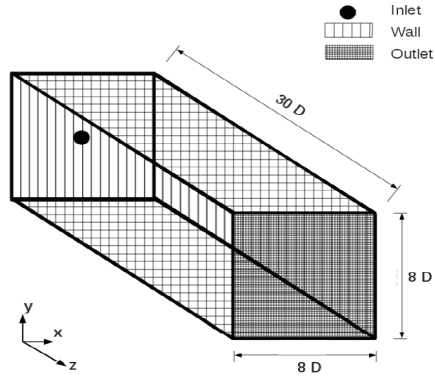

Figure 6.1: Geometrical set-up.

	OpenFOAM	in-house
High order	2 nd order schemes	convective term, 3rd order, pressure and diffusive term 4^{h} order, time derivatives 2nd order
Low order	1 nd order schemes	convective term, 1rd order, pressure and diffusive term 2^{h} order, time derivatives 1nd order

Table 6.1: Discretization schemes used for both solvers.
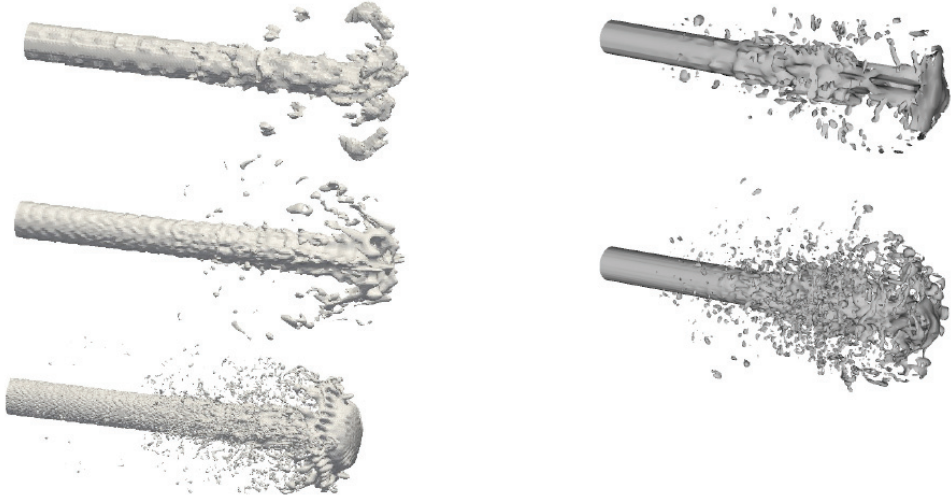
Figure 6.2: Iso-surface $\alpha = 0.5$ of the liquid volume fraction. (left) Results from Open-FOAM for different resolutions: 10 (top), 20 (middle) and 40 (bottom) cells/ D. (right) Results from the in-house code for different resolutions: 10 (top) and 20 (middle) cells/ D.
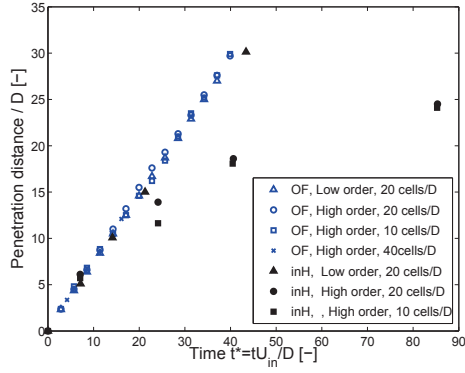
Figure 6.3: Penetration distance of the liquid for different cases.

6.2 Nuclei distribution and its effects on the cavity shape

In paper III, simulations were performed on a two-dimensional NACA profile in order to study the nuclei distribution. The model accounted only for drag and buoyancy forces. A similar simulation is performed with a model that accounts for all the forces described in equation (3.2.6). N_{in}=500 bubbles with properties ($\rho_B = 1$ kg/m^3, $D = 50\mu m$), are injected per time step at a distance $1.5c_0$ in front of the hydrofoil, where c_0 is the chord length. The averaged nuclei distribution is sampled on the vertical line that goes through the lowest pressure region. Figure 6.4 shows the average nuclei distribution when accounting for all the forces in equation (3.2.6) compared to the case where only drag and gravity forces are included. The results suggest that the nuclei distribution is strongly influenced by forces other than drag and buoyancy.
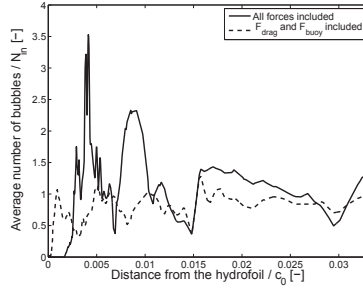

**Figure 6.4:** Sensitivity to forces in the equation of motion.

In paper III, simulations were performed on a two dimensional NACA profile in order to study the effects of a non-uniform nuclei distribution in the mass transfer model of Sauer and Schnerr [62]. The simulations performed on a 3D geometry are presented here. The set-up consists of the 2D case extruded in z-direction, such that the span-wise width is c_0, and the mesh in this direction consists of 50 points uniformly distributed. Symmetry boundary conditions are applied to the front and back of the domain. In Figures 6.5- 6.7, the cavitating case with a uniform distribution of nuclei ($N = 10^8$) is compared with a case where the nuclei concentration is more dense near the hydrofoil ($N = 10^8$ in a layer of thickness $\delta_N = 2$ mm, and $N = 10^2$ everywhere else). The total volume of vapour and the drag and lift coefficients are similar for both cases until t=0.03 s. The discrepancies observed later show that the cavity development is affected by the nuclei distribution. In the uniform case (Figure 6.6), the rear part of the attached cavity is smooth. After the break-off, one roll-up is transported downstream while a new cavity, which has also a smooth rear part, grows. In the non-uniform case (Figure 6.7), the rear part of the attached cavity is irregular. Several small structures are detached and rapidly shrink because of the low content of nuclei in this region (Figure 6.7 (g)-(i)). This explain the lower volume of vapour displayed in Figure 6.5 after t=0.04 s.

These results show that a non-uniform nuclei distribution leads to the formation of sev-

eral small structures instead of a large coherent structure transported downstream. The lack of nuclei in the downstream region makes these small structures disappear rapidly. These features emphasise the importance of the nuclei distribution when modelling cavitation inception and development with the mass transfer model of Sauer and Schnerr.
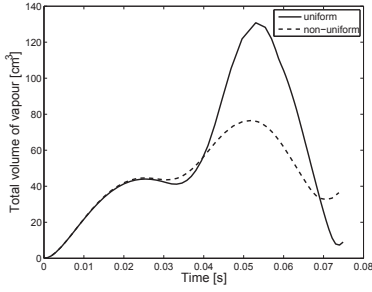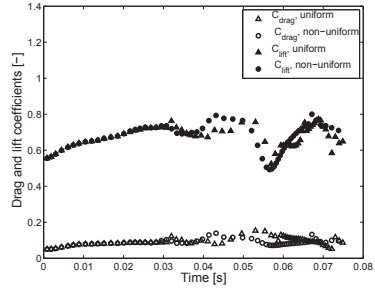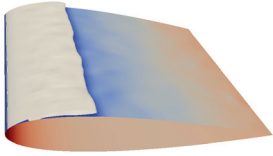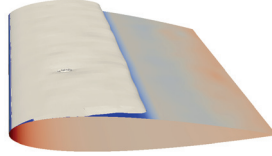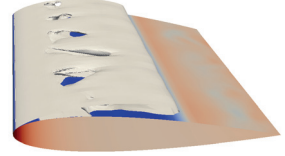

(a)   (b)

Figure 6.5: (a) Total volume of vapour for cavitating flow with different nuclei distribution. (b) Drag and lift coefficients for cavitating flow with different nuclei distribution.
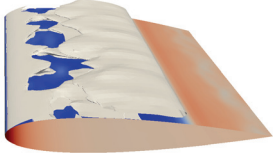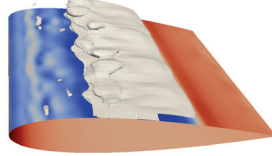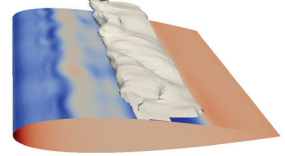
(a) t=0.006 s

(b) t= 0.013 s

(c) t= 0.021 s

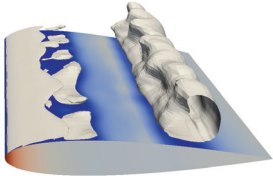(e) t=0.028 s

(f) t= 0.034 s

(g) t= 0.041 s

(h) t=0.047 s

(i) t= 0.052 s

(j) t= 0.058 s

(k) t=0.061 s

(l) t= 0.064 s

(m) t= 0.067 s

(n) t=0.07 s

Figure 6.6: Vapour volume fraction α for an uniform nuclei distribution
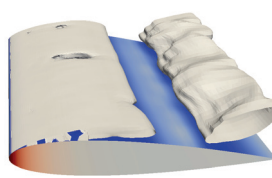
(a) t=0.006 s

(b) t= 0.013 s

(c) t= 0.021 s

(e) t=0.028 s

(f) t= 0.034 s
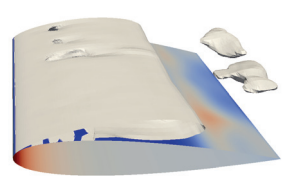
(g) t= 0.041 s
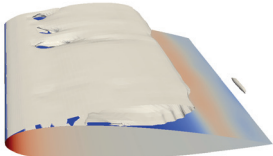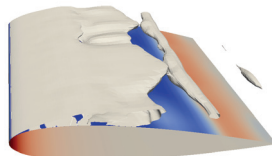
(h) t=0.047 s
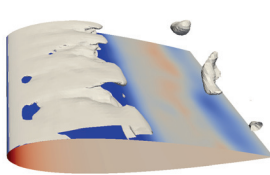
(i) t= 0.052 s
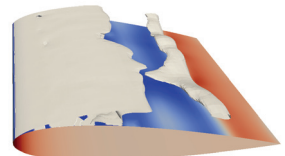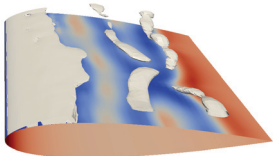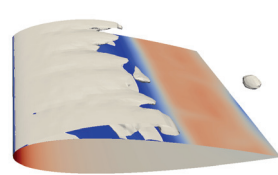
(j) t= 0.058 s
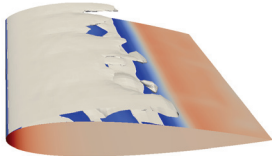
(k) t=0.061 s
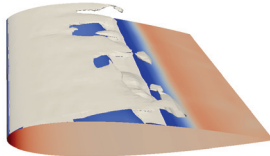
(l) t= 0.064 s
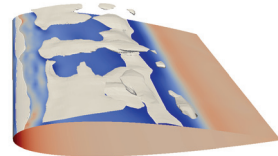
(m) t= 0.067 s
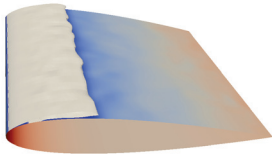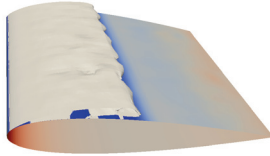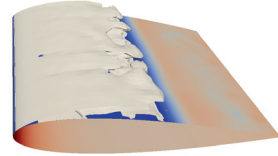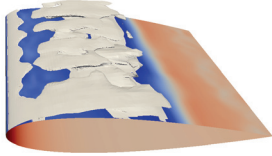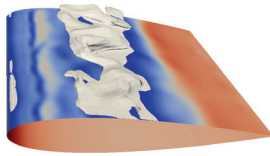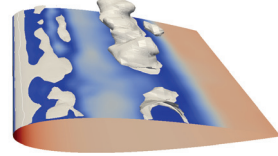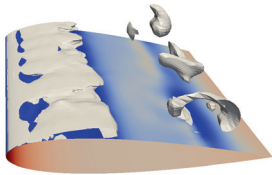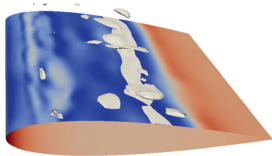
(n) t=0.07 s

Figure 6.7: Vapour volume fraction α for a non uniform nuclei distribution.

Chapter 7

Summary of appended papers

This thesis is based on the following papers.

1. **Numerical and experimental comparisons for rising air bubbles**
   Aurélia Vallier and Johan Revstedt.

   Deforming ellipsoidal air bubbles in water are studied numerically using the Volume-Of-Fluid (VOF) method. The numerical results are compared for different length of the channel and against experimental data. The air volume flow rate and the size of the flow domain are set so that the bubbles are close enough to interact without coalescing. The air bubbles have an equivalent diameter large enough for them to deform without breaking up.

   The bubble behaviour is investigated, in terms of aspect ratio, rise velocity and bubble path. This study shows that the choice of a short channel is valid only for the first 10 bubbles. For the following bubbles, the presence of a closer free surface affects the results. The perturbations of the flow and the detachment are no longer similar and influence the trajectory and the shape of the bubbles.

   Two different methods of obtaining the centroid position are investigated. The error induced by using data from two-dimensional projections is emphasised by comparing with numerical three-dimensional data. It shows that the method used in the experiments is limited to bubbles that are not tilted or deformed from the ellipsoid shape.

   The present work assesses the performance of the numerical solver and illustrates the limitations of the Volume-Of-Fluid method implemented in OpenFOAM which predicted an unphysical volume loss in the wake of the bubbles. The modification of the surface tension force reduces the volume loss but it affects the shape and the velocity of the bubbles.

   Contribution The candidate performed the simulations with OpenFOAM, the postprocessing of the numerical results and their analysis.

2. **Modelling of bubble dynamics related to cavitation**
   Aurélia Vallier, Johan Revstedt and Håkan Nilsson.

Modelling bubble dynamics is numerically challenging because the collapse occurs in a very short time and involves large variations of the growth rate and radius. In this work, the Rayleigh-Plesset equation is implemented and solved with an appropriate time adaptive integration method, the embedded Rosebrock method. The importance of the critical equilibrium state for modelling bubble dynamics is illustrated with examples of bubbles growing without limit. The accuracy of the method requires a correct equilibrium state (R_0, p_0) of the bubble. Therefore, a method for estimating the equilibrium radius R_0 at release location is derived and validated in order to avoid bubble size oscillations at the beginning of the computations. The performance of the present model is assessed by considering results from previous studies. The agreement between numerical and experimental data depends on the set of parameters chosen to resolve the Rayleigh-Plesset equation. In particular the value of the liquid viscosity influences the bubble size at rebound R_{reb}. According to the classical approach used to estimate the intensity of the collapse, the dissipated energy depends on the value R_{reb}. While this approach is valid with experimental data, it is not reliable in the context of numerical calculations because the results obtained depend on the model parameters.

The bubble dynamics model is included in an algorithm modelling the bubble transport in the flow using a Discrete Bubble Model. A study is performed to analyse the effects of the force F_{vol} which accounts for the volume variation of the bubbles in the transport equation. This force yields unphysical deviations of the trajectory of collapsing bubbles. Therefore its contribution should not be included in the computations of the transport of collapsing bubbles.

The overall model is implemented in OpenFOAM in order to simulate the trajectory of small bubbles and capture their expansion and collapse near the surfaces. The present work emphasises the influence of the ambient pressure, the initial size of the bubbles, their release position, as well as the flow features. The results provide information about the regions that are most exposed to successive collapses as well as the collapse intensities.

Contribution The candidate implemented all the models described in the paper in a new solver in OpenFOAM. The candidate performed the simulations, the post-processing of the numerical results and their analysis.

3. **Mass transfer cavitation model with variable density of nuclei**
   Aurélia Vallier, Johan Revstedt and Håkan Nilsson.
   7th International Conference on Multiphase Flow, ICMF 2010, Tampa, Florida, 2010

The Sauer and Schnerr mass transfer model assumes a uniform nuclei distribution despite measurements of the non-homogeneous nucleus population. First, computations are performed to study the nuclei distribution over a NACA0015 hydrofoil. The nuclei in the liquid phase are modelled with a Lagrangian Particle Tracking method. It is shown that the nuclei accumulate at the leading edge close to the low pressure region. However the nuclei are not present on average in the boundary layer.

The Sauer and Schnerr model is modified to take into account the observed non-uniform nuclei density. It does not yield attached cavitation. It means that the transported

nuclei influence is not as important as the one of the surface nuclei for cavitation inception, at least when using the present mass transfer model. Then, the performance of the modified model is investigated with a higher nuclei concentration near the surface. The attached cavity is shorter, the re-entrant jet is faster and thinner, and the cloud is stretched. A thin layer of vapour links the attached cavity and the cloud of vapour. The shape of the sheet cavity and the volume of vapour are affected by the nuclei content. These features emphasise the importance of the nuclei distribution when modelling cavitation inception and development with this mass transfer model.

Contribution The candidate implemented the model described in the paper in a new solver in OpenFOAM. The candidate performed the simulations, the post-processing of the numerical results and their analysis.

4. **Numerical procedure for simulating the break-up of cavitation sheet**
Aurélia Vallier, Johan Revstedt and Håkan Nilsson.
4th International meeting on Cavitation and Dynamic Problems in Hydraulic Machinery and Systems, Belgrade, Serbia, 2011.

Mass transfer cavitation models based on the Volume-Of-Fluid method (VOF) have a limitation of the resolution due to the grid size. Bubbles smaller than the control volumes can not be resolved. A new multi-scale approach is developed in the present work, which can model the presence of bubbles smaller than the grid size. The principle is to couple the VOF method with a two-way coupled Discrete Bubble Model. This multi-scale approach switches from an Eulerian to a Lagrangian frame in order to account for the small bubbles that a pure VOF method cannot simulate. An algorithm for identifying small bubbles is developed and tested on two simple cases of an air bubble breaking up under the impact of a water jet. The results show that the model successfully captures the formation of small bubbles and gives a better description of the liquid/vapour mixture.

Contribution The candidate implemented the model described in the paper in a new solver in OpenFOAM. The candidate performed the simulations, the post-processing of the numerical results and their analysis.

5. **A new multi-scale approach for modelling cavitation on hydrofoils**
Aurélia Vallier, Johan Revstedt and Håkan Nilsson.

A model based on a VOF method can not describe structures that are smaller than the cell size. Therefore, it can not model the small cavitation bubbles without investing an enormous computational effort. These bubbles are present in the case of cloud cavitation and influence the global dynamic of the flow. For this type of cavitation, tracking individual bubbles is more relevant. In order to improve the existing mass transfer cavitation model based on VOF method, a new multi-scale method is developed. This multi-scale approach switches from an Eulerian to a Lagrangian frame in order to account for the small bubbles that a pure VOF method can not simulate. An algorithm for identifying the small Lagrangian bubbles is presented. The collision events are described by a deterministic model, the bubble dynamics is resolved with

a Rayleigh-Plesset equation, the bubbles affect the flow, and the transition from the Lagrangian to the Eulerian frame is also included.

The multi-scale model is applied to a cavitating hydrofoil and describes the re-entrant jet that breaks up the attached cavity and yields the formation of Lagrangian bubbles. The importance of the bubble interactions and their influence on the flow are highlighted by comparing the bubble distribution for different cases. The bubble locations at first collapse, the bubble trajectories and the pressure waves emitted during the collapses and rebounds, are studied in this work. They are crucial features for predicting erosion damages on the hydrofoil surface. However, these features are computationally expensive to post-process. A more efficient approach consists in studying the residence time of the bubbles, it gives a good estimation of the regions exposed to successive collapses and rebounds. The multi-scale approach is an improvement to the modelling of the transition from sheet to cloud cavitation.

Contribution The candidate implemented the model described in the paper in a new solver in OpenFOAM. The candidate performed the simulations, the post-processing of the numerical results and their analysis.

Chapter 8

Conclusions and future work

Conclusions   This work is aimed to improve the numerical models for cavitation inception and development on a hydrofoil. The focus lies on numerical methodologies that include the broad range of cavity sizes, using appropriate models for each specific phenomenon

For the large structures, the VOF method has been studied for two cases of non-cavitating flow, large bubbles rising in a water channel (paper I) and a liquid jet in a gas chamber (section 6.1). These studies highlighted the limitations of the VOF method implemented in OpenFOAM. It requires a high grid resolution to obtain accurate results. In the case of the rising bubbles, unphysical volume loss has been observed in the wake of the bubbles, and the error could be decreased with a finer mesh or with a modification of the surface tension force. In the case of the liquid jet, the 2nd order discretization schemes created high numerical diffusion and dampen instabilities, such that the method predicted erroneously a linear liquid penetration and no breakup in the domain. However the major instabilities that cause the jet breakup are captured with OpenFOAM with a high grid resolution.

The behaviour of the predicted cavitation on a hydrofoil has been investigated, using the VOF and Sauer and Schnerr mass transfer model in OpenFOAM (paper III). The importance of the nuclei distribution has been emphasised, when modelling cavitation inception and development. A non-uniform nuclei distribution lead to the formation of several small structures instead of a large coherent structure transported downstream. The lack of nuclei in the downstream region made these small structures disappear rapidly.

For the small spherical bubbles, the Rayleigh-Plesset bubble dynamics model has been investigated under academic and realistic conditions, in paper II. It has been shown that the accuracy of the method requires a correct equilibrium state (R_0, p_0) of the bubble. Therefore, a method for estimating the equilibrium radius R_0 at release location was derived and validated in order to avoid bubble size oscillations at the beginning of the computations. This study showed also that the agreement between numerical and experimental data depends on the set of parameters chosen to resolve the Rayleigh-Plesset equation. In particular the value of the liquid viscosity influences the bubble size at rebound R_{reb}. According to the classical approach used to estimate the intensity of the collapse, the dissipated energy depends on the value R_{reb}. While this approach is valid with experimental data, it is not reliable in the context of numerical calculations because the results obtained depend on the model parameters. Furthermore, the simulations successfully described the collapse and the following rebounds, but it appeared that the value of the growth rate at collapse may become larger than the speed of sound. In this case, the assumption of incompressibility is theoretically not applicable anymore.

For the small spherical bubbles, the DBM model has been used to study the distribution of nuclei over a NACA0015 hydrofoil (paper III and section 6.2). The results suggested that the nuclei distribution is strongly influenced by forces other than drag and buoyancy. The DBM model has also been used together with the bubble dynamics model in paper II. It showed that the force F_{vol} which accounts for the volume variation of the bubbles in the transport equation, yields unphysical deviations of the trajectory of collapsing bubbles. Therefore its contribution should not be included in the computations of the transport of collapsing bubbles.

In order to improve the existing mass transfer cavitation model based on the VOF method, a new multi-scale method has been developed. This multi-scale approach switches from an Eulerian to a Lagrangian frame in order to account for the small bubbles that a pure VOF method can not simulate. An algorithm for identifying Lagrangian bubbles have been implemented in OpenFOAM. This interaction between the VOF and DBM methodologies has been first evaluated in the non-cavitating case of a large bubble that breaks up under a liquid jet (paper IV). Then, in paper V, the approach is completed with other features: the bubble dynamics is resolved using the Rayleigh-Plesset equation, the collision events are described by a deterministic model, the bubbles affect the flow, and the transition from the Lagrangian to the Eulerian frame is included. The multi-scale approach is applied to a cavitating hydrofoil and describes the re-entrant jet that breaks the attached cavity and yields the formation of Lagrangian bubbles. The importance of the bubble influence on the flow and the bubble interactions are highlighted by comparing the bubble distributions and the cavity shape for different cases. The locally dense concentration of bubbles was observed and justify the use of a 4-way coupling approach. However, the conversion of the small bubbles back to the Eulerian frame, was shown to have a negligible effect on the results. The bubble locations at their first collapse, the bubble trajectories, and the pressure wave emitted during the collapses and rebounds are crucial features for predicting erosion damages on the hydrofoil surface. However, these features are computationally expensive to post-process. A more efficient approach consists in studying the residence time of the bubbles, which gives a good estimation of the regions exposed to successive collapses and rebounds. The multi-scale approach is therefore an improvement to the modelling of the transition from sheet to cloud cavitation and the modelling of cavitation erosion risk.

Future work The following features are suggested to be considered in future work in order to improve further the modelling of cavitation.

- The performance of the VOF method could be further investigated. Higher discretization schemes could be used in order to reduce numerical diffusion and interface smearing. Beside the choice of robust and accurate schemes, it would be interesting to use the recent developments performed in this field by the OpenFOAM community. For instance, the Coupled-Level-Set-Vof method of [46] has been implemented, and using this approach would give a more accurate representation of the interface.

- The compressibility effect could be included in the Rayleigh-Plesset equation, by using the equation proposed by Keller and Miksis [36]. It would give a more realistic description of the dynamic behaviour at collapse, and it would account for radiation damping.

- The new multi-scale model depends on several parameters, and their effects on the results need further investigations. The choice of the criterion α_{lim}, N_{L-E} and N_{L-E} affect the bubble distribution, and consequently the flow and the shape of the large-scale structures. The sensitivity of the size of the Lagrangian and Eulerian cells is also important.

- The collapse and rebounds of the bubbles when they reach a region of higher pressure generate pressure waves that influence the collapse of the surrounding bubbles, causing a chain reaction that amplifies the erosive process. These interactions are important features that should be included as a source term (the secondary Bjerknes force) in the Rayleigh-Plesset equation. This would improve the prediction of erosion damages.

- It would be interesting to apply the multi-scale model to a complex geometry, such as a water turbine, in order to model accurately the cavitating flow and predict the effects of the bubble collapses in a real application.

Bibliography

[1] Arndt R., Wosnik M., Experimental and Numerical Investigation of Large Scale Structures in cavitating Wakes, 36th AIAA Fluid Dynamics Conference and Exhibit 2006, 3046.

[2] Arora, M., Ohl, C.D. and Lohse, D., Effect of Nuclei Concentration on Cavitation Cluster Dynamics, J. Acoust. Soc. Am. 121, 34323436, 2007.

[3] Auton T.R., The lift force on a spherical body in a rotational flow. J. Fluid Mech. **183**, 199-218, 1987.

[4] Benjamin T. B. and Ellis A.T., The collapse of cavitation bubbles and the pressures thereby produced against solid boundaries, Phil. Trans. R. Soc. Lond. A, **260**, 221-240, 1996.

[5] Blake J.R. and Gibson D.C., Cavitation bubbles near boundaries, Ann.Rev Fluid Mech., **19**, 99-123, 1987.

[6] Boussinesq J., Théorie analytique de la chaleur, Gauthier-Villars Paris, **2**, 1903.

[7] Brackbill J.U., Kothe D.B., Zemach C., A continuum Method for Modeling surface Tension, J. Comp. Phys., 100, 335-354, 1992.

[8] Brennen C. E., Cavitation and Bubble Dynamics, New York Oxford University Press, 1995.

[9] Brujan E.A., Ikeda T and Matsumoto Y., Jet formation and shock wave emission during collapse of ultrasound-induced cavitation bubbles and their role in the therapeutic applications of high-intensity focused ultrasound, Phys. Med: Biol, **50**, 4797-4809, 2005.

[10] Chesters, A.K., The modeling of coalescence processes in fluid-liquid dispersions - a review of current understanding. Trans. I. Chem. E 69 (part A), 353-361, 1991.

[11] Chesters, A.K., Hofman, G.,Bubble coalescence in pure liquids. Appl. Sci. Res. 38, 353-361, 1982.

[12] Darwish M. and Moukalled F., Convective Schemes for Capturing Interfaces of Free Surface Flow on Unstructured Grids. Numerical Heat Transfer B, **49**, 19-42, 2006.

[13] Duineveld P.C., Bouncing and coalescence of two bubbles in water, PhD. thesis, University of Twente, the Netherlands, 1994.

[14] Elghobashi S., An updated classification map of particle-laden turbulent flows, Proceedings of the IUTAM Symposium on Computational Multiphase Flow, 3-10, 2006.

[15] Escaler X., Egusquiza E., Farhat M., Avellan F., Coussirat M., Detection of cavitation in hydraulic turbines, Mechanical systems and signal processing, 837-1007, 2006

[16] Franc J.-P., Physics and Control of Cavitation, Design and Analysis of High Speed Pumps, **2**, 1-36, 2006

[17] Franc J-P., Michel J.M., Cavitation erosion research in France:the state of the art, J. Mar Sci Technology (1997) 2:233-244.

[18] Franc J-P., Partial Cavity Instabilities and Re.Entrant Jet, CAV2001: lecture002.

[19] Giannadakis E. , Papoulias D. , Gavaises M. and Arcoumanis C. , Evaluation of the Predictive Capability of Diesel Nozzle Cavitation Models, SAE Paper 2007-01-0245.

[20] Göde, Performance Upgrading of Hydraulic Machinery with the Help of CFD, Notes on Numerical Fluid Mechanics and Multidisciplinary Design, **100**, 2009.

[21] Gosset, A, Evaluation of the cavitatingFoam solver for low mach number flow around a 2D hydrofoil, Fifth OpenFOAM Workshop, Sweden 2010.

[22] Grekula, M., Cavitation Mechanisms related to erosion, Studies on Kaplan turbines, foils and propellers, PhD thesis, Chalmers University of Technology, 2010.

[23] Grosshans H, Vallier A.., Revstedt J. and Fuchs L., Numerical Simulation of the breakup of a liquid jet using the OpenFOAM VOF method and comparison to an In-House code, 6th OpenFOAM WorkShop, PennState University, USA, 2011.

[24] Grosshans H., Large Eddy Simulation of Atomizing Sprays, PhD thesis, Lunds University, 2013.

[25] Haberman W.L. and Morton R.K., An experimental investigation of the drag and shape of air bubble rising in various liquids , David Taylor Model Basin Rep. No. 802, 1953.

[26] Higashi S., Yoshiki Yoshida Y., and Tsujimoto Y., Tip Leakage Vortex Cavitation from the Tip Clearance of a Single Hydrofoil, CAV2001, session A6.

[27] Hirshi R., Dupont P, Avellan F., Favre J-N., Guelich J-F., Handloser W. and Parkinson E, Centrifugal pump performance drop due to leading edge cavitation: numerical predictions compared with model tests, Journal of Fluids Engineering 120, 705.711, 1998.

[28] Hirt, C.W. and Nichols, B.D., Volume of Fluid (VOF) Method for the Dynamics of Free Boundaries, J. Comp. Phys., **39**, 201-225, 1981.

[29] Hsiao C.-T., Chahine G.L. and Liu H.-L., Scaling effect on bubble dynamics in a tip vortex flow: prediction of cavitation inception and noise., Dinaflow, 2000.

[30] Huuva T., Cure A., Bark G. and Nilsson H., Computations of unsteady cavitating flow on wing profiles using a volume fraction method and mass transfer models, Proceedings of the 2nd IAHR International Meeting of the Workgroup on Cavitation and Dynamical Problems in Hydraulic Machinery and Systems, Scientific Bulletin of the "Polytechnica" University of Timisoara, Romania. Transactions on Mechanics, **52**(66) 21-34, 2007.

[31] Ingvarsdottir H, Ollivier-Gooch C., Green S., CFD Modeling of the Flow Around a Ducted Tip Hydrofoil. ASME Joint U.S.-European Fluids Engineering Conference, Montreal, July 2002.

[32] Jasak H., Weller H.G., Interface tracking capabilities of the Inter-Gamma differencing scheme, 1995.

[33] Jasak H, Weller H.G. and Gosman A.D., High resoluton NVD differencing scheme for arbitrarly unstructured meshes, Int. J. Numer. Meth. Fluids, 31, 431-449, 1999.

[34] Johnson V. E. and Hsieh T., The influence of the trajectories of gas nuclei on cavitation inception in a line vortex flow, Proc. Sixth Symp. Naval Hydrodyn., 163-179. Office of Naval Research, Washington, DC, 1966.

[35] Kaps P., Rentrop P, Generalized Runge-Kutta Methods of Order Four with Stepsize Control for Stiff Ordinary Differential Equations, Numerische Mathematik, **33**, 55-68, 1979.

[36] Keller J. B. and Miksis M., Bubble oscillations of large amplitude, J. Acoust. Soc. Am. 68, 628-633 , 1980.

[37] Kubota, A., Kato, H. and Yamaguchi, H., A New Modelling of Cavitating Flows: A Numerical Study of Unsteady Cavitation on a Hydrofoil Section, J. Fluid Mech., **240**, 59-96,1992

[38] Kunz, R.F., Boger, D.A., Stinebring, D.R., Chyczewski, T.S., Gibeling, H.J., T.R. Govindan,Multi-Phase CFD Analysis of Natural and Ventilated Cavitation About Submerged Bodies, ASME Paper FEDSM99-7364, ProceedingsrdASME/JSME Joint Fluids Engineering Conference, 1999.

[39] Kunz, R.F., Boger, D.A., Stinebring, D.R., Chyczewski, T.S., Lindau, J.W., Gibeling, H.J., Venkateswaran, S., and T.R. Govindan, A Preconditioned Navier-Stokes Method for Two-Phase Flows with Application to Cavitation Predication, Computers and Fluids, **29**, 849-875, 2000.

[40] Kunz R.F., Lindau J., Kaday T. A., Peltier L. J., Unsteady RANS and Detached Eddy simulations of cavitating flow over a hydrofoil, Fifth International Symposium on cavitation CAV2003-OS-1-12.

[41] Lu N-X., Modelling Cavitation Mechanisms Using LargeEddy Simulation, PhD. Thesis, Chalmers University of Technology, Sweden, 2013.

[42] Masato I., Multibubble cavitation inception, Phys. Fluids, **21**, 113302, 2009.

[43] Maxey, M.R. and Riley, J.J., Equation of motion for a small rigid sphere in a nonuniform flow, Phys. Fluids, **26**, 883-889, 1983.

[44] Mettin R., Akhatov I., Parlitz U, Ohl C.D. and Lauterborn W, Bjerknes forces between small cavitation bubbles in a strong acoustic field, Physical review, **56**, 3, 1997

[45] Meier, Numerical and experimental study of large steam-air bubbles injected in a water pool, PhD, Swiss Federal Institute of Technology, Zürich, Switzerland, 1999.

[46] Menard T., Tanguy S. and Berlemont A., Coupling level set/VOF/ghost fluid methods: validation and application to 3D simulation of the primary break-up of a liquid jet, Int. J. Multiphase Flow, **33**, 510Ð524, 2007.

[47] Merkle, C.L., Feng, J., Buelow, P.E.O., Computational Modeling of the Dynamics of Sheet Cavitation, 3rd International Symposium on Cavitation, Grenoble, France. 1998.

[48] Mishima S., Design of Cavitating Propeller Blades in Non-Uniform Flow by Numerical Optimization, 1996.

[49] Morch, K.A., Reflections on cavitation nuclei in water, Phys. Fluids 19, 2007.

[50] Moss W.C., Levantin J.L. and Szeri A.J., A new damping mechanism in strongly collapsing bubbles. Proceedings Mathematical, Physical and Engineering Sciences, **456**, No 2004, 2983-2994, 2000.

[51] Muzaferija S., Peric M., Computation of free-surface flows using interface-tracking and interface-capturing methods, Nonlinear water wave interaction, Computational Mechanics Publivtions, Southampton, 1998.

[52] Noh W.F., Woodward P.R., SLIC (Simple Line Interface Method), Lecture Notes in Physics, **59**, Springer, 1976.

[53] OpenFOAM http://www.opencfd.co.uk/openfoam

[54] Popinet S., An accurate adaptative solver for surface tension driven interfacial flows, J. Comp. Phys., 228 5838-5866, 2009.

[55] Philipp A. and Lauterborn W., Cavitation erosion by single laser-produced bubbles, Journal of fluids Mechanics, **361**, 75-116, 1998

[56] Plesset M.S, Prosperetti A., Bubble dynamics and cavitation. Annu. Rev. Fluid. Mech. **9**, 145-185, 1977.

[57] Podvin B., Khoja S., Moraga F., Attinger D., Model and experimental visualizations of the interaction of a bubble with an inclined wall, Chemical Engineering Science **63**, 1914-1928, 2008.

[58] Popinet S. and Zaleski S., Bubble collapse near a solid boundary: A numerical study of the influence of viscosity., J. Fluid Mech. **464**, 137-163, 2002.

[59] Rayleigh Lord, On the pressure developed in a liquid during the collapse of a spherical void, Phul. Mag.,**34**, 94, 1917.

[60] Reboud JL, Delannoy Y. Two-phase flow modelling of unsteady cavitation. Proceedings of the 2nd International Symposium on Cavitation, Tokyo, Japan, 1994.

[61] Rusche H., Computational fluid dynamics of diversed two phase flows at high phase fraction. PhD thesis, University of London , England, 2002.

[62] Sauer J. and Schnerr G.H., Unsteady cavitating flow- A new cavitating model based on a modified front capturing method and bubble dynamics, Proceedings of 2000 ASME Fluid Engineering Summer Conference, Boston, MA, June 11-15, 2000

[63] Saurel R. and Lemetayer O., A multiphase model for compressible flows with interfaces, shocks, detonation waves and cavitation, J. Fluid Mech, **431**, 239-271, 2001.

[64] Schiller L. and Nauman A.Z., A drag coefficient correlation, Ver. Deut. Ing., **77**, 318-320, 1993.

[65] Senocak I. and Shyy, W. , A Pressure-Based Method for Turbulent Cavitating Flow Computations, Journal of Computational Physics, **176**, 363-383, 2002.

[66] Shams E., Apte S.V., Larde eddy simulation of cavitation inception in a high speed flow over an open cavity, Proc. of the 7th International Symposium on Cavitation, 2009.

[67] Shima A., Studies on bubble dynamics, Shock Waves, **7**, 33-42, 1997.

[68] Sommerfeld M., Bourloutski E and Bröder D., Euler/Lagrange calculations of bubbly flows with consideration of bubble coalescence, Can. J. Chem. Eng. 81, 508-518, 2003.

[69] Stokes, G., On the effect of the internal friction of fluids on the motion of pendulums. Trans. Camb. phil. Soc., 9, 8, 1850.

[70] Tinguely M, Obresckow D., Kobel P., Dorsaz N., deBosset A. and Farhat M., Energy partition at the colapse of spherical cavitation bubbles, Phys. Rev. E, **86**, 4, 2012.

[71] Tomar G., Fuster D., Zaleski S. and Popinet S., Multiscale simulations of primary atomization, Computers & Fluids, **39**(10), 1864-1874, 2010.

[72] Ubbink O. and Issa, R., A method for capturing Sharp Fluid Interfaces on arbitrary meshes, J. Comp. Phys, **153**, 26-50, 1999.

[73] Vogel A. and Lauterborn W., Acoustic transient generation by laser produced cavitation bubbles near solid boundaries, J. Acoust. Soc. Am, **84**, 2, 1988.

[74] Youngs D.L., Time dependent multi-material flow with large fluid distribution, Numerical Methods for Fluid Dynamics, 187-221, 1986

[75] Wallis GB. One-dimensional Two-phase Flow. McGraw-Hill: New York, 1969.

[76] Zalezak S.T., Fully Multi-Dimensional Flux Corrected Transport Algorithms for Fluid Flow, J. Comp. Phys., **31**, 335-362, 1979.

[77] Zenit R. and Legendre D., The coefficient of restitution for air bubbles colliding against walls in viscous liquids, Phys. Fluid 21, 083306, 2009.

[78] Zobeiri, A., Ausoni, P., Avellan, F. and Farhat, M., How oblique trailing edge of a hydrofoil reduces the vortex-induced vibration, Journal of Fluids and Structures, 32, 78, 2012

Comparisons of numerical and experimental results for rising air bubbles

Aurélia Vallier and Johan Revstedt
Fluid Mechanics/Energy Sciences
Lund University P.O. Box 118, S-221 00 Lund, Sweden

Abstract

Deforming ellipsoidal air bubbles in water are studied numerically using a Volume-Of-Fluid (VOF) method as well as experimentally using a shadowgraph technique. The air volume flow rate and the size of the flow domain are set so that the bubbles are close enough to interact without coalescing. The air bubbles have an equivalent diameter large enough for them to deform without breaking up. The aim of this work is to assess the performance of the numerical solver and also to investigate the bubble behaviour in terms of aspect ratio, rise velocity and bubble path. Two different methods to obtain the centroid position are investigated. The error induced by using data from two-dimensional projections is emphasized by comparing with numerical three-dimensional data.

1   Introduction

The transport of bubbles plays a significant role in many industrial processes such as in chemical, pharmaceutical, environmental and hydro-power applications. Bubbles induce both positive and negative features in industrial processes. A positive feature is that bubbles improve mixing, mass and heat transfer. A negative feature of bubbles is found when cavitation occurs in water turbines in hydro-power plants. Cavitation causes damage on the turbine blade, shroud or hub. Furthermore, it is dependent of many parameters such as water quality, pressure, temperature, turbulence levels and surface roughness. Being able to predict more accurately where bubbles cavitation occurs, increases the performance of water turbines and its efficiency. Hence, modification of the water turbine design allows for the bubble cavitation to occur in regions further away from the turbine. Clearer insight into cavitation is created by a better comprehension of bubble transport and bubble-bubble interaction. Hence, in order to control the performance of bubbly industrial processes which induce both positive and negative effects, a fundamental understanding of the behaviour of individual bubbles in liquid will increase the comprehension of the phenomena mentioned above.

The behaviour of individual air bubbles in water has been studied extensively over the years using mainly experimental techniques. Grace et al. [4] presented a graphical correlation for terminal velocity and shape

of rising bubbles, using experimental results from other researchers. Three distinct bubble shape regions were observed; spherical, ellipsoidal and spherical-cap. Furthermore, Saffman [1] studied the bubble path of a wide range of bubbles. Three characteristic motions were observed, dependent on the diameter D_{eq}: the rectilinear ($D_{eq} < 1.4$ mm), zig-zag ($D_{eq} \in [1.4, 2]$ mm) and helical ($D_{eq} > 2$ mm) motion. Special attention has been paid to the wake of a single rising air bubble. Saffman [1] proposed that the observed zig-zagging bubbles are dependent on its wake. The motion is caused by an interaction between the oscillating wake and a instability in front of the oblate bubble. Lunde and Perkins [5] suggested that a possible reason for shape oscillations is induced by the roughly constant vortex shedding behind the bubble. Brücker [6] used Particle Image Velocimetry (PIV) and de Vries et al. [7] used Schlieren optics technique to observe the wake structure of a single air bubble. The results showed that for zigzagging bubbles the wake structure consisted of a couple of counter-rotating hairpin-like vortices. These vortices are continuously generated and discharged creating a lateral movement. For helical bubbles, the two vortices were twisted and attached at an asymmetrical position, inducing both lateral and circular movement.

Apart from experimental approaches to the study of individual bubbles, numerical two-phase models have been used. The experimental results can be used for validating the two-phase numerical models. The numerical models are less expensive when comparing to experimental equipment and can provide information which is impossible to obtain from experiments, such as three dimensional features. The behaviour of bubbles in the range of $4 < D_{eq} < 20$ mm was observed by Krishna and van Baten [8], using a two-dimensional VOF method. However, their terminal rise velocity did not provide quantitative agreement with experimental results. van Wachem and Schouten [9] utilized a three-dimensional Lagrangian interface VOF approach. Both the rise velocity and shape of the simulated bubbles are in agreement with experimental results. van Sint Annaland et al. [10] compared the bubble shape and terminal rise velocity with the Grace diagram, using a three-dimensional VOF model, achieving good agreement. The presence of the hairpin-type vortex has been observed by Mougin and Magnaudet [11] using a numerical approach.

Deforming ellipsoidal air bubbles in water are investigated in the present work, comparing the VOF implementations in OpenFOAM with available results from experiments. The aim is to assess the accuracy of the numerical solver and also to investigate the bubble behaviour in terms of aspect ratio, rise velocity and bubble path.

2   Problem set-up

The geometrical set-up of the experiments shown in Figure 1 consists of a square channel of dimensions $(x, y, z) = (3D, 3D, 20D)$ where $D = 4$ mm. The channel is filled with distilled water. The free surface is positioned at $z = 17.5D$. At the bottom of the channel pressurized air is injected through a pipe of diameter

D. The bubbles are detached by the so-called pinch-off method where the detachment is occurring naturally due to buoyancy. The air volume flow rate and the size of the flow domain are set so that the bubbles are close enough to interact without coalescing. The air bubbles have an equivalent diameter large enough for them to deform without breaking up. The fluid properties and the governing dimensionless parameters concerning the experiment is given in Table 1. The bubbles were captured using a high-speed CMOS-camera with a 500 mm macro lens obtaining a pixel resolution of 640x580. In each pixel a digital signal was recorded. The temporal and spatial resolution are 500 Hz and 0.119 $mm^2/pixel^2$, respectively. The two-dimensional projections, in xz- and yz-plane, were simultaneously captured using a mirror. The images were recorded using background illumination, implying that bubbles are dark areas of significantly lower signal level than the surrounding fluid. The post-processing of the interface of the projected bubble is done using a contour-detecting algorithm. The error of the contour-detecting algorithm was estimated to less than 1%, using 200 bubbles of various shapes and sizes. The maximum positioning error of the bubble was estimated to be smaller than 1%. Statistics of the experimental data is based on 170 bubbles traveling through the channel.

The limitations of the experimental approach is that only two-dimensional projections can be used in calculating features such as equivalent diameter, aspect ratio, rise velocity and bubble path. However, from the numerical simulations, three-dimensional data are available to calculate these parameters.

Two different geometrical set-up are used for the simulations. One is similar to the experimental set-up. Simulations are also performed with a shorter domain of dimensions $(x, y, z) = (3D, 3D, 9D)$ in order to save computational time. The numerical results obtained with the longer channel are compared with experiments. The error introduced when using a shorter channel is evaluated. In order to model air injected through a circular hole at the centre of the bottom wall of the square channel, a fully developed parabolic laminar velocity profile is set at the inlet

$$U_{inlet} = U_0 \left(1 - \left(\frac{r}{R} \right)^2 \right), \tag{2.1}$$

where the maximum axial velocity, U_0, was chosen to provide a volume flow of $Q = 2 \cdot 10^{-6} m^3/s$ similar to the experimental conditions. An interface is placed at $z = 6D$ for the short channel and at $z = 17.5D$ for the long channel, to resemble the experimental conditions. Neumann boundary conditions are applied for the velocity at the outlet. Additionally, Dirichlet boundary condition of zero pressure is used at the outlet. No-slip boundary conditions are used for the velocity at the side walls and Neumann condition is applied for pressure. For the phase fraction α, Neumann boundary condition accounting for the contact angle with the wall was used.

3 Numerical approach

The governing equations are the incompressible and isothermal conservation of mass (3.2) and momentum (3.3), where ρ, u_i, p, μ, g_i, σ and α are the density, velocity, pressure, dynamic viscosity, gravitation, surface tension and liquid volume fraction. The function $\delta = \frac{\partial \alpha}{\partial x_i}$ ensures that the force is only applied at the interface. The normal direction of the interface, n_i, is given by equation (3.4) and the interface curvature, κ, is given by equation (3.5).

$$\frac{\partial u_i}{\partial x_i} = 0, \tag{3.2}$$

$$\rho(\frac{\partial u_i}{\partial t} + u_j \frac{\partial u_i}{\partial x_j}) = -\frac{\partial p}{\partial x_i} + \frac{\partial}{\partial x_j}(\mu(\frac{\partial u_i}{\partial x_j} + \frac{\partial u_j}{\partial x_i})) + \rho g_i + \sigma \kappa \delta n_i, \tag{3.3}$$

$$n_i = \frac{\frac{\partial \alpha}{\partial x_i}}{|\frac{\partial \alpha}{\partial x_i}|}, \tag{3.4}$$

$$\kappa = \frac{\partial}{\partial x_i} n_i. \tag{3.5}$$

The liquid volume fraction α is propagated using the mass conservative transport equation (3.6).

$$\frac{\partial \alpha}{\partial t} + \frac{\partial u_j \alpha}{\partial x_j} = 0. \tag{3.6}$$

The density and the viscosity are given by

$$\rho = \rho_l \alpha + \rho_g (1 - \alpha), \tag{3.7}$$

$$\mu = \mu_l \alpha + \mu_g (1 - \alpha). \tag{3.8}$$

where the subscripts l and g denote the liquid and gas phases. The advantages of the VOF method is that detailed bubble dynamics are obtained by solving equations (3.2)-(3.6). Both the liquid and the gas phase are obtained with high spatial and temporal resolution. Furthermore, the deformation of the interface, bubble-bubble interaction, bubble break-up and coalescence are included automatically without extra modelling. The drawback with high resolution both in time and space is that the simulations are limited by the computer resources available. Furthermore, difficulties in estimating the interface curvature and obtaining numerical convergence at high density ratio is still an issue. In equation (3.3), the surface tension forces are reformulated into an equivalent volume force $F_i = \sigma \kappa \delta n_i$. This approach may lead to the formation of vortex-like flow in the neighborhood of the interface. These perturbations called spurious currents may cause instabilities and destroy the interface if the surface tension is dominant. In an effort to reduce these effects, different approaches have been introduced such as improving the curvature calculation with a estimator function [16],

4

or height function [17]. Brackbill [13] suggested to add a density scaling factor, $\frac{2\rho}{\rho_l+\rho_g}$, to the force F_i. This approach is applied in section 4.5. The equations (3.2)-(3.3) are discretized in space using second order differencing scheme for all terms except for the convective. For the convective term, a blend of central and upwind difference is applied. The discretization in time is first order Euler scheme. For the pressure-velocity coupling the PISO algorithm is used.

4   Characterization of bubbles deformation

4.1   Three-dimensional features

The aspect ratio E_{3D} of a three-dimensional bubble is a function of the volume V and surface area A of the bubble and it is defined as

$$E_{3D} = \frac{1}{6\sqrt{\pi}}\frac{A^{3/2}}{V},$$
(4.9)

$$V = \int_\Omega (1-\alpha)\,d\Omega,$$
(4.10)

$$A = \int_\Omega \left|\frac{\partial\alpha}{\partial x_i}\right|d\Omega.$$
(4.11)

The choice of the volume of integration Ω is discussed in section 4.5. The bubble's centroid position, C^{3D}, is calculated by integrating around the whole volume Ω. The x-component C_x^{3D} is defined as

$$C_x^{3D} = \frac{\int_\Omega (1-\alpha)\,x d\Omega}{\int_\Omega (1-\alpha)\,d\Omega}.$$
(4.12)

The other components, C_y^{3D} and C_z^{3D}, are calculated in a similar way. The rise velocity is calculated as the ratio between the bubbles propagation in z-direction, $(C_{z,t_2}^{3D} - C_{z,t_1}^{3D})$, and the time difference, $(t_2 - t_1)$, to propagate that distance:

$$U_{rise} = \frac{C_{z,t_2}^{3D} - C_{z,t_1}^{3D}}{t_2 - t_1}.$$
(4.13)

4.2   Two-dimensional projected features

The two-dimensional aspect ratio, can be calculated as

$$E_{2D} = \frac{d_{mi}}{d_{ma}},$$
(4.14)

where d_{ma} is the major axis and d_{mi} is the minor axis. When experimental data are post-processed, the major axis is approximated by using the available extrema of the bubble contour in each plane. For instance, $xmax$ and $xmin$ in yz-plane are illustrated in Figure 2. Thus, the position of a two-dimensional projected

bubble centroid $C_x^{2D,1}$ is obtained as the centre of the approximated major axis

$$C_x^{2D,1} = \frac{xmax - xmin}{2}.$$

(4.15)

The centroid position can also be obtained by integration of α over the projected surface Γ.

$$C_x^{2D,2} = \frac{\int_\Gamma (1-\alpha)x d\Gamma}{\int_\Gamma (1-\alpha) d\Gamma}.$$

(4.16)

As long as the bubble is a rotationally symmetric ellipsoid $C_x^{2D,1}$ and $C_x^{2D,2}$ are equal. However, for a deformed bubble, these definitions give different results since the geometrical centre no longer coincides with the centre of mass.

4.3   Grid dependency

The grid dependency study is performed for the first detached bubble for grid resolution $D/h=8$ (coarse), 16 (medium) and 24 (fine), where h is the cell size. In Figure 3(a), the iso-contours are compared for each grid. On the coarser grids, the VOF method is less sharp than on a fine mesh, therefore the interface is represented by a larger transition region. Figure 3(b) displays the velocity rise. The medium and fine grids produce similar results while there are small discrepancies with the coarse grid: the bubble velocity is almost constant for t $\in [0.11, 0.12]$ s while an acceleration is observed with the two other grids. In Figure 3(c)-(d) the temporal evolution of the bubble volume and aspect ratio show that the results are under-predicted with the coarser grid. For all cases, the bubble volume decreases as the bubble rises. The volume with the coarser mesh is 3.8 to 13.7% smaller than the volume predicted by the finest grid at detachment and at t=0.15 s respectively. The error for the medium grid is in the range 0,7 to 1.7 %. The volume loss is 1.1% (resp. 3.4%) at t=0.15 s for the fine (resp. medium) grid. The aspect ratio obtained with the two finer grids follow the same oscillations even if it grows less with the medium grid than with the finer grid. Based on the fact that the results for $D/h = 16$ and $D/h = 24$ are quite similar, a grid resolution of $D/h = 16$ was used throughout this study in order to save computational time.

4.4   Detachment

Figure 4 illustrates the first bubble detachment and the bubble shape oscillations. The bubble is spherical (a), skirted (b) and then spherical cap (c). Afterwards, the shape oscillates from an ellipsoid with a flatten trailing surface (d) to an ellipsoid with a flatten leading surface (e). Then it becomes an oblate ellipsoid, with a larger aspect ratio (f). The ellipsoid shape is in agreement with the diagram of Grace for the present values of Re and Eo. Figure 5(a) shows that symmetry is observed for the bubble shape and the velocity

vectors, in the case of the first bubble detachment. However the following bubbles in the long channel are asymmetric because they are released in a flow field disturb by the previous bubbles. These perturbations are shown in Figure 5(b).

4.5   Mass conservation

In order to investigate the volume loss observed in Figure 3(c), the method used for evaluating the three dimensional data is discussed. In equation (4.10), the volume fraction α is integrated over a volume Ω that contains the bubble. The size of this volume can have a misleading influence on the post-processed results. For the results presented above, Ω is a box surrounding the bubble. Its size is obtained by adding 1 mm further the extrema of the bubble iso-surface $\alpha = 0.5$, in each direction. The evaluation of the bubble volume is also performed with a larger box Ω, obtained by adding 5 mm further the extrema of the bubble interface. The results are presented in Figure 6 (a). Until $t = 0.095$ s, the results with the larger domain of integration are erroneous because they correspond to the volume of the bubble studied plus the top part of the following bubble. After $t = 0.095$ s, the volume corresponds solely to the bubble studied and it is constant. However, the volume obtained with a narrow box of integration implies that the volume of the bubble is actually decreasing. From these results, it appears that a loss of the bubble volume occurs in the wake of the bubble within a few millimeters. Therefore the effect of the correction for spurious current in the momentum equation (3.3) is investigated. With the density correction in the surface tension force F_i, the volume is lower but constant even whith a volume of integartion close to the bubble interface. It means that the amount of vapor detached from the bubble is strongly reduced with this approach. However this modification influences the shape and the rise velocity of the bubble as shown in Figures 6(b)-(d).

4.6   Sensitivity to the channel length and the number of bubbles

Figure 7 shows the average volume of the bubbles obtained for both channel lengths. With the longer channel, the volume is slightly reduced. Considering the centroid position of the first 10 bubbles in Figure 8(a), there is only a minor difference between the results for different length of the channel. The average bubble path is almost rectilinear in both cases. The bubble to bubble variation (represented by the standard deviation) around this average is increasing with increasing height in the column. The variation is larger for the short channel because the free surface moves and influences the bubble trajectory whereas the free surface is located much higher in the long channel and doesn't influence the bubble path at this height. Statistics with a larger number of bubbles suggest a different behavior for the long channel (Figure 8(b)). A fairly straight mean path is still obtain with 20 bubbles in the short channel while with the long channel, a drift toward the negative x direction is observed. This behavior is caused by the asymmetry of the bubbles

at detachment and the perturbation in the flow field due to previous bubbles wake. These results stress that the closer position of the free surface in the shorter channel has a damping effect on these perturbations. In the long channel, once one bubble has started to drift in a direction it induces a motion in the liquid phase that promotes the tendency for the following bubble to take a similar path. However after a sufficiently long time, the path oscillations are such that the other direction can also become a favorite direction due to the vicinity of the channel walls. Indeed in the long channel, it is observed that the first drift is followed by a drift toward the positive x direction. Furthermore, with 30 bubbles, the first drift is damped and the second one is accentuated (Figure 9).

The aspect ratio shown in Figure 10(a) exhibits a monotonic increase until z=9 mm for both channel lengths. Afterwards, the aspect ratio is constant for the shorter channel while it decreases with the longer channel. In the upper part of the long channel, the aspect ratio oscillates between 1.17 and 1.3 (Figure 10(b)). The amplitude of the oscillations is reduced for a larger number of bubbles.

The discrepancies observed here emphasize the need of using a long channel and a large number of bubbles in order to obtain reasonable statistics.

4.7   Comparisons 2D and 3D results

In Figure 11(a), the bubble path of the bubble centroid positions is shown using the two methods presented in equations (4.15) and (4.16). The bubble centroid position $C_x^{2D,2}$ is smoother as compared to $C_x^{2D,1}$. Indeed with the first method, only the maximum and minimum lateral positions are influencing the centroid position, while for the second method, the whole area of the bubble is accounted. Both centroid methods follow the same path in xz-plane until z=28 mm. However, in the yz-plane (not shown here), there is a difference in the range $z > 16$ mm, which implies that the bubbles are tilted and the error of the experimental method increases. Figure 11(b) shows that $C^{2D,2}$ is in good agreement with C^{3D} in the xz-plane while a loss of accuracy is emphasized in the yz-plane (not shown here) with the 2D approach. These results stress that the bubble shape is not symmetrical and the 2D results are not sufficient to describe the bubbles.

Figure 12 shows the numerical and experimental results for the centroid position $C_x^{2D,1}$. The experiments predict a drift toward the positive direction in each plane with a large bubble to bubble variation. The tendency of the numerical results is similar and a higher number of sample might increase this resemblance. The fluctuations of the experimental results are larger than in the numerical results. A reason is the large number of bubbles passings which induce a stronger motion in the liquid phase and increase the lateral motion of the bubbles

The aspect ratio is displayed in Figure 13. The numerical results show that the difference between

xz- and yz-plane is marginal for 2D aspect ratio, indicating erroneously symmetrical bubbles. These values suggest that the bubbles experience no shape oscillations in the region $10 < z < 15$ mm, and then deforms into ellipsoidal bubbles with an aspect ratio of 0.35. This behaviour is not in agreement with the three dimensional results in Figure 10 which reveal shape oscillations for z>15mm. In both planes, the experimental data show a shape oscillation of the bubble after detachment and up to z=14 mm (resp. 17 mm) and thereafter a continuous increase of the aspect ratio. These discrepancies are attributed to the errors induced by the approach used for evaluating the 2D aspect ratio which is not representative in the case of deformed bubbles.

5   Conclusions

The present work illustrated the limitations of the volume of fluid method implemented in OpenFOAM which predicted an unphysical volume loss in the wake of the bubbles. The volume loss is decreased when using a finer mesh. The modification of the surface tension force also reduces the volume loss in the wake. However, it affects the shape and the velocity of the bubbles. The first bubble rises faster and undergoes stronger shape oscillations, when this modification is included.

This study showed that the choice of a short channel was valid only for the first 10 bubbles. For the following bubbles, the presence of a closer free surface affects the results. The perturbations of the flow and the detachment are no longer similar and influence the trajectory and the shape of the bubbles.

Furthermore, comparisons between 2D and 3D evaluation of the results were performed. The 2D method to estimate the aspect ratio inherently will predict symmetrical bubbles with a ellipsoidal shape. However, using the 3D method the results clearly showed shape oscillations. These discrepancies indicate that the method used in the experiments is limited to bubbles which are not tilted or deformed from the ellipsoid shape.

Acknowledgements

References

[1] Saffman P., On the rise of small air bubbles in water, J. Fluids Mech., 249-275, 1956.

[2] Aybers, N.M. and Tapucu, A., Studies of the drag and shape of gas bubbles rising through a stagnant liquid, Wrme- und Stoffubertragung 2, pp. 171-177, 1969

[3] Aybers, N.M. and Tapucu, A., The motion of gas bubbles rising through stagnant liquid, Wrme- und Stoffubertragung, pp. 118-128, 1969

[4] Grace, J.R., Wairegi, T. and Nguyen, T.H, Shapes and velocities of single drops and bubbles moving freely through immiscible liquids, Trans. Inst. Chem. Eng., vol. 54, pp. 167-173, 1976.

[5] Lunde, K. and Perkins, R.J, Shape oscillations of rising bubbles, Applied Scientific Research, vol. 58, pp. 387-408, 1998.

[6] Brücker C., Structure and dynamics of the wake of bubbles and its relevance for bubble interaction, Phys. Fluids 11, 1781-1796, 1999.

[7] de Vries A., Biesheuvel A., van Wijngaarden L., Notes on the path and wake of a gas bubble rising in pure water, Int. J. Multiphase Flow 28, 1823-1835, 2002.

[8] Krishna, R. and van Baten, J.M., Rise characteristics of gas bubbles in a 2D rectangular column: VOF simulations vs. experiments., Int. Comm. Heat Mass Transfer, vol. 26, pp. 965-974,1999.

[9] van Wachem, B.G.M and Schouten, J.C., Experimental validation of 3-D Lagrangian VOF model: Bubble shape and rise velocity, AIChE Journal, vol. 48, pp. 2744-2753, 2002

[10] van Sint Annaland, M., Deen, N.G. and Kuipers, J.A.M., Numerical simulation of gas bubbles behaviour using a three-dimensional volume of fluid method, Chem. Eng. Sci., vol. 60, pp. 2999-3011, 2005.

[11] Mougin G., Magnaudet J., Path instability of a rising bubble. Physical review letters 88, 2002.

[12] Hirt, C.W. and Nichols, B.D., Volume of Fluid (VOF) Method for the Dynamics of Free Boundaries, J. Comp. Phys., Vol. 39, pp. 201-225, 1981.

[13] Brackbill J.U., Kothe D.B., Zemach C., A continuum Method for Modeling surface Tension, J. Comp. Phys., 100, 335-354, 1992.

[14] Rusche H., Computational fluid dynamics of diversed two phase flows at high phase fraction. PhD thesis, University of London , England, 2002.

[15] Arlov D., Numerical study of flows related to aerated stirred tanks, PhD, Lund, 2007.

[16] Meier, Numerical and experimental study of large steam-air bubbles injected in a water pool, PhD, Swiss Federal Institute of Technology, Zürich, Switzerland, 1999.

[17] Popinet S., An accurate adaptative solver for surface tension driven interfacial flows, J. Comp. Phys., 228 5838-5866, 2009.

List of Figures

Figure 1: The experimental set-up of the column. D=4 mm

Figure 2: A schematic contour of a bubble interface. The projection is in xz-plane. (a) Definitions of major and minor axes and bubble centroid position in the case of an ellipsoid. (b) Error between the definition and the method used for the calculation of the axes in the case of a tilted ellipsoid. (c) Error between the definition and the method used for the calculation of the axes in the case of a deformed ellipsoid.
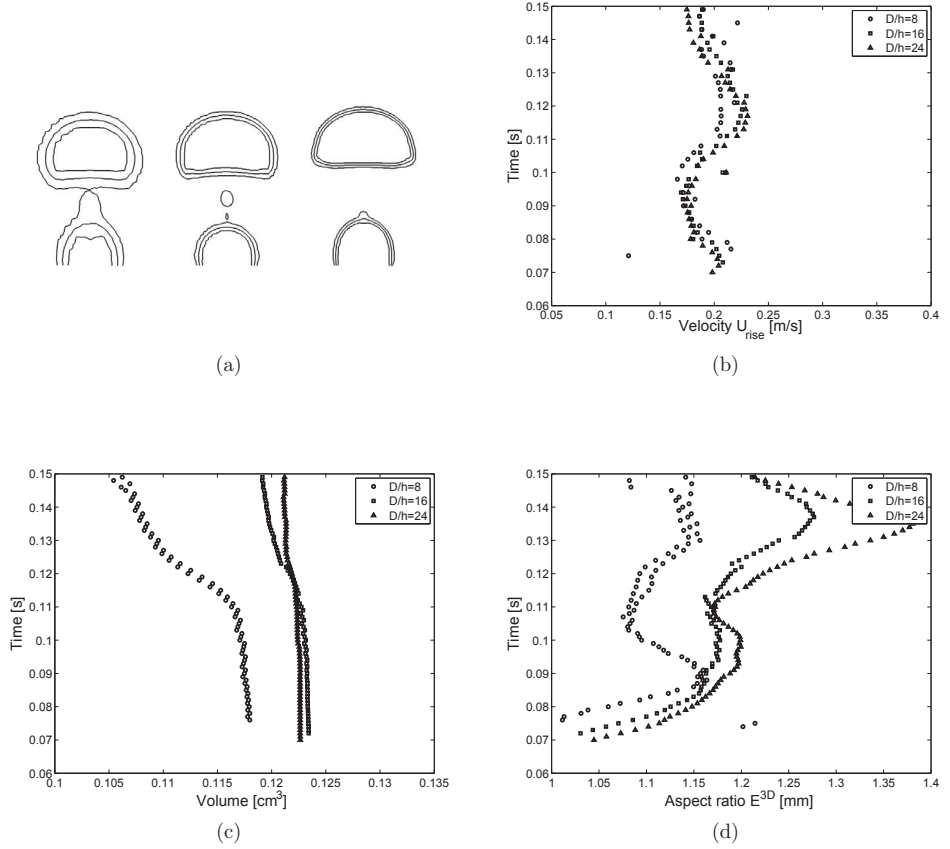
Figure 3: (a) Isosurfaces ($\alpha = 0.1$, 0.5 and 0.9) for the first bubble for different grid resolutions, t=0.08 s. (b) Rise velocity, (c) volume and (d) aspect ratio of the first bubble for different grid resolutions.

(a) t=0.071 s   (b) t=0.074 s   (c) t=0.08 s

(d) t=0.092 s   (e) t=0.1 s   (f) t=0.137 s
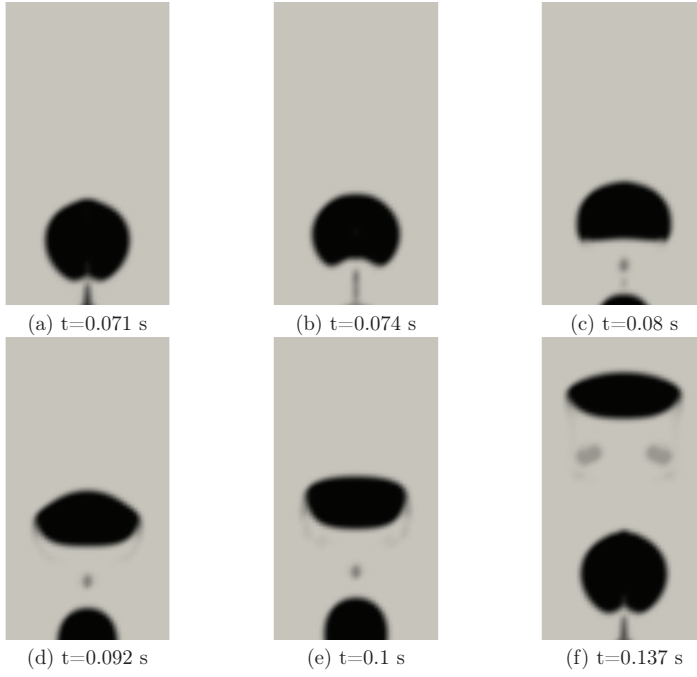
Figure 4: First bubble detachment and shape oscillations.

(a)   (b)
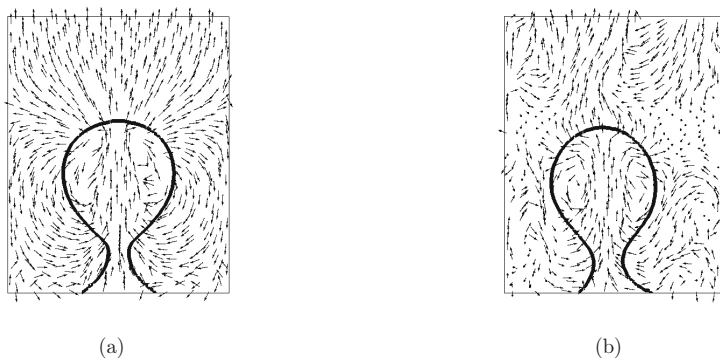
Figure 5: The bubble shape and the velocity vectors at detachment, (a) t=0.069 s, (b) t=1.401 s.
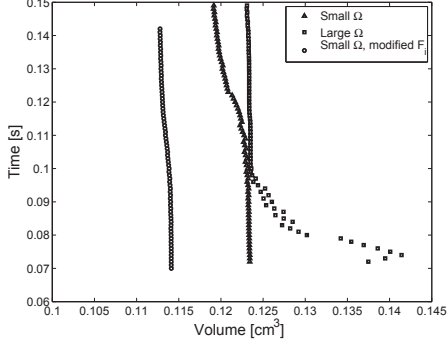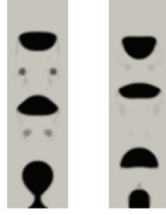
(a)   (b)
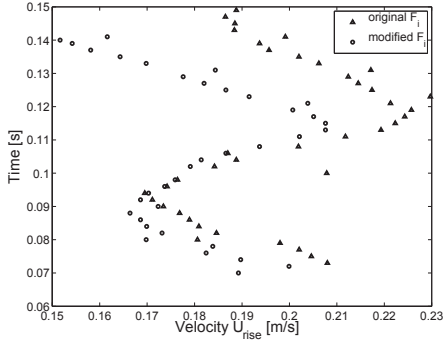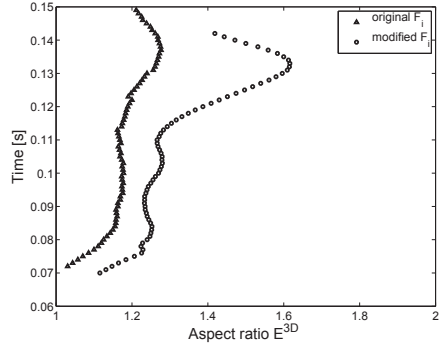
(c)   (d)

Figure 6: (a) Volume of the first bubble with different sizes for the volume of integration Ω and with the density correction for the surface tension force in equation (3.3). (b) Shape of the first bubbles when the surface tension force in equation (3.3) is without (left) and with (right) density correction. (c) Velocity rise and (d) aspect ratio of the first bubble when the surface tension force in equation (3.3) is with or without density correction.
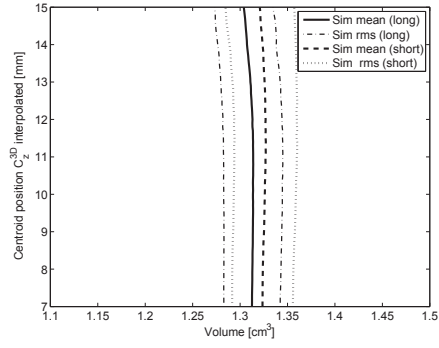
Figure 7: Volume from 3D calculations with 20 bubbles and different channel lengths.
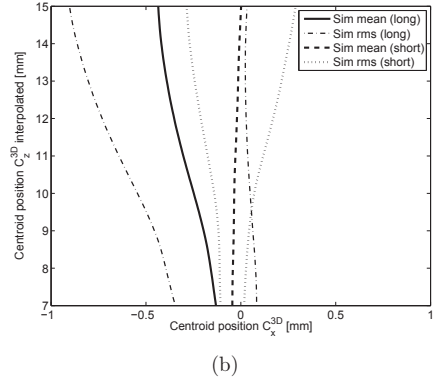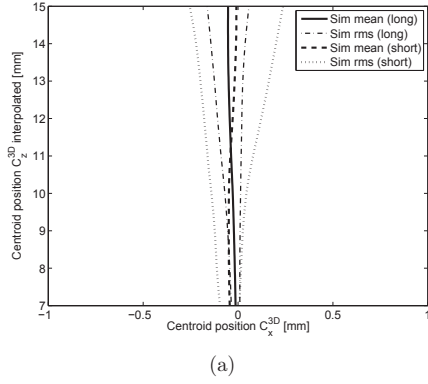
Figure 8: The bubble path in xz-plane from 3D calculations for (a) 10 and (b) 20 bubbles (short and long channel).
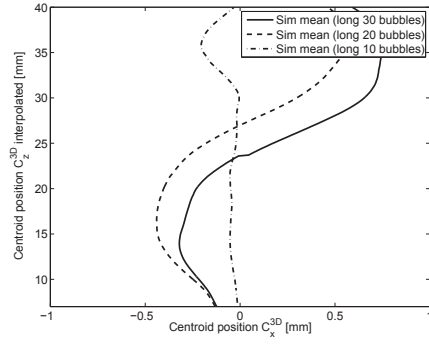
Figure 9: The bubble path in xz-plane from 3D calculations for 10, 20 or 30 bubbles (long channel)
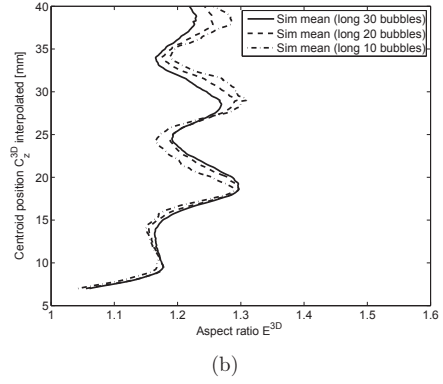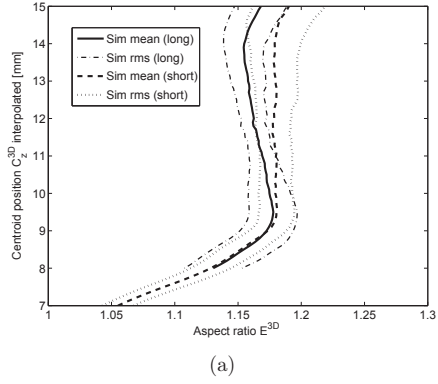
Figure 10: (a) The aspect ratio evaluated from 3D calculations for 20 bubbles (short and long channel). (b) The aspect ratio evaluated from 3D calculations (long channel)
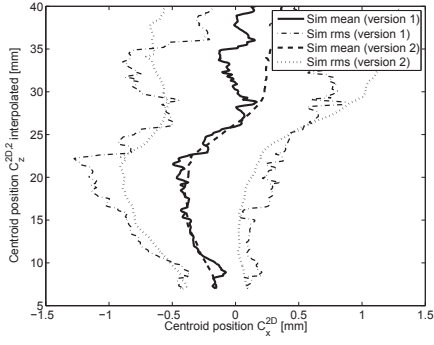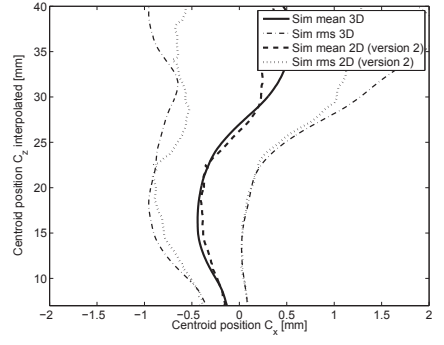
Figure 11: (a)The bubble path in the xz-plane with two methods for calculating the centroid. (b) The bubble path in the xz-plane from 2D and 3D calculations.
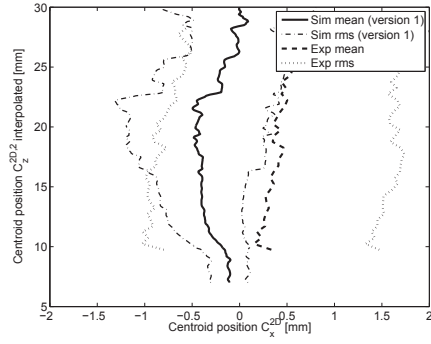
Figure 12: The bubble path in the xz-plane from 2D calculations and experiments.

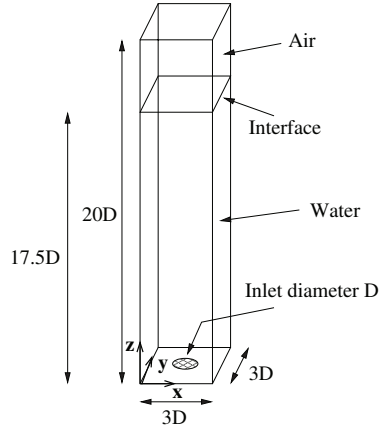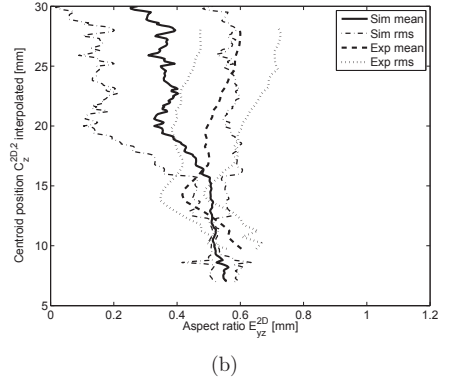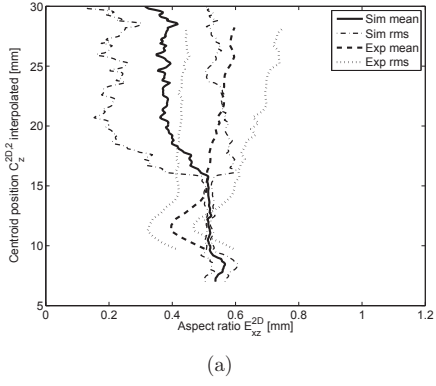**Figure 13:** The aspect ratio for (a) xz-plane and (b) yz-plane from 2D calculations and experiments.

List of Tables

Property	Nomenclature	Air	Water
Temperature	T [° C]	20 ± 0.5	20 ± 0.5
Density	$\rho_{l,g}$ $[kg/m^3]$	1.20 ± 0.00	998 ± 0.10
Dynamic viscosity	$\mu_{l,g}$ $[kg/(ms)]$	$1.81 \pm 0.00 \cdot 10^{-5}$	$1.00 \pm 0.01 \cdot 10^{-3}$
Surface tension	σ_{st} $[N/m]$		0.0728
Volume flow	Q $[m^3/s]$		$2.0 \pm 0.5 \cdot 10^{-6}$
Reynolds number	$Re = \frac{\rho_l V_{bubble} D_{eq}}{\mu_l}$ $[-]$		$400 < Re < 2200$
Eötvos number	$Eo = \frac{g(\rho_l - \rho_g) D_{eq}^2}{\sigma_{st}}$ $[-]$		$4.4 < Eo < 7.6$
Morton number	$Mo = \frac{g(\rho_l - \rho_g) \mu_l^4}{\rho_l^2 \sigma_{st}^3}$ $[-]$		$2.5 \cdot 10^{-11}$

Table 1: The physical properties and governing dimensionless parameters from the experimental set-up. Subscripts l and g denotes liquid and gas, respectively.

Modelling of bubble dynamics related to cavitation

A. Vallier[*,a], J. Revstedt[a], H. Nilsson[b]

[a]*Division of Fluid Mechanics Dept. Energy Sciences, Lund University,*
SE-22100 Lund, Sweden
[b]*Applied Mechanics, Fluid Dynamics, Chalmers University of Technology,*
SE-412 96 Gothenburg, Sweden

Abstract

The dynamics of small bubbles is simulated in order to predict the risk of cavitation erosion. A Rayleigh-Plesset bubble dynamics model is implemented and validated against several test cases. The sensitivity of the model parameters on the results is emphasized. For each bubble, a proper equilibrium radius is calculated in order to avoid unphysical oscillations at the beginning of the computations. The variations of different kinds of energy during a collapse is studied in order to estimate the intensity of the collapse. The results are used for evaluating the total energy loss and the energy dissipated in the shock wave. The accuracy of these approaches is discussed.

The bubble dynamics model is applied to travelling bubbles collapsing above a rectangular cylinder, using a discrete bubble transport model and a random-walk dispersion model. The forces affecting the bubbles are described. The contribution of the volume variation force is clarified. The present work emphasizes the influence of the ambient pressure, the initial size of the bubbles, their release position, as well as the flow features. The results provide information about the regions that are most subjected to successive collapses as well as the collapse intensities.

Key words: Bubble dynamics, Rayleigh-Plesset equation, Discrete Bubble Model, cavitation.

---

[*]Corresponding author
Email addresses: `aurelia.vallier@energy.lth.se` (A. Vallier),
`johan.revstedt@energy.lth.se` (J. Revstedt), `hani@chalmers.se` (H. Nilsson)

1. Introduction

Cavitation is the formation of vapor cavities in an initially homogeneous liquid. The cavities range from large coherent irregular structures, to clouds of tiny spherical bubbles. The large-scale cavity structures cause a modification of the flow path, which affects the efficiency of hydraulic machinery. They may also cause vibrations due to cavity instabilities, similar to vortex shedding. Large-scale cavitation inception and break-up are strongly related to the range of smaller structures and the tiny spherical bubbles. The tiny spherical bubbles act as disturbances in the homogeneity of the liquid and act as sources for the generation of larger structures in regions where the static pressure is reduced. As the large-scale structures break up, clouds of bubbles of different scales are generated. Travelling to regions of higher static pressure, the bubbles implode, causing noise and a risk of material erosion. Small gas bubbles play therefore an important role, both in cavitation inception and in the erosion process. A better understanding of the bubble dynamics is thus essential to control where cavitation inception and damages occur. To minimize cavitation damages it is important to reduce the energy of the bubble collapses, or to make sure that the collapses occur far away from the surfaces.

The presence of gas bubbles is a primordial factor to initiate cavitation. These small bubbles may follow the flow or can be trapped in surface rugosities, and they grow when the surrounding pressure is reduced. Depending on the bubble properties and the pressure applied on them, they may stay in equilibrium, collapse, or grow into macroscopic bubbles. Studies in the context of cavitation erosion focus on the bubble collapses and their damaging effects. Rayleigh (1917) originally explained that a single collapsing spherical bubble emits a large pressure peak which can be directly responsible for surface damages. The shock wave radiated in the liquid may also influence the collapse of the surrounding bubbles and cause a focus of energy. Thus, erosion is in reality a result of a complex interaction within a cloud of bubbles. The shock waves emitted by collapsing bubbles affect bubbles close to walls which, in turn, collapse and damage the surface (see e.g. Mettin et al. (1997)). Near a solid boundary, a bubble is deformed and the acoustic wave emitted by the collapse of an asymmetrical bubble is weaker than the one issued from an unbounded collapse (see e.g. Vogel and Lauterborn (1988)). The erosion process is therefore explained by the co-existence of a shock wave and a strong liquid jet which penetrates through the bubble and impacts the

wall upon collapse in the vicinity of the surface boundary (see e.g. Blake and Gibson (1987), Brujan et al. (2005) and Popinet and Zaleski (2002)). The damaging effect of the liquid jet is related to the tremendous velocity and temperature involved. The predominance of the contribution of the shock wave or the liquid jet on surface damages depends on the shape of the bubble and its distance from the surface (see e.g. Philipp and Lauterborn (1998) and Shima (1997)). These theories still don't fully explain the mechanism of erosion because of the diversity of factors that influence the way bubbles approach the solid surface and the way they collapse (see e.g. Benjamin and Ellis (1996)). Nevertheless, the intensity and the location of the collapses are crucial parameters to predict the risk of erosion on the surfaces.

While the bubble growth and collapses are difficult to measure experimentally, due to the small time scales involved, they can be estimated from numerical simulations with appropriate models. In order to get a better insight on the bubble dynamics and its effects, a numerical model is implemented and the sensitivity of different parameters on the results is emphasized. In the present work, the Rayleigh-Plesset model for the dynamics of spherical bubbles is implemented and validated for several cases of collapsing bubbles. The results are compared with previous numerical and empirical studies. A method for estimating the equilibrium radius at the release location is derived and validated in order to avoid bubble size oscillations at the beginning of the computations. The variations of different kinds of energy during a collapse is studied in order to estimate the intensity of the collapse. The results are used for evaluating the total energy loss and the energy dissipated in the shock wave. The accuracy of these approaches is discussed. Once the accuracy of the bubble dynamics model is assessed, it is included in a discrete bubble tracking algorithm. The forces affecting the bubble are described. A study is performed to clarify the contribution of the force introduced by Johnson and Hsieh (1966) which accounts for the volume variation of the bubbles. A model for turbulence dispersion is implemented to describe the deviation of the bubble trajectory from the streamlines of the mean flow. The algorithm is applied to small bubbles travelling and collapsing around a rectangular cylinder. The intensity and location of the collapses are investigated in order to emphasize the influence of the ambient pressure, the size of the bubbles, their release position, as well as the flow features.

2. Bubble dynamics and initial equilibrium radius

A small cavitation bubble is here approximated as a spherical bubble with a radius $R(t)$ and a rate of growth $\dot{R} = \frac{dR(t)}{dt}$. The acceleration of the bubble surface is given by $\ddot{R} = \frac{d^2 R(t)}{dt^2}$. The bubble density, ρ_B, and internal pressure, $p_B(t)$, are assumed to be uniform. The surrounding liquid has a density ρ_L and a pressure $p_L(\mathbf{x}_B, t)$ at the bubble location $\mathbf{x}_B$. The surrounding liquid pressure is the sum of a constant reference pressure p_0 and a time varying pressure $p(t)$. The bubble is assumed to be in equilibrium at liquid pressure p_0, with radius R_0 and $\dot{R} = \ddot{R} = 0$. Any variation of the liquid pressure, $p(t)$, acts as a disturbance on the bubble stability and influences the radius of the bubble, $R(t)$.

The bubble contains water vapour and a non-condensable gas of which the mass is assumed constant during the evolution of the bubble size. The presence of the gas ensures that a collapsing bubble cannot disappear, i.e. $R(t) > 0$. The collapse phase ends when the compression stops and it is followed by a rebound of the bubble. In order to express the radius and the rate of growth as a function of time, Rayleigh (1917) and Plesset and Prosperetti (1977) derived the equations of the bubble dynamics under the assumptions that the bubble stays spherical and that the liquid is incompressible. When the surface tension σ_{st} and the liquid viscosity μ_L are accounted for, the Rayleigh-Plesset equation is given by

$$R\ddot{R} + \frac{3}{2}\dot{R}^2 = \frac{1}{\rho_L}\left[p_B(t) - 4\mu_L\frac{\dot{R}}{R} - \frac{2\sigma_{st}}{R} - p_L(\mathbf{x}_B, t) \right], \qquad (1)$$

where the pressure inside the bubble, $p_B(t)$, is the sum of the saturated vapour pressure p_v and the gas pressure $p_g(t)$. The gas pressure is related to the equilibrium state gas pressure p_{g0}, at (R_0, p_0), as $p_g(t) = p_{g0}\left(\frac{R_0}{R(t)}\right)^{3\gamma}$. Moss et al. (2000) suggested to use different values for the polytropic coefficient γ during the process of growth and collapse. The bubble growth phase preceding a collapse is sufficiently slow to be assumed isothermal and during this process, when $R \geq R_0$, γ is unity. On the other hand, the collapse occurs within an extremely short time, therefore the compression of gas is assumed adiabatic during this phase and γ takes the value of the ratio of the heat capacities of the gas, $\gamma = 1.4$, when $R < R_0$. Equation (1) at the equilibrium

state, (R_0, p_0), gives the gas pressure p_{g0} as

$$p_{g0} = p_0 + \frac{2\sigma_{st}}{R_0} - p_v. \tag{2}$$

If the bubble reaches a new equilibrium state at $t = t_e$, the radius is denoted $R(t_e) = R_e$ and the equilibrium condition implies $\dot{R}(t_e) = \ddot{R}(t_e) = 0$. Thus, equation (1) reduces to

$$0 = \left(p_0 + \frac{2\sigma_{st}}{R_0} - p_v \right) \left(\frac{R_0}{R_e} \right)^{3\gamma} + p_v - \frac{2\sigma_{st}}{R_e} - p_L(\mathbf{x}_B, t_e). \tag{3}$$

The equilibrium relation between the liquid pressure and the equilibrium radius R_e is thus given by

$$p_L(\mathbf{x}_B, t_e) = p_{g0} R_0^{3\gamma} R_e^{-3\gamma} - 2\sigma_{st} R_e^{-1} + p_v. \tag{4}$$

The minimum of the equilibrium relation (4) is the critical equilibrium pressure, p_c, reached at $R_e = R_c$, which has the analytical expression

$$R_c = R_0 \left(\frac{3\gamma p_{g0} R_0}{2\sigma_{st}} \right)^{\frac{1}{3\gamma-1}},$$
$$p_c = p_v - \frac{2\sigma_{st}}{R_c} \left(\frac{3\gamma-1}{3\gamma} \right).$$

The critical pressure is less than the vapor pressure and the difference $p_v - p_c$ is larger for smaller bubbles. The critical pressure becomes negative when the bubble size is sufficiently small. Following the explanations of Franc (2006), a bubble initially at equilibrium which is subjected to a small reduction of the liquid pressure will converge to a new equilibrium state provided that $p_L(\mathbf{x}_B, t_e) > p_c$. When $p_L(\mathbf{x}_B, t_e) > p_v$, there exists a single equilibrium radius which is stable. If $p_c < p_L(\mathbf{x}_B, t_e) < p_v$, the equilibrium is either stable (for $R_e < R_c$) or unstable (for $R_e > R_c$). It is known (see e.g. Chahine and Shen (1986)) that for $p_L(\mathbf{x}_B, t_e) < p_c$, or for an unstable equilibrium, a decrease of the pressure leads to a growth without limit. In this case, the growth rate increases until an asymptotic value $\dot{R}_{lim}$. Franc (2006) derived an approximation of $\dot{R}_{lim}$ by integrating equation (1) using the assumptions of constant liquid pressure $p_L(\mathbf{x}_B, t_e) < p_v$, $R \to \infty$ and that the viscous effect and surface tension are negligible for large bubbles, yielding

$$\dot{R}_{lim} \sim \sqrt{\frac{2}{3} \frac{p_v - p_L(\mathbf{x}_B, t)}{\rho_L}}. \tag{5}$$

5

In practice, the known parameters in equation (1) are the initial radius, the initial pressure and the reference pressure. It is important to make sure that the bubble is initially in equilibrium in order to avoid unphysical oscillations at the beginning of the computation. If $t = t_e$ at the instant the computation starts, the initial radius is $R(t_e) = R_e$ and the liquid pressure $p_L(\mathbf{x}_B, t_e)$. If the initial pressure is the reference liquid pressure, $p_L(\mathbf{x}_B, t_e) = p_0$, the choice $R_0 = R_e$ yields a bubble in equilibrium. However, if the initial pressure differs from p_0, i.e. $p_L(\mathbf{x}_B, t_e) = p_0 + p(t_e)$, it is necessary to determine the equilibrium radius R_0 corresponding to the reference liquid pressure p_0 on the equilibrium curve of $(R_e, p_L(\mathbf{x}_B, t_e))$. After re-arranging terms in equation (3), it is deduced that the equilibrium radius R_0 satisfies the condition

$$R_0^{3\gamma} + aR_0^{3\gamma-1} + b = 0, \tag{6}$$

with

$$\begin{cases} a = \frac{2\sigma_{st}}{p_0 - p_v}, \\ b = \frac{R_e^{3\gamma}}{p_0 - p_v} \left(p_v - \frac{2\sigma_{st}}{R_e} - p_L(\mathbf{x}_B, t_e) \right). \end{cases}$$

If this proper value is not chosen for R_0, the bubble oscillates around the equilibrium and the frequency of oscillation, f_0, is estimated by Franc (2006) by linearizing equation (1) and neglecting the liquid viscosity. The bubble resonance frequency is given by

$$f_0 = \frac{1}{2\pi R_0} \sqrt{\frac{1}{\rho} \left(3\gamma p_{g0} - \frac{2\sigma_{st}}{R_0} \right)}. \tag{7}$$

2.1. Energy dissipation and shock wave energy

Cavitation damage is assumed to be proportional to the energy acting on the surface. Therefore the energies involved in the collapse are considered here. The total bubble energy is the sum of the potential, kinetic and internal energy, $E_B = E_{pot} + E_{kin} + U$. According to Best (2002), the kinetic energy is

$$E_{kin} = 2\pi \rho_L \dot{R}^2 R^3. \tag{8}$$

The potential energy is the work done in expanding from zero radius to radius R against the hydrostatic pressure, i.e.

$$E_{pot} = \int_0^R 4\pi r^2 \Delta p \, dr = \frac{4}{3}\pi \Delta p R^3. \tag{9}$$

6

The pressure Δp is the difference between the static liquid pressure and the pressure of the condensable vapor inside the bubble, i.e $\Delta p = p_0 - p_v$. The internal energy is the work done in compressing adiabatically the gas from zero pressure (i.e. infinite volume) to the volume of the bubble V_B,

$$U = -\int_{\infty}^{V_B} p \, dV = \frac{4\pi}{3(\gamma - 1)} p_g R^3.$$ (10)

It is several orders of magnitude smaller that the other energies and is therefore neglected. During the collapse, a portion of the bubble energy is dissipated by various effects such as thermal radiation, production of the pressure wave, and surface deformation. When the bubble reaches the maximum size $R(t_1) = R_{max}$ before the collapse, $\dot{R}(t_1) = 0$ and the kinetic energy is canceled. This is also true after the collapse, when the rebound bubble reaches the maximum size $R(t_2) = R_{reb}$. The energy dissipated during the collapse is therefore estimated as

$$E_{diss} = E_B(t_1) - E_B(t_2) = \frac{4}{3}\pi \Delta p (R_{max}^3 - R_{reb}^3).$$ (11)

The energy of a spherical shock wave produced by a bubble collapse is estimated by Cole (1948) as

$$E_{SW} = \frac{4\pi r^2}{\rho_L c_L} \int_{t_1}^{t_2} p_a(r)^2 dt,$$ (12)

where $r \geq R$ is the distance from the center of the bubble, c_L is the sound speed in the liquid and p_a is the pressure of the acoustic wave radiated by the bubble collapse which is estimated by Mettin et al. (1997) as

$$p_a(r) = \frac{\rho_L}{r}(R^2 \ddot{R} + 2R\dot{R}^2).$$ (13)

Combining equations (1), (12) and (13) gives

$$E_{SW} = \frac{4\pi}{\rho_L c_L} \int_{t_1}^{t_2} \left(\frac{\rho_L}{2} R\dot{R}^2 + (p_B - p_L)R - 4\mu_L \dot{R} - 2\sigma_{st}\right)^2 dt.$$ (14)

2.2. Numerical solution and initial condition

The Rayleigh-Plesset equation (1) is a non-linear 2nd order ODE which is considered stiff due to the significant variation of its coefficients with time.

If the bubble undergoes a collapse, its growth rate $\dot{R}$ becomes highly non-linear and its radius R can rapidly decrease several orders of magnitude. As the collapse occurs on a much shorter timescale than the growth phase, it is necessary to use a solver which adapts the step size to the variation of the coefficients. Equation (1) can be written as two first-order ODEs, yielding

$$\begin{cases} \frac{dR}{dt} = \dot{R}, \\ \frac{d\dot{R}}{dt} = -\frac{3}{2}\frac{\dot{R}^2}{R} + \frac{p_B - p_L}{\rho_L}\frac{1}{R} - 4\nu_L\frac{\dot{R}}{R^2} - \frac{2\sigma_{st}}{\rho_L}\frac{1}{R^2}. \end{cases}$$

In matrix form, it reads $[X]' = [F]$, where the matrices are

$$X = \begin{bmatrix} R \\ \dot{R} \end{bmatrix} \;,\quad F = \begin{bmatrix} \dot{R} \\ -\frac{3}{2}\frac{\dot{R}^2}{R} + \frac{p_B - p_L}{\rho_L}\frac{1}{R} - 4\nu_L\frac{\dot{R}}{R^2} - \frac{2\sigma_{st}}{\rho_L}\frac{1}{R^2} \end{bmatrix}.$$

Within each time step, the system of ODEs can be integrated with a Runge-Kutta method and different strategies are suggested for time step optimization (see e.g. Alehossein and Qin (2007) and Shams and Apte (2009)). However, the method can be inherently optimized with an automatic step size adjustment provided by a so-called embedded method. Given an initial estimated time step h_{RK}, it consists in computing two estimates of the unknown, the real one $[X]$ and a low order estimate $[\hat{X}]$. The truncation error $err = [X] - [\hat{X}]$ is used to control the step size according to an user-defined error criteria ϵ_{RK}.

In the present work, the time integration method used is the embedded Rosenbrock method presented by Kaps and Rentrop (1979) with the set of parameters proposed by Shampine Shampine (1982). It seeks a solution of the form $[X(t_0 + h_{RK})] = [X_0] + \sum_{i=1}^{s} c_i\mathbf{k}_i$, and c_i are replaced by $\hat{c}_i$ to evaluate $[\hat{X}]$. The coefficients c_i and $\hat{c}_i$ are fixed constants. The corrections $\mathbf{k}_i$ are found by solving s linear equations which require the Jacobian matrix, as shown by Press et al. (1992). The coefficients of the Jacobian matrix are obtained by the analytical differentiation of the right hand side of the system of ODEs, yielding

$$[J] = \frac{\partial[F]}{\partial[X]} = \begin{bmatrix} 0 & 1 \\ \frac{3\dot{R}^2}{2R^2} - \frac{p_B - p_L}{\rho_L R^2} + \frac{8\nu_L\dot{R}}{R^3} + \frac{4\sigma_{st}}{\rho_L R^3} & -\frac{3\dot{R}}{R} - \frac{4\nu_L}{R^2} \end{bmatrix}.$$

The step size control is based on the following criterion,

- if $err \leq \epsilon_{RK}$, the next time step is evaluated as

$$min(0.9h_{RK}err^{-1/4}, 1.5h_{RK}),$$

- if $err > \epsilon_{RK}$, the time step is reduced to

$$max(0.9h_{RK}err^{-1/3}, 0.5h_{RK}).$$

Using $s = 4$ for calculating $[X]$ and $s = 3$ for calculating $[\hat{X}]$ leads to a fourth order accurate method. The initial estimated time step h_{RK} is set to 10^{-10}s for all the calculations in this work since the collapse is not resolved for higher values of h_{RK}. The error criteria is set to 10^{-4} as it was found that the accuracy was not improved for smaller values.

The equilibrium radius R_0 is calculated by solving equation (6) with the leap-frog Newton's method, presented by Kasturiarachi (2002). The equation is written as $f(x) = 0$ where the function f and its derivative f' are defined as

$$f(x) = x^{3\gamma} + ax^{3\gamma-1} + b,$$
$$f'(x) = 3\gamma x^{3\gamma-1} + a(3\gamma - 1)x^{3\gamma-2}.$$

The initial guess is the initial radius in equilibrium at pressure $p_L(\mathbf{x}_B, t_e)$, given by $x_0 = R_e$. The iteration formula is

$$x_{n+1} = x_n - \frac{f(x_n)^2}{f'(x_n)\left(f(x_n) - f(\overline{x}_n)\right)},$$

where

$$\overline{x}_n = x_n - \frac{f(x_n)}{f'(x_n)}.$$

3. Validation

The implementation of the Rayleigh-Plesset model is validated for the critical equilibrium state, the initial equilibrium radius, the energy dissipation and the radius evolution.

3.1. The critical equilibrium state

In section 2, the conditions for infinite growth were presented. It occurs for $p_L(\mathbf{x}_B, t) < p_c$ or $R \geq R_{e,u}$. These two theoretical cases are illustrated in the case of a bubble which has the equilibrium state $R_0 = 1$ μm, $p_0 = 100$ kPa.
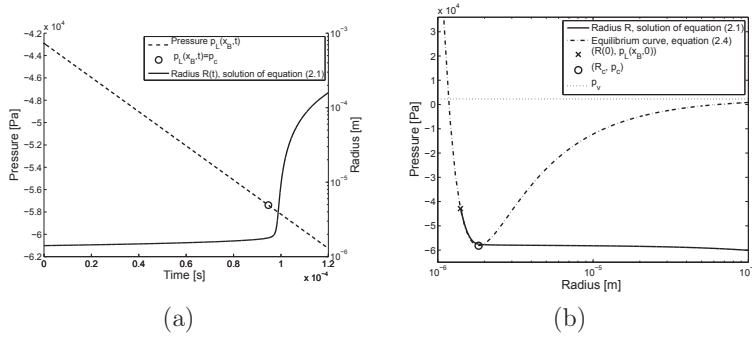
Figure 1: The bubble initial equilibrium state is (R(0)=1.4 μm, $p_L(\mathbf{x}_B, 0) = -42.9$ kPa).(a) The temporal evolution of the liquid pressure (dashed line) and the resulting bubble radius calculated with equation (1) (solid line). (b) The same temporal evolution of the bubble size (solid line) on the equilibrium curve (dashed-dotted line). The radius calculated with equation (1) follows the equilibrium curve when $p_L(\mathbf{x}_B, t) < p_c$. Once the pressure is below the critical value p_c, the radius grows indefinitely.

3.1.1. Response to a pressure drop

First, the response to a pressure drop is investigated. The bubble radius is initially R(0)=1.4 μm. According to the equilibrium relation (4) the bubble is equilibrated at liquid pressure $p_L(\mathbf{x}_B, 0) = -42.9$ kPa. The Rayleigh-Plesset equation is solved for a liquid pressure $p_L(\mathbf{x}_B, t)$ decreasing linearly. Figure 1(a) shows the slow growth of the radius when the pressure decreases until it reaches the critical value p_c. After this time, an equilibrium cannot be reached anymore when the pressure is decreased below p_c and the bubble size grows two orders of magnitude within 20 μs. In Figure 1(b) the bubble size evolution is shown on the equilibrium curve. It illustrates that there is no radius on the curve which corresponds to this pressure and ensures a state of equilibrium. Therefore, the infinite growth is observed from the threshold value $p_L(\mathbf{x}_B, t) < p_c$.

3.1.2. Sensitivity to the initial size

The pressure is kept constant $p_L(\mathbf{x}_B, t) = p_L(\mathbf{x}_B, 0) = -42.9$ kPa. The initial radius R(0) is set to a value lower than the equilibrated radius $R_e = 1.4$ μm at this pressure. The simulations are performed for different values of the initial radius (from R(0)= $0.55R_e$ to R(0)= $0.9R_e$). The initial values are shown in Figure 2(a) together with the equilibrium curve for $(R_e, p_L(\mathbf{x}_B, 0))$. Figure 2(b) shows the radius as a function of time. In the case of a bubble with a radius close to the stable equilibrium radius, the size oscillates and converges to the stable equilibrium radius. The amplitude and the period of the oscillations are larger for the smaller radius ratio $R(0)/R_e$. For the case $R(0) = 0.55R_e$ the radius increases enough to reach the value of the unstable equilibrium radius $R_{e,u} = 3.0687$ μm. Afterwards the radius grows unbounded as predicted. In order to explain this behavior, the growth rate is shown in Figure 2(c) for the cases $R(0) = 0.6R_e$ and $R(0) = 0.55R_e$. At the beginning of the computations, the growth rate increases in order to set the bubble in equilibrium R_e. Once the value R_e is reached, the growth rate starts to decrease. It implies that the radius continues to grow, but more slowly. In the case of $R(0) = 0.6R_e$, the growth rate becomes negative which yields the decreasing of the radius. Then the radius reaches again the value R_e which implies that the growth rate starts to increase and that the radius shrinks more slowly. In the case $R(0) = 0.55R_e$, the radius reaches the unstable radius value $R_{e,u}$ while the growth rate is decreasing and still positive and the radius is growing slowly. Afterwards the bubble cannot converge to a stable state. The growth rate keeps increasing until the asymptotic value $\dot{R}_{lim} = 6.2$ m/s and the radius grows therefore indefinitely. This value is similar to the theoretical approximation $\dot{R}_{lim} = 5.54$ m/s, given by equation (5).

3.2. The initial equilibrium radius

A method was described in section 2 in order to prevent unphysical oscillations. It consists in solving equation (6) to evaluate the equilibrium radius R_0. In order to validate the implementation of this method, it is applied to a bubble of radius R(t_e)= 50 μm under the ambient pressure $p_0 = 101$ kPa and for different values of $p(t_e)$ (0, 10 and 20 kPa). For $p(t_e) = 0$, the condition $R_0 = 50$ μm yields a constant radius because the stable bubble is not subjected to any disturbance. Figure 3(a) shows that the radius oscillates (dotted and dashed-dotted lines) to adjust to a new equilibrium for

11
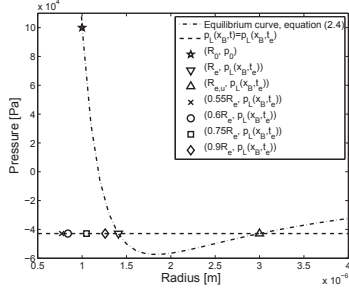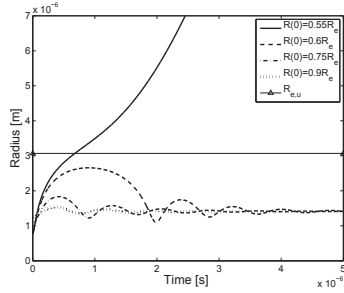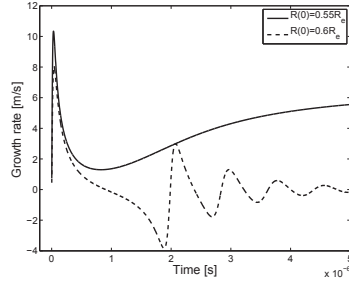
Figure 2: (a) The equilibrium curve corresponds to equation (4) for a bubble with the equilibrium state (R_e=1.4 μm, $p_L(\mathbf{x}_B, t_e) = -42.9$ kPa), symbol ∇. The pressure is kept constant and the initial values of the bubble radius R(0) differ from R_e (symbols $*$, $\circ$, $\square$ and $\diamond$). (b) Temporal evolution of the bubble radius calculated with equation (1) for different values for the initial radius R(0). The oscillations converge rapidly to R_e, except for the case $R(0) = 0.55 R_e$, where the radius grows indefinitely once the unstable radius $R_{e,u}$ is reached. (c) Temporal evolution of the growth rate for a case of radius oscillations and the case of infinite growth.

12

the cases $p(t_e) \neq 0$ and $R_0 = 50$ μm. For the fourth and fifth lines, R_0 is calculated with equation (6) to yield equilibrium, therefore the radii obtained with equation (1) are constant in these cases, $R(t) = R(0)$. It emphasizes that for each value of the pressure $p(t_e)$ the method successfully evaluates an equilibrium radius R_0 corresponding to p_0 that prevents oscillations of $R(t)$.

The values of R_0 calculated with equation (6) are shown on their respective equilibrium curve, equation (4), in Figure 3(b). R_0 is 51.1454 μm (symbol $\triangle$) and 52.2165 μm (symbol $\blacktriangle$) for $p(t_e)=10$ and 20 kPa respectively. In this figure, the initial value of the radius is depicted with the symbols $\circ$, $\square$ and $\blacksquare$ for the different cases. The equilibrium curve (e_0) corresponds to a bubble with the equilibrium state $(p_L(\mathbf{x}_B, t) = p_0 =101$ kPa, $R_0 = 50$ μm). When R_0 (symbol $\triangle$) is calculated with equation (6), the radius follows the equilibrium curve (e_{10}) such that the initial radius R(0)=50 μm corresponds to the equilibrium radius (symbol $\square$) on this curve for a pressure $p_L(\mathbf{x}_B, 0) = p_0 + 10$ kPa. Similarly, with the calculated radius R_0 (symbol $\blacktriangle$), the radius follows the equilibrium curve (e_{20}) such that the initial radius R(0)=50 μm corresponds to the equilibrium radius (symbol $\blacksquare$) on this curve for a driving pressure $p_L(\mathbf{x}_B, 0) = p_0 + 20$ kPa.

In the case of a liquid pressure $p_L(\mathbf{x}_B, t) = p_0 + 10$ kPa, and an initial radius $R(0) = R_0 = 50$ μm, the radius tends to reach the equilibrium value R_e corresponding to this pressure, it is denoted with the symbol $\triangledown$ in Figure 3(b). Therefore the radius R(t) shown in Figure 3(a) oscillates around this value $R_e = 48.88$ μm. In the case of a pressure $p_L(\mathbf{x}_B, t_e) = p_0 + 20$ kPa, the same explanation applies and the radius oscillates around the equilibrium radius $R_e = 47.879$ μm denoted with the symbol $\blacktriangledown$. The amplitude of the first oscillations is in the range of $|R_e - R(0)|$ and is therefore larger in this case. For both cases producing size oscillations, the dissipation between two periods is hardly discernible and it takes around 8 ms for the radii to converge to their equilibrium values. The weak damping is due to the negligible effect of the viscosity and surface tension for large bubbles. This feature is illustrated with the results obtained for a smaller bubble under similar pressure conditions, and $R_0 = R(0) = 1.4$ μm. The evolution of the radii in Figure 4 show that the equilibrium values are reached within less than 8 μs. The amplitude of the oscillations decreases faster due to the stronger effect of viscosity and surface tension for smaller bubbles through the term $4\mu_L \frac{\dot{R}}{R}$ and $\frac{2\sigma_{st}}{R}$ in equation (1). For each case of size oscillations, the period of the oscillations is evaluated from the results R(t) shown in Figures 3(a) and 4. These results, indicated in Table 1, are in perfect agreement with the

	Simulations [s]	T=$1/f_0$ [s]
$p(t_e)$=10kPa, $R_0 = R(0) = 50\ \mu$m	$1.4285 \cdot 10^{-5}$	$1.4276 \cdot 10^{-5}$
$p(t_e)$=20kPa, $R_0 = R(0) = 50\ \mu$m	$1.341 \cdot 10^{-5}$	$1.3387 \cdot 10^{-5}$
$p(t_e)$=10kPa, $R_0 = R(0) = 1.4\ \mu$m	$3.065 \cdot 10^{-7}$	$3.06496 \cdot 10^{-7}$
$p(t_e)$=20kPa, $R_0 = R(0) = 1.4\ \mu$m	$3.205 \cdot 10^{-7}$	$3.20074 \cdot 10^{-7}$

Table 1: Periods of the oscillation obtained from the resolution of equation (1) and estimated with equation (7).

theoretical approximations obtained from the bubble resonance frequency, equation (7).

3.3. Energy dissipation

The variation of the different kinds of energy during the collapse is studied for a bubble initially expanded from its equilibrium state (R_0, p_0). The initial radius is $R(0) = 20R_0 = 5\ \mu$m and the liquid pressure is constant $p_L(\mathbf{x}_B, t) = p_0 = 70$ kPa. Figure 5(a) shows that the bubble radius converges to the equilibrium radius R_0 within less than 1 μs. Figure 5(b) illustrates the temporal evolution of the various energies when the bubble undergoes collapse and rebounds. Figure 5(c) shows the peak pressure emitted by the collapsing bubble. Denoting E_{B0} the initial bubble energy, the energy dissipated during the first collapse is estimated with equation (11) as $E_{diss} = 92\% E_{B0}$ while the energy of the shock wave calculated with equation (12) is $E_{SW} = 10\% E_{B0}$. These results are in the range of experimental data. Kling and Hammit (1972) suggested that 50 to 70% of the bubble energy is dissipated by thermal radiation, production of the pressure wave and formation of permanent gas. Vogel and Lauterborn (1988) predicted that the average energy loss of the cavitation bubble during their first collapse is 84%. They also show that the fraction of the energy loss converted in acoustic energy range from 10 to 90 % while Brujan et al. (2005) reported that around 30 % of the bubble energy was converted into acoustic energy.
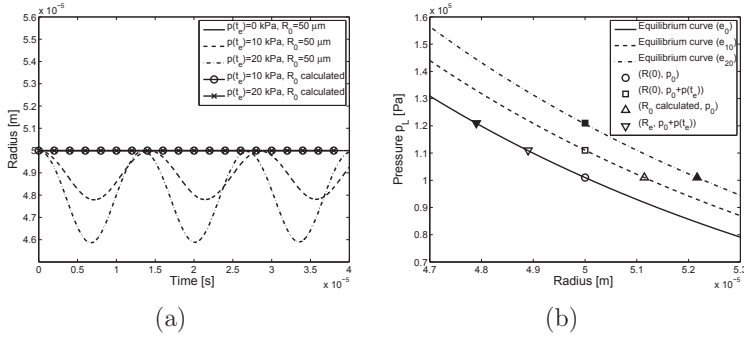
Figure 3: The initial radius is $R(0) = 50$ μm and the liquid pressure is constant $p_L(\mathbf{x}_B, t) = p_0 + p(t_e)$. (a) The temporal evolution of the bubble radius calculated with equation (1) for different values of $p(t_e)$ (0, 10 and 20 kPa) and R_0 (50 μm or calculated with equation (6)). The first, fourth and fifth lines are overlapping each other. The dotted and dashed-dotted lines show that oscillations occur when the bubble is not initially in equilibrium. (b) The equilibrium curve (e_0) corresponds to equation (4) for a bubble with the equilibrium state (p_0=101 kPa, $R_0 = 50$ μm), symbol $\circ$. The equilibrium curve (e_{10}) corresponds to equation (4) for a bubble with the equilibrium state (p_0=101 kPa, $R_0 = 51.1454$ μm), symbol $\triangle$. The equilibrium curve (e_{20}) corresponds to equation (4) for a bubble with the equilibrium state (p_0=101 kPa, $R_0 = 52.2165$ μm), symbol $\blacktriangle$. The radius oscillations shown in Figure (a) vary about the mean values depicted with symbols ∇ and $\blacktriangledown$ in Figure (b)

15
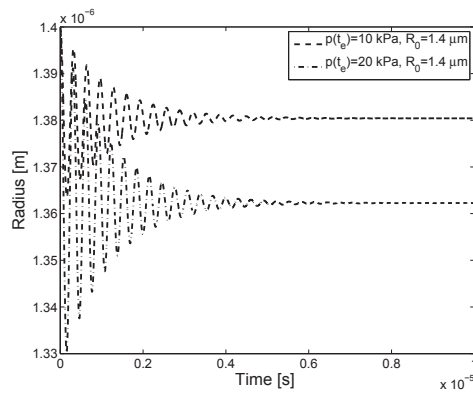
Figure 4: The initial radius is $R(0) = 1.4$ μm and the liquid pressure is constant $p_L(\mathbf{x}_B, t) = p_0 + p(t_e)$. The temporal evolution of the bubble radius calculated with equation (1) for different values of $p(t_e)$ (10 and 20 kPa) and R_0=1.4 μm.
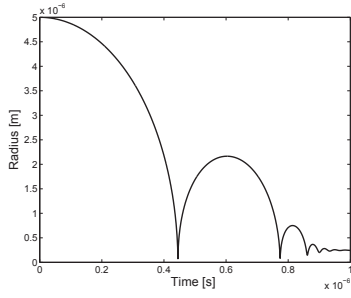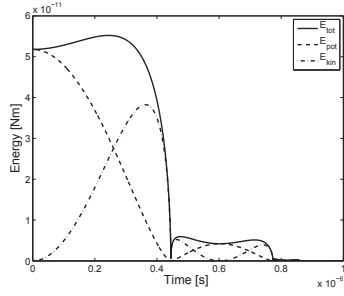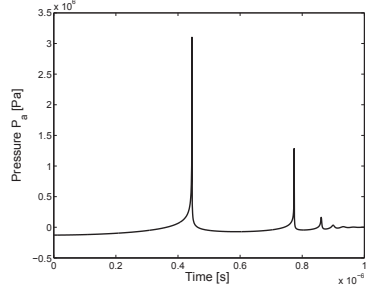
Figure 5: (a) The temporal evolution of the bubble radius. (b) Temporal evolution of the bubble energy. (c) Pressure $p_a(\mathrm{R}(0))$ emitted at the distance $\mathrm{R}(0)$ from the center of the bubble.

3.4. The radius evolution

The implementation of the Rayleigh-Plesset model is validated by investigating the dynamic behaviour of various bubbles subjected to different pressure variations. The numerical results are compared with previous numerical studies and with experimental data.

Alehossein and Qin (2007) investigated the influence of the amplitude of a step pressure drop. For a small drop in pressure (13 kPa), different integration methods (Euler and Runge-Kutta) using fixed time step produced similar results. A larger pressure drop (130 kPa) was more challenging numerically and an adaptive time step method was required to resolve the collapse phase. The pressure profile is shown in Figure 6(a). In Figure 6(b), the results from the present study are compared with the work of Alehossein and Qin (2007). They differ in several aspects. The amplitude and the period of the oscillations are different. The noteworthy discrepancy is that the radius in the present simulation is strictly increasing at the beginning while Alehossein and Qin (2007) predict a decrease of the radius at the beginning under the decrease of the pressure. This is only possible if the initial state of the bubble is actually not at equilibrium as explained previously. Either the initial pressure or the initial radius used in their computations has a value which differs from the equilibrium state and leads to oscillations. In order to confirm this, simulations were performed with a lower equilibrium pressure ($p_0 = 12$ kPa) or a lower equilibrium radius (R_0=7 μm) instead of the equilibrium values ($p_0 = 120$ kPa, R_0=10 μm). The results obtain with these parameter are good agreement with Alehossein and Qin (2007). However the results obtain in the present work with a bubble initially equilibrated give a more realistic description of the bubble size evolution. These results emphasize the importance of the choice of the parameter p_0 and R_0 in equation (1).

Another case of bubble collapse is simulated and the results are compared with the experimental measurement of Tomita and Shima (1986) and the numerical results of Alehossein and Qin (2007). The simulation is started from the maximum bubble size ($\dot{R}(0)$=0, R(0)=0.75 mm) and describes the collapse under a constant liquid pressure. Figure 7 shows the results obtained with the assumption R_0=0.3 μm. The result obtained in the present work is in good agreement but over predicts slightly (9 %) the collapse time. The simulation successfully describes the collapse and the following rebound despite the extremely high velocity of the bubble interface shown in Figure

18
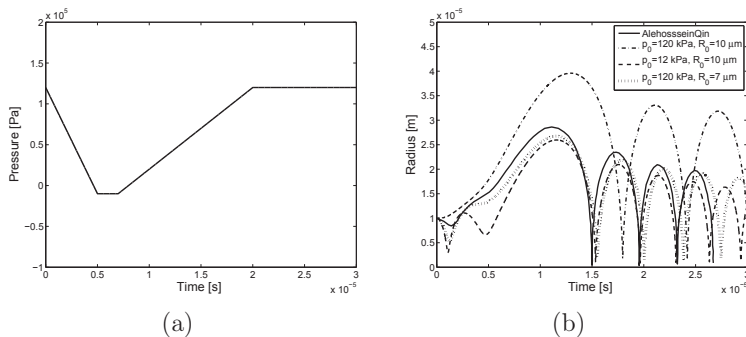
Figure 6: (a) The temporal evolution of the pressure and (b) the resulting bubble radius for different values of the equilibrium state. The oscillations at the beginning of the computations are removed when the bubble is initially equilibrated.

7(b). The value of the growth rate at collapse shows that the assumption of incompressibility is theoretically not applicable anymore in this case.

Lauterborn et al. (2007) presented numerical calculations which matched the data from photographic observations of a bubble collapsing in a water-glycerin mixture. The same experimental data are used by Ohl et al. (1999) and the numerical results are based on different parameters listed in Table 2. The liquid pressure is $p_L(\mathbf{x}_B, t) = p_0 + sin(2\pi f_0 t)$ with p_0=100 kPa and f_0=21.4 kHz. Figure 8(a) shows the results obtained with the present implementation using the set of parameters suggested by Lauterborn et al. (2007) and Ohl et al. (1999). The phase of growth is similar while the rebounds are damped for a higher value of the viscosity. In order to fit the experimental data, the parameters used by Ohl et al. (1999) are modified in order to enhance the damping and the value $\mu = 0.015$ kg/m s gives a very good agreement (Figure 8(b)). The strong influence of the viscosity on the bubble size R_{reb} at rebound is noteworthy. Following the energy approach described in section 2.1, it appears that the energy dissipated during the collapse relies on this value R_{reb} in equation (11). The predicted energy
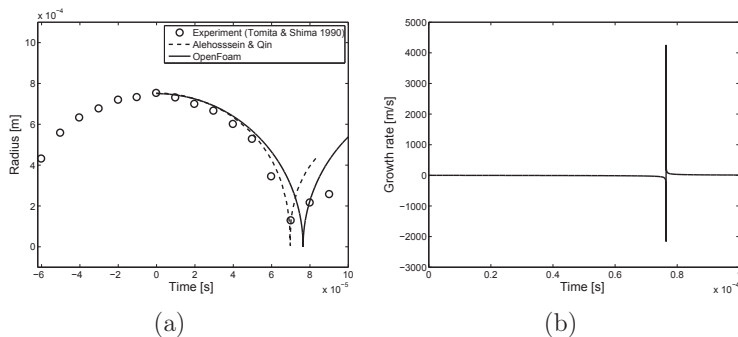
Figure 7: The temporal evolution of the (a) bubble radius and (b) growth rate

	R_0	p_v	σ_{st}	μ	κ
Lauterborn et al. (2007)	$8.1e^{-6}$	0	0.0725	0.0018	1.2
Ohl et al. (1999)	$8e^{-6}$	2500	0.07	0.006	1.33

Table 2: Parameters used in Lauterborn et al. (2007) and Ohl et al. (1999) for the numerical calculations of a bubble collapsing in a water-glycerin mixture.

loss during the collapse shown in Figure 8(a) varies from 47% to 72% of the maximal bubble energy E_{B0} depending on the alleged value set for the liquid viscosity in the numerical calculations. According to the experimental data, $E_{diss} = 95\% E_{B0}$. This highlights the uncertainty of this energy approach in the context of numerical simulations. For any particular case of collapsing bubble, there exists appropriate parameters such that equation (1) produces a temporal evolution of the radius which overlaps the experimental data. However in a general case of numerical calculations of random bubbles, there is no specific set of parameters which leads to reliable values of R_{reb} and consequently of the energy dissipated during the collapses.
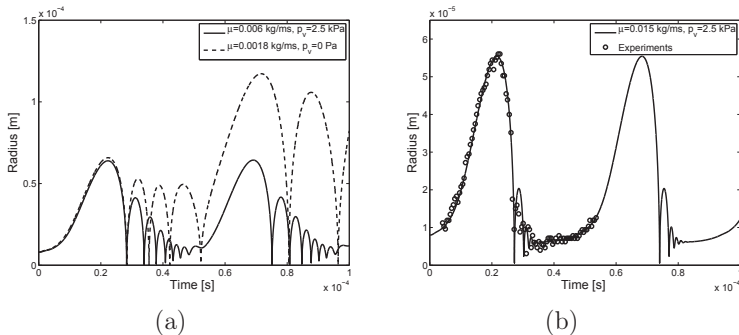
Figure 8: The temporal evolution of the bubble radius (a) for the parameters given by Lauterborn et al. (2007) and Ohl et al. Ohl et al. (1999), (b) with the parameters given by Ohl et al. (1999) and a higher viscosity to fit their experimental data.

4. Bubble transport

In the discrete bubble model, a bubble is represented as a particle tracked with a Lagrangian particle tracking method. The bubble is considered as a point source when modelling the interaction with the surrounding fluid and it is modeled as a hard sphere particle when modelling the interaction with solid surfaces. A bubble of radius R is defined by the position of its center, $\mathbf{x}_B$ and its velocity, $\mathbf{U}_B$. The volume of the bubble is $V_B = \frac{4}{3}\pi R^3$ and its mass is $m_B = \rho_B V_B$. In a Lagrangian frame, each bubble position vector $\mathbf{x}_B$ is calculated from the equation

$$\frac{d\mathbf{x}_B}{dt} = \mathbf{U}_B, \tag{15}$$

and the motion of each bubble is governed by Newton's second law

$$m_B \frac{d\mathbf{U}_B}{dt} = \mathbf{F_a} + \mathbf{F}_p + \mathbf{F}_{buoy} + \mathbf{F_{drag}} + \mathbf{F}_{vol} + \mathbf{F}_{lift}. \tag{16}$$

The forces acting on the bubble are the added mass force, the pressure gradient force, the buoyancy force, the drag force, the force due to volume variation

21

of the bubble and the lift force.

$$\mathbf{F}_a = \tfrac{1}{2}\rho_L \tfrac{m_B}{\rho_B}\left(\tfrac{D\mathbf{U}_L}{Dt} - \tfrac{d\mathbf{U}_B}{dt}\right),$$

$$\mathbf{F}_p = -\tfrac{m_B}{\rho_B}\nabla p_L,$$

$$\mathbf{F}_{buoy} = m_B(1 - \tfrac{\rho_L}{\rho_B})\mathbf{g},$$

$$\mathbf{F}_{drag} = C_{drag}\rho_L \tfrac{m_B}{\rho_B}\tfrac{3}{8R}(\mathbf{U}_L - \mathbf{U}_B)|\mathbf{U}_L - \mathbf{U}_B|,$$

$$\mathbf{F}_{vol} = \tfrac{1}{2}\rho_L \tfrac{dV_B}{dt}(\mathbf{U}_L - \mathbf{U}_B) = \rho_L \tfrac{m_B}{\rho_B}\tfrac{3\dot{R}}{2R}(\mathbf{U}_L - \mathbf{U}_B),$$

$$\mathbf{F}_{lift} = C_{lift}\rho_L \tfrac{m_B}{\rho_B}(\mathbf{U}_L - \mathbf{U}_B) \times \omega_L.$$

Empirical relations of drag, lift and added mass effect for spherical non-rotating particles are considered in this model and

- $\frac{D\mathbf{U}_L}{Dt}$ is the total acceleration of the fluid as seen by the particle ($\frac{D\mathbf{U}_L}{Dt} = \frac{d\mathbf{U}_L}{dt} + \mathbf{U}_L \cdot \nabla\mathbf{U}_L$) evaluated at the particle position,

- $\mathbf{g}$ is the gravitational acceleration,

- C_{lift} is the lift coefficient, assumed to take the value 0.5 according to Auton (1987),

- ω_L is the vorticity of the fluid, $\omega_L = \nabla \times \mathbf{U}_L = (\frac{\partial w}{\partial y} - \frac{\partial v}{\partial z})\mathbf{n_x} + (\frac{\partial u}{\partial z} - \frac{\partial w}{\partial x})\mathbf{n_y} + (\frac{\partial v}{\partial x} - \frac{\partial u}{\partial y})\mathbf{n_z}$,

- C_{drag} is the drag coefficient which depends on the bubble Reynolds number

$$\mathrm{Re}_B = \frac{2\rho_L R|\mathbf{U}_L - \mathbf{U}_B|}{\mu_L}.$$

The experimental study of Haberman and Morton (1953) indicates that the drag coefficient of a bubble is equal to the drag of a rigid sphere for $Re_B{<}40$. The discrepancy at higher Reynolds number is due to the internal circulatory motion and the deformation of the bubble. This range is out of the scope of this study because strictly spherical bubbles are considered. For very small Reynolds number (≤ 0.1), the Stokes law is valid and the drag coefficient is $C_{drag} = \frac{24}{Re_B}$. For larger Reynolds

number, an empirical law, proposed by Schiller and Nauman (1935) is used:

$$C_{drag} = \frac{24}{Re_B} \left(1 + 0.15 Re_B^{0.687} \right).$$

Equation (16) was introduced in the context of solid particles by Stokes (1850) and modified by Boussinesq (1903) and Maxey and Riley (1983) among other. Besides particle rotation, the present model also neglects the Basset history force due to the viscous stress on the particle surface, as well as the Faxen correction on the drag force that accounts for non uniform flow effects. In order to account for the specificity of a bubble compare to a solid particle, Johnson and Hsieh (1966) introduced a force due to the variation of the volume. They assumed that this force was negligible except at the time of collapse. Hence this force was not included in their numerical computations of bubble trajectories. This force was accounted for by Giannadakis et al. (2008), Hsiao et al. (2005) and Shams and Apte (2009), among others, without further comments. However the analysis performed in section 5.2 shows that this force has an erroneously large contribution at collapse. Therefore the force F_{vol} is neglected in the present work except when its influence is discussed in section 5.2.

After rearranging terms, equation (16) becomes

$$\frac{d\mathbf{U}_B}{dt} = \frac{1}{\frac{\rho_B}{\rho_L} + \frac{1}{2}} \left(\frac{1}{2} \frac{D\mathbf{U}_L}{Dt} - \frac{1}{\rho_L} \nabla p_L + \left(\frac{\rho_B}{\rho_L} - 1 \right) \mathbf{g} \right.$$
$$+ \left(\frac{3C_{drag}|\mathbf{U}_L - \mathbf{U}_B|}{8R} + \frac{3\dot{R}}{2R} \right) (\mathbf{U}_L - \mathbf{U}_B) + C_{lift}(\mathbf{U}_L - \mathbf{U}_B) \times \omega_L), \tag{17}$$

where the term $\frac{3\dot{R}}{2R}$ is only accounted for when the contribution of the force F_{vol} is studied. Finally the discrete bubble model consists in solving the system of 6 first-order ODEs given by equations (15) and (17) with the Rosenbrock integration method. The matrix formulation and the coefficients of the Jacobian matrix needed by the time integration method are derived in Appendix A. During the Eulerian time step dt, each bubble is tracked by solving the equations (15) and (17) at least once and at most as many times as the times the bubble trajectory crosses a cell. Therefore there is a specific distribution of the Lagrangian time steps $dt_L^j, j = 1..N_i$ within an Eulerian time step dt for each bubble B_i such that $dt = \sum_{j=1}^{N_i} dt_L^j$ for any B_i .

4.1. Flow turbulence

A steady state simulation of the flow field is initially performed using a RANS model for the turbulence and the bubbles are tracked in the resulting converged mean flow field. With this approach, the turbulent fluctuations are not included because the fluid velocity interpolated at the bubble position, $\mathbf{U}_L$, does not contain a fluctuating component due to the turbulence. Therefore the bubbles trajectories follow the streamlines of the mean flow. However, the effect of turbulent dispersion of the bubbles can be artificially added with a random walk model at each Lagrangian time step (see e.g. Gosman and Ioannides (1983)). The principle is that eddies are created randomly and affect the bubble trajectory to mimic the fact that small bubbles are trapped in eddies for a certain period of time. In practice, a local fluctuating component is added to the fluid velocity at the position of the bubble, i.e. $\mathbf{U}_L$ becomes $\tilde{\mathbf{U}}_L = \mathbf{U}_L + \mathbf{U}_L^{fluct}$ in equation (17). The local fluctuating velocity is estimated by

$$\mathbf{U}_L^{fluct} = \psi\sqrt{\frac{2}{3}k},$$

where $\sqrt{\frac{2}{3}k}$ is the local RMS fluid velocity fluctuations for isotropic turbulence and ψ is a random number generated from a Gaussian distribution of zero mean and variance one. The eddy life time (t_{eddy}) and the time needed by the bubble to traverse the eddy (transit time t_{tr}) are calculated as

$$t_{eddy} = \frac{C_\mu^{0.63}\frac{k^{1.5}}{\epsilon}}{|\mathbf{U}_L^{fluct}|},$$

$$t_{tr} = -\tau_B ln(1 - \frac{l_e}{\tau_B|\tilde{\mathbf{U}}_L - \mathbf{U}_B|}),$$

where τ_B is the relaxation time of the bubble, i.e the time it takes for a bubble to respond to changes in the local flow velocity. It is expressed as

$$\tau_B = \frac{8}{3}\frac{\rho_B R}{\rho_L C_{drag}|\tilde{\mathbf{U}}_L - \mathbf{U}_B|}.$$

The random walk algorithm consists in evaluating $\mathbf{U}_L^{fluct}$ with a random number ψ, calculating the characteristic times t_{eddy} and t_{tr} and keeping $\mathbf{U}_L^{fluct}$ constant during the interaction time $dt_{turb} = min(t_{eddy}, t_{tr})$ in order to evaluate $\mathbf{U}_B$ according to equation (17) during this interaction time. In practice

the time step dt_L^j used to solve equation (17) with the modified velocity can be shorter than the interaction time if the bubble trajectory crosses a cell before its completion. Therefore the time step used is actually $min(dt_L^j, dt_{turb})$. In the present work, the random-walk model is used for the computations of bubbles released randomly in the domain in order to account for the turbulence effect in the statistical results (section 5.3). However the random walk model is not included in the context of parameter studies (section 5.2). Indeed for these cases, the bubbles injected at a given position must follow exactly the same trajectory and be submitted to the same pressure p_L such that the discrepancy of the results are only attributed to the variation of the concerned parameter (reference pressure, release location or initial size).

4.2. Wall treatment

The influence of the impact of a bubble with a wall boundary on the bubble behaviour is difficult to model. Experimental studies consider either the trajectory of non-cavitating bubbles colliding on a wall or cavitating bubble collapsing near a wall without approach velocity. In the case of cavitation in water turbines both the motion and the dynamics are involved which increases the complexity of the phenomenon. In the case of a still bubble released and collapsing near a wall, it is known that the bubble undergoes deformations due to the wall. Experiments show that this deformation gives rise to a liquid jet separating the bubble and impacting the wall which is supposed to be responsible for erosion pits when the bubble is accelerated toward the boundary during the collapse phase (see e.g Brujan (2004) and Plesset and Chapman (1971)). The risk of damage increases for bubbles in contact with the wall because the liquid jet impacts directly the wall without dissipation through the liquid film between the bubble and the wall. Furthermore a bubble close to the wall may undergo collapse under the influence of the shock waves emitted by bubbles collapsing further away from the solid surface. The deformation of the bubble, the liquid jet and the possible bubble breakup are not resolved in the present study as the bubbles are assumed spherical at all time as a first approximation. In order to account for the effect of the impact with the wall on the bubble expansion, the bubble growth is not evaluated at the instant the bubble impacts a wall. After the collision, the bubble dynamics is solved with a growth rate set to zero, as suggested by Giannadakis et al. (2008).

In practice, an impact with a wall is modeled when the bubble trajectory crosses a face f_w of the wall boundary. Neglecting the actual flattening of the

bubble when it approaches a surface boundary, it is assumed that a collision occurs when the distance from the spherical bubble center to the center of the face is equal to the bubble radius. Denoting $\mathbf{n}_w$ and $\mathbf{t}_w$ the normal and tangential unit vectors of f_w, the bubble velocity before the impact is written as

$$\mathbf{U}_B^0 = U_B^{0n}\mathbf{n}_w + U_B^{0t}\mathbf{t}_w.$$

Non-cavitating bubbles colliding against a wall either bounce, stick or slide depending whether inertia or dissipation dominates the process and experiments show the presence of a liquid film between the bubble and the wall at collision, as shown by Podvin et al. (2008). Zenit and Legendre (2009) showed that the behaviour of a bubble colliding with a wall was different from a solid sphere due to the liquid film and the bubble deformation. They found that the coefficient of restitution ϵ_w depends on the capillary number $Ca = \frac{\mu_L U^{0n}}{\sigma_{st}}$ and the modified Stokes number $St^* = \frac{(\rho_B + \frac{1}{2}\rho_L)2RU^{0n}}{9\mu_L}$, it reads

$$\epsilon_w = e^{-30\sqrt{Ca/St^*}}.$$

The normal component of the bubble velocity after the impact is evaluated as $U_B^n = -\epsilon_w U_B^{0n}$ and the tangential component is unchanged as friction is neglected.

5. Results

5.1. Problem set-up

The overall model is applied to the simulation of small bubbles travelling in the low pressure region above a rectangular cylinder of dimension [10h, 2h, 7h] with $h = 6$ mm (Figure 9). The origin of the domain is located on the leading edge and at the centerline of the cylinder. In the plane z=0, the cylinder is attached to an infinite wall. The inlet and the outlet are located in the plane x=-40h and x=60h respectively. Symmetry boundary conditions are applied to the remaining boundaries of the computational domain (planes y=30h, y=-30h and z=11h).

The fluid flow is first obtained from RANS simulations with the kωSST model for the turbulence. The inlet velocity is $\mathbf{U}_L = 15$ m/s. The reference pressure, p_0, is the liquid pressure of the undisturbed flow, i.e. the value imposed at the outlet boundary. Next, bubbles of different sizes are injected in front of the cylinder and tracked with the discrete bubble model.
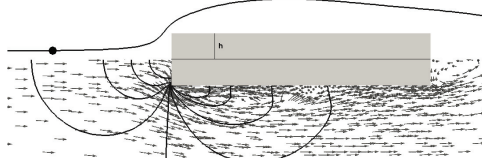
Figure 9: Plane z=4h of the computational domain. Pressure contours and velocity vectors are shown in the bottom half. A stream line passing the location of a bubble (symbol ●) released at $\mathbf{x}_{B0} = (-5h, 0.4h, 4h)$ is shown in the upper half.

The mesh used to compute the fluid flow is referred as the Eulerian mesh and is chosen fine enough to capture the flow details such as the recirculation zone over the obstacle. It is refined in the vicinity of the wall in order to resolve the boundary layer. The tracking of the bubbles is done on a coarser and uniform mesh to ensure that the bubble size is always smaller than the cell size, even when the initially small bubbles grow up to several orders of magnitudes. The choice of this Lagrangian mesh is motivated by two distinct reasons. First, it is advantageous to use a uniform mesh because it reduces the number of Lagrangian sub-time-steps dt_L^j when the bubbles evolve close to the wall compared with the use of the refined Eulerian mesh. The Eulerian time step used for modelling the bubble transport is small enough ($dt = 1e^{-5}$) such that the accuracy of the results is not altered by the size of the Lagrangian cells. Secondly, the size of the bubble must be smaller than the cell due to the implementation of the model for bubble collision with a wall. The approach allows collision only for bubbles with centroid located in a cell connected to the wall surface. This limitation implies that the bubble radius has to be smaller than the edges of the host cell which are connected to the wall face f_w. Therefore, a coarser mesh is necessary to resolve properly the wall collision events.

A bubble injected in the free stream would be initially equilibrated at the liquid pressure p_0. However, in order to save computational time, the bubble is initially released close to the obstacle, at a distance $x = -5h$ from the leading edge. Thus the initial pressure is not p_0 at this location. It is therefore necessary to compute the equilibrium radius R_0 with equation (6) in order to avoid the effect of the release location on the bubble dynamics.

When solving for the bubble dynamics, the pressure $p_L(\mathbf{x}_B, t)$ is the liquid pressure interpolated at the centroid position if the bubble is smaller than the Eulerian host cell. As the bubble grows, it may become larger than the host cell in the Eulerian grid and the driving pressure is calculated as the average of the liquid pressures interpolated at the cells containing the bubble volume. This yields a more realistic approximation of the forces over the bubble surface.

5.2. Parameter study

Bubbles with different initial radius (R(0)=10 and 50 μm) are injected at the same positions $\mathbf{x}_{B0} = (-5h, 0.2h, 4h)$ in front of the obstacle and the evolution of their size is solved with the Rayleigh-Plesset equation while they are travelling downstream. The random walk model is not included in this parameter study, as mentioned in section 4.1. Hence bubbles released at the same position follow exactly the same streamline and are subjected to the same liquid pressure. This parameter study focuses on the collapse features, therefore the calculation of the bubble behaviour is stopped when the maximal rebound radius is reached.

Sensitivity to the reference pressure p_0, Figure 10 and 11. The computations are performed for $p_0 = 50$, 70 and 100 kPa to examine the sensitivity to the reference pressure. Figure 10(a) shows the temporal evolution of the bubble sizes for the largest reference pressure. When a bubble arrives in the low pressure region, its radius increases. It then reaches a region with a higher pressure where it almost recovers its initial size. These bubbles don't undergo collapse under this pressure distribution because the pressure is above the critical value and the bubble stays therefore in equilibrium. With a lower reference pressure, the bubble growth is enhanced and the bubbles collapse, as depicted in Figure 10(b). The discontinuity observed during the bubble growth is due to the implementation of the algorithm for the collision with the obstacle wall. The growth rate is set to zero when the bubble hits the wall as explained in section 4.2. Figure 11 shows the interpolated liquid pressure along the bubble trajectory as well as the rate of growth (dashed line). When the pressure is below the critical value p_c, the rate of growth increases such that the bubble radius becomes two orders of magnitudes larger. When the bubble is transported downstream, the increase of the pressure above p_c yields the decrease of the rate of the growth. However the radius continues to grow as long as the growth rate is positive. When the rate of growth becomes negative, the bubble collapses.

When the reference pressure is further decreased ($p_0 = 50$ kPa), the pressure is kept below the critical values p_c long enough for the bubbles to grow into macroscopic bubbles (Figure 10(c)). In this case the large bubbles leave the computational domain without collapsing. In the following, the ambient pressure is set to 70 kPa as it produces the most relevant results in the context of erosion due to the presence of collapsing bubbles.

Sensitivity to the release height y_0, Figure 12. The evolution of the bubble size depends also on the release location. A bubble that follows a streamline closer to the obstacle is subject to a lower pressure and its growth is therefore enhanced as shown in Figure 12(a). The bubble injected at y=0.4h reaches a maximum radius $R_{max} \sim 10R(0)$ and collapses at a distance $\delta = 4 \cdot 10^{-3}$ m from the wall. A bubble released at a lower location (y=0.2h) grows faster such that its surface hits the wall during the growth phase and the bubble collapse occurs further away from the wall ($\delta = 10 \cdot 10^{-3}$ m).

Sensitivity to the initial size $R(0)$, Figures 10(b), 13 and 14 . The bubble initially at 50 μm grows until $R_{max} \sim 110R(0)$ and its collapse gives rise to a large pressure peak as shown in Figure 13(a). Even if the initially smaller bubble reaches a lower value R_{max}, its collapse is stronger because the bubble grows up to $350R(0)$ and is accordingly compressed until a smaller size upon collapse. Therefore the pressure peak emitted at the bubble surfaces is larger. The pressure peak radiated to the obstacle, $p_a(\delta)$, is shown in Figure 13(c). It emphasizes that the smaller bubble (symbol $\square$) has a stronger impact on the wall. The symbol $\triangle$ shows the result for the previous case of a larger bubble which collapses closer to the wall, without previous wall collision. In this case the peak pressure at the bubble surface is lower (Figure 13(b)) and its effect on the wall is negligible. Is is explained by the shorter growth phase which leads to a weaker collapse. The dissipated energies depicted in Figure14(a) stress that the total energy loss is not proportional to the energy dissipated in the shock wave. The bubble which lost the largest percentage of its energy during collapse corresponds to the case of the lowest energy dissipated in the shock wave. This is due to the size of the bubble which is much smaller compared to the two other collapsing bubbles studied. Indeed for a smaller bubble, the surface tension and the viscosity play a major role on the damping process. However the total amount of energy loss is larger for
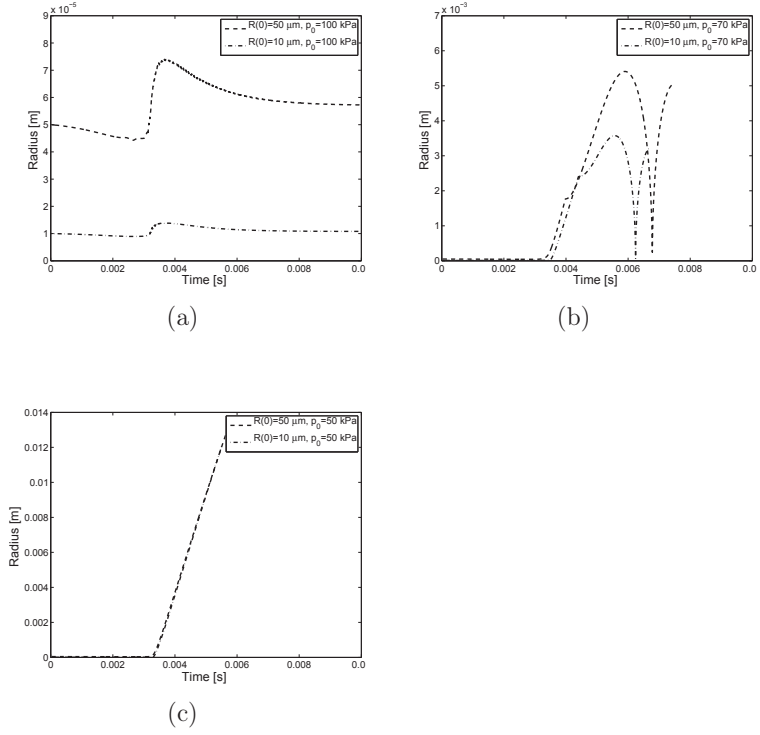
Figure 10: The temporal evolution of the radius for bubbles of different initial sizes, released at the same position $\mathbf{x}_{B0} = (-5h, 0.2h, 4h)$ and travelling near the leading edge for different values of the reference pressure p_0. (a) $p_0 = 50$ kPa (b) $p_0 = 70$ kPa (c) $p_0 = 100$ kPa.
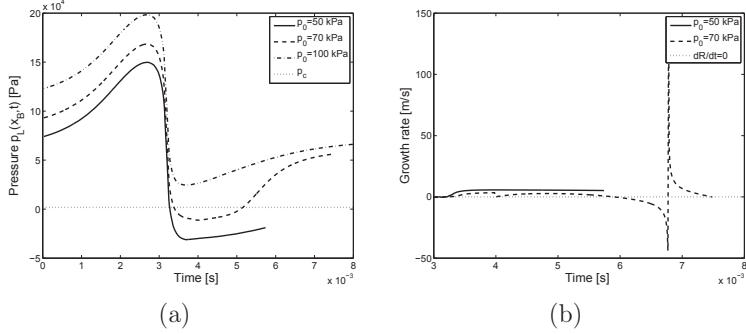
Figure 11: Bubbles of initial size $R(0)$=50 μm, released at the same position $\mathbf{x}_{B0} = (-5h, 0.2h, 4h)$ and travelling near the leading edge for different values of the reference pressure p_0. (a) The temporal evolution of the liquid pressure interpolated at the bubble centroid position. (b) The temporal evolution of the bubble growth rate.
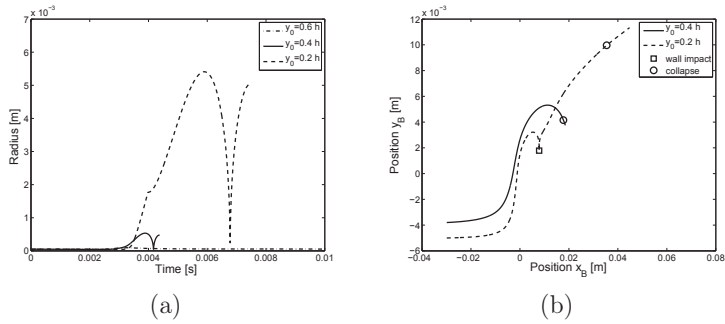
Figure 12: (a) The temporal evolution of the radius for bubbles of different released locations, for $R(0)$=50 μm and $p_0 = 70$ kPa. (b) The trajectory of the collapsing bubbles.

31
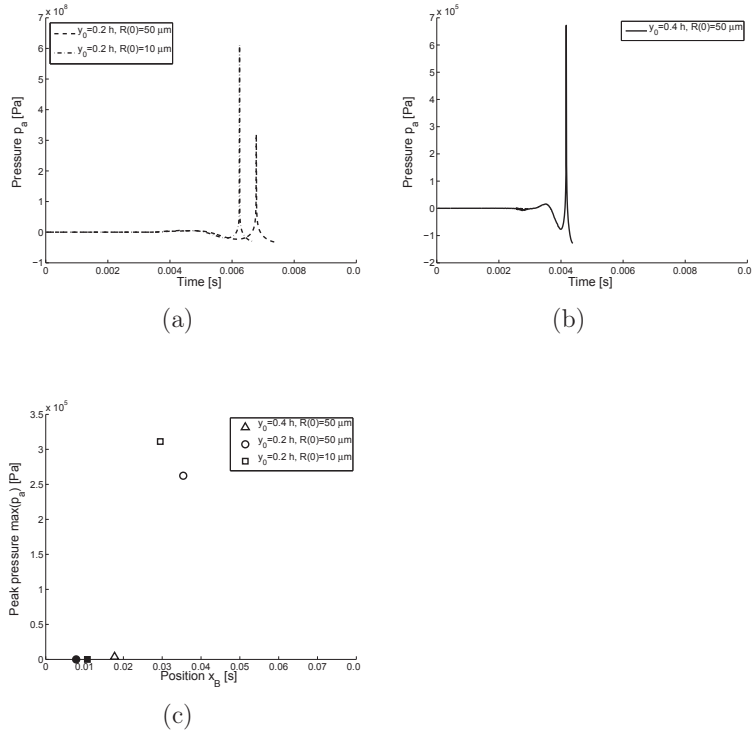
Figure 13: (a) and (b) The acoustic pressure emitted at the bubble surface for the collapsing bubbles. (c) The peak pressure radiated at the wall $p_a(\delta)$ (open symbols) and the location of the impacts for the bubbles which collided with the wall (filled symbols).
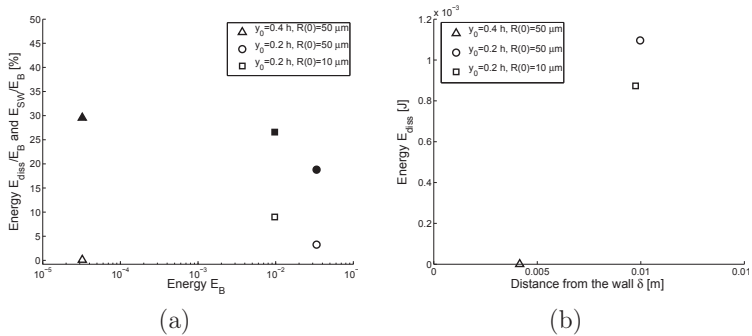
Figure 14: (a) The percentage of energy due to the shock wave (open symbols) and the percentage of energy dissipated during collapse (filled symbols). (b) The total amount of energy dissipated as a function of the distance to the wall.

the bubbles which undergoes a stronger collapse as shown in Figure 14(b).

Sensitivity to the force F_{vol}, Figures 12(a), 15 and 16. For a bubble injected at $\mathbf{x}_{B0} = (-5h, 0.4h, 4h)$ with an initial radius R(0)=50 μm, the temporal evolution of the radius is shown in Figure 12(a) (solid line) when the force F_{vol} is neglected in equation (17). The behaviour of a bubble with the same properties is presented in Figure 15(a) (dashed line) when the force F_{vol} is accounted for. Without F_{vol}, the radius becomes smaller than R_0 when the bubble collapses and the calculations for this bubble are stopped after the first rebound, accordingly to the implemented algorithm. When the force F_{vol} is included in the transport equation, the bubble radius grows less and the collapse is weaker such that the radius is above R_0 even at collapse. Therefore this event is not considered as a collapse by the algorithm and the computations are pursued after the first rebound. The lower value of the radius before the collapse is explained by the distinct trajectories shown in Figure 15(b). During the growth phase, the contribution of the force F_{vol} is larger and opposite to the drag force (Figure 15(c)). It affects the bubble velocity through equation (17) and the trajectory through equation (15).

Hence during the growth phase, the bubble is transported at a higher position where the liquid pressure p_L is larger and the radius grows less. When the successive collapses occur, the variation of $\dot{R}$ yields small oscillations of the bubble trajectory. Another bubble of radius R(0)=50 μm is released at a lower position $\mathbf{x}_{B0} = (-5h, 0.2h, 4h)$. As previously, when F_{vol} is added, the radius grows less (Figure 15(a) compared with Figure 12(a), dashed lines) because the bubble is transported slightly higher during the growth phase. Due to these small changes of the size and the position, the bubble does not hit the wall. The crucial modification observed in the trajectory is the jump upward at collapse. While the presence of the force F_{vol} generated insignificant oscillations observed in Figure 15(b) during a weak collapse, it produces an unrealistic behaviour when the collapse is stronger. Here the strength of the collapse is related to the value of the growth rate which is $\dot{R} \sim 2$ m/s in Figure 15(a) and $\dot{R} \sim 40$ m/s in Figure 16(a). In the case of a stronger collapse, the force F_{vol} offsets the other forces at collapse (Figure 16(c)) and all the components of the velocity $\mathbf{U}_B$ show a sudden large deviation which is not physical. From these observations, it is concluded that the force F_{vol} should not be included in the computations of the transport of collapsing bubbles.

5.3. Sensitivity to the flow features

A large number of bubbles (10 000) of different sizes (ranging from 1 to 50 μm) are released at a random position in a narrow band in front of the cylinder $\mathbf{x}_{B0} = (-5h, [0, h], [z - 0.025h, z + 0.025h])$. Different values of z are used in separate computations in order to study the influence of the flow pattern on the collapses. The difference of the flow field in these planes is the shape of the recirculation zone. Its length is given by the reattachment point in Figure 17(a). In the plane z=6h, the recirculation zone is shorter than in the center of the obstacle (plane z=4h).

As in the previous simulations, the discrete bubble model is used to convect the small bubbles in the flow with equations (15) and (17) and the evolution of the bubble size is described by the Rayleigh-Plesset equation (1). In the present computations, the effect of the fluid turbulence is included with the random-walk model (section 4.1)

The position of each bubble is sampled during its first collapse when the radius reached its smallest value. The resulting probability density functions

(a)

(b)

(c)
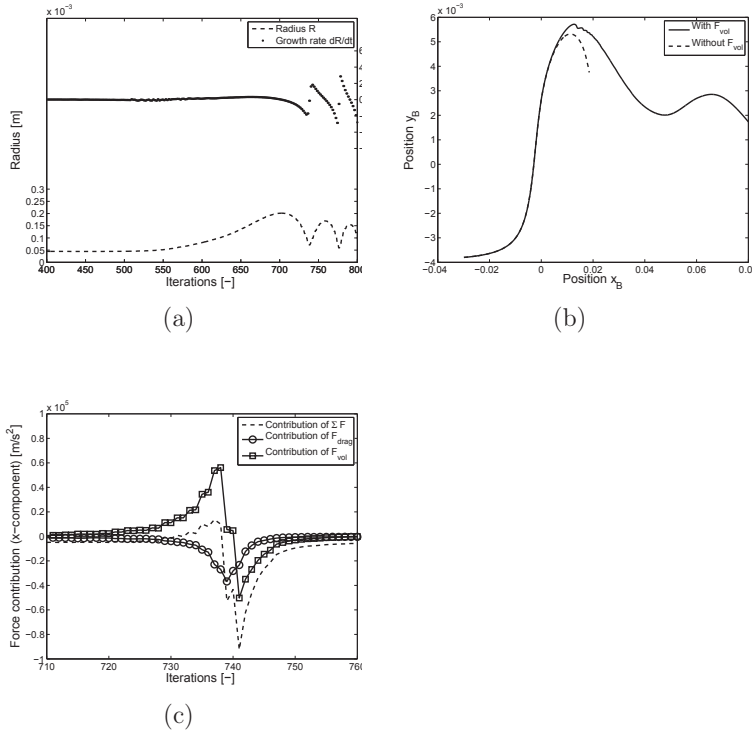
Figure 15: The influence of the force F_{vol} on (a) the temporal evolution of the radius and growth rate (b) the trajectory of the bubble. (c) The contribution of this force compare to the drag force.

35

(a)

(b)

(c)
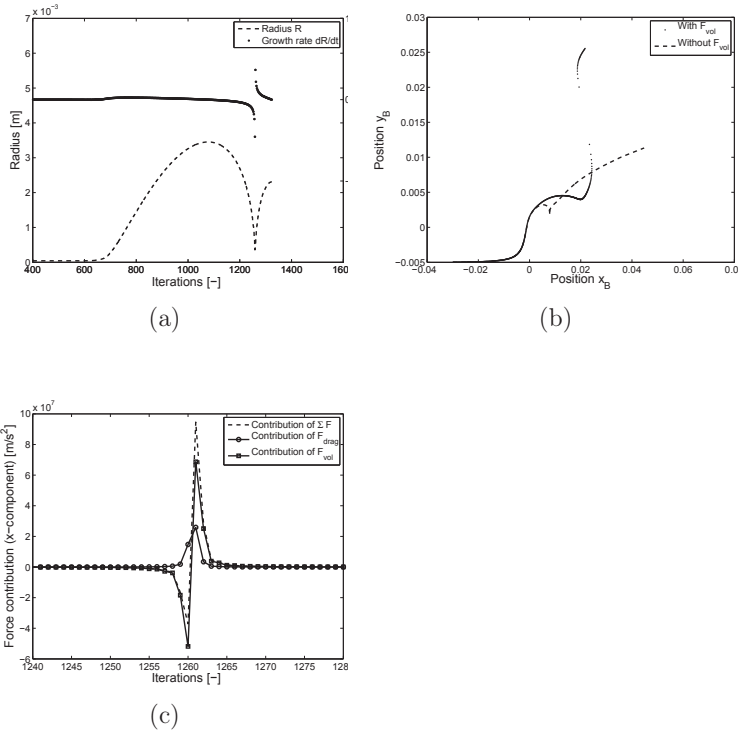
Figure 16: The influence of the force F_{vol} on (a) the temporal evolution of the radius and growth rate , and on (b) the trajectory of the bubble. (c) The contribution of this force compare to the drag force.

36

in Figure 17(b) and (c) indicate the location where the collapses are more likely to happen in the plane z=4h and z=6h. The expected location of the successive collapses is shifted toward the leading edge of the obstacle (plane x=0) when the recirculation zone is shorter. In Figure 18, the values of the peak-pressure radiated to the wall, $p_a(\delta)$, give an estimation of the intensity of the collapses and the risks of damage on the obstacle surface. They are stronger in the plane with a longer recirculation zone. Indeed the growth phase is longer in this case and the following collapse yields a larger peak pressure.

6. Conclusion

The Rayleigh-Plesset equation was implemented and solved with an embedded Rosebrock method. The importance of the critical equilibrium state for modelling bubble dynamics was illustrated with examples of bubbles growing without limit. The accuracy of the method requires a correct equilibrium state (R_0, p_0) of the bubble. Therefore a method for estimating the equilibrium radius R_0 at release location was derived and validated in order to avoid bubble size oscillations at the beginning of the computations. The performance of the present model was assessed by considering results from previous studies. The agreement between numerical and experimental data depends on the set of parameters chosen to resolve the Rayleigh-Plesset equation. In particular the value of the liquid viscosity influences the bubble size at rebound R_{reb}. According to the classical approach used to estimate the intensity of the collapse, the dissipated energy depends on the value R_{reb}. While this approach is valid with experimental data, it is not reliable in the context of numerical calculations because the results obtained depend on the model parameters.

The bubble dynamics model was included in an algorithm modelling the bubble transport in the flow using a discrete bubble model. A study is performed to analyse the effects of the force F_{vol} which accounts for the volume variation of the bubbles in the transport equation. This force yields unphysical deviations of the trajectory of collapsing bubbles. Therefore its contribution should not be included in the computations of the transport of collapsing bubbles.

The overall model is implemented in OpenFOAM in order to simulate the
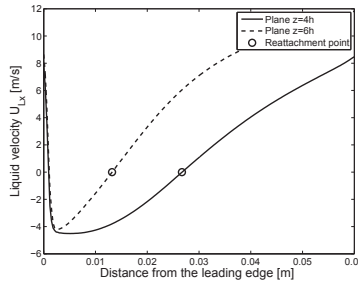
(a)
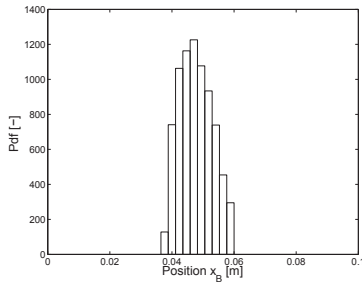
(b)
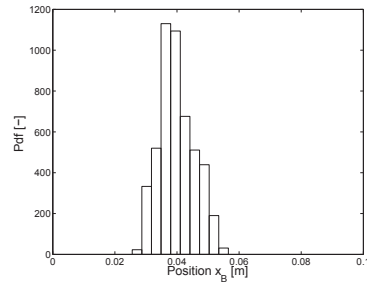
(c)

Figure 17: a) x-component of the liquid velocity $\mathbf{U}_L$ sampled above the obstacle (y=6.5 mm) and length of the recirculation zone in two different planes. (b) and (c) Pdf of the position at collapse vs distance from the leading edge in the plane (a) z=4h and (b) z=6h.
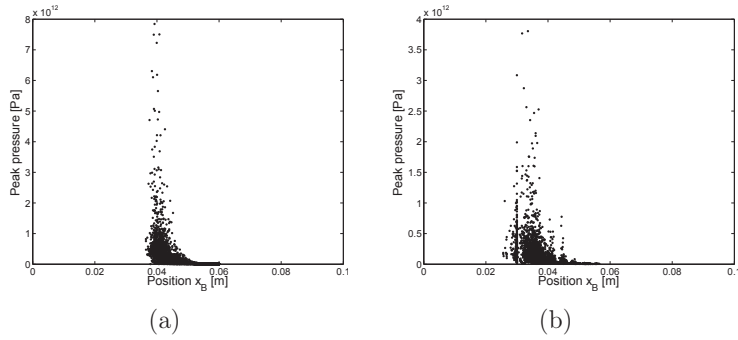
Figure 18: Peak of pressure radiated on the wall due to the shock wave in the plane (a) z=4h and (b) z=6h.

trajectory of small bubbles and capture their expansion and collapse near the surfaces. This model can be applied to a more complex geometry such as a turbine and provide information about the location of expected erosion damages due to the successive bubble collapses.

Acknowledgements

References

Alehossein, H., Qin, Z., 2007. Numerical analysis of rayleigh-plesset equation for cavitating water jets. Int. J. Numer. Methods Eng. 72, 780–807.

39

Auton, T., 1987. The lift force on a spherical body in a rotational flow. J. Fluid Mech. 183, 199–218.

Benjamin, T. B., Ellis, A., 1996. The collapse of cavitation bubbles and the pressures thereby produced against solid boundaries. Philos. Trans. R. Soc. Lond. A 260, 221–240.

Best, J., 2002. The effect of non-spherical collapse on determination of explosion bubble parameters. Technical report, DSTO-RR-0238; DODA-AR-012-368, Maritime Operation Div.

Blake, J., Gibson, D., 1987. Cavitation bubbles near boundaries. Annu. Rev. Fluid Mech. 19, 99–123.

Boussinesq, J., 1903. Théorie analytique de la chaleur. Gauthier-Villars Paris 2.

Brujan, E., 2004. The role of cavitation microjets in the therapeutic applications of ultrasound. Ultrasound Med. Biol. 30, 381–387.

Brujan, E., Ikeda, T., Matsumoto, Y., 2005. Jet formation and shock wave emission during collapse of ultrasound-induced cavitation bubbles and their role in the therapeutic applications of high-intensity focused ultrasound. Phys. Med. Biol. 50, 4797–4809.

Chahine, G., Shen, Y., 1986. Bubble dynamics and cavitation inception in cavitation susceptibility meters. J. Fluids Eng. 108, 444–452.

Cole, R., 1948. Underwater explosions. Princeton Univ. Press, 8.

Franc, J.-P., 2006. Physics and control of cavitation. Design and Analysis of High Speed Pumps 2, 1–36.

Giannadakis, E., Gavaises, M., Arcoumanis, C., 2008. Modelling of cavitation in diesel injector nozzles. J. Fluids Mech. 616, 153–193.

Gosman, A., Ioannides, E., 1983. Aspects of computer simulation of liquid-fueled combustors. J. Energy 7, 482–490.

Haberman, W., Morton, R., 1953. An experimental investigation of the drag and shape of air bubbles rising in various liquids. David Taylor Model Basin, Rep. 802.

Hsiao, C.-T., Chahine, G., Liu, H.-L., 2005. Scaling a tip vortex with a bubble dynamics model accounting for nuclei size distribution. J. Fluids Eng. 127, 55–65.

Johnson, V. E., Hsieh, T., 1966. The influence of the trajectories of gas nuclei on cavitation inception in a line vortex flow. Sixth Symposium on Naval Hydrodynamics, 163–179.

Kaps, P., Rentrop, P., 1979. Generalized runge-kutta methods of order four with stepsize control for stiff ordinary differential equations. Numerische Mathematik 33, 55–68.

Kasturiarachi, A., 2002. Leap-frogging newton's method. Int. J. Math. Ed. Sci. Tech. 33.

Kling, C., Hammit, F., 1972. A photographic study of spark-induced cavitation bubble collapse. J. Basic Eng. 94, 825–833.

Lauterborn, W., Kurz, T., Mettin, R., Ohl, C. D., 2007. Experimental and theoretical bubble dynamics. Advances in Chemical Physics 110.

Maxey, M., Riley, J., 1983. Equation of motion for a small rigid sphere in a nonuniform flow. Phys. Fluids 26, 883–889.

Mettin, R., Akhatov, I., Parlitz, U., Ohl, C., Lauterborn, W., 1997. Bjerknes forces between small cavitation bubbles in a strong acoustic field. Phys. Rev. 56.

Moss, W., Levantin, J., Szeri, A., 2000. A new damping mechanism in strongly collapsing bubbles. Proc. Math. Phys. Eng. Sci. 456, 2983–2994.

Ohl, C. D., Kurz, T., Geisler, R., Lindau, O., Lauterborn, W., 1999. Bubble dynamics, shock waves and sonoluminescence. Philos. Trans. R. Soc. Lond. A 357, 269–294.

Philipp, A., Lauterborn, W., 1998. Cavitation erosion by single laser-produced bubbles. J. Fluid Mech. 361, 75–116.

Plesset, M., Chapman, R., 1971. Collapse of an initially spherical vapour cavity in the neighbourhood of a solid boundary. J. Fluid Mech. 47, 283–290.

Plesset, M., Prosperetti, A., 1977. Bubble dynamics and cavitation. Annu. Rev. Fluid. Mech. 9, 145–185.

Podvin, B., Khoja, S., Moraga, F., Attinger, D., 2008. Model and experimental visualizations of the interaction of a bubble with an inclined wall. Chem. Eng. Sci. 63, 1914–1928.

Popinet, S., Zaleski, S., 2002. Bubble collapse near a solid boundary: A numerical study of the influence of viscosity. J. Fluid Mech. 464, 137–163.

Press, W., Teukolsky, S., Vetterling, W., B.P., F., 1992. Numerical recipes in c. Cambridge University.

Rayleigh, L., 1917. On the pressure developed in a liquid during the collapse of a spherical void. Phylos. Mag. 34.

Schiller, L., Nauman, A., 1935. A drag coefficient correlation. Ver. Deut. Ing. 77, 318–320.

Shampine, L., 1982. Implementation of rosenbrock methods. ACM Trans. on Math. Softw. 8, 93–113.

Shams, E., Apte, S., 2009. Larde eddy simulation of cavitation inception in a high speed flow over an open cavity. Seventh International Symposium on Cavitation.

Shima, A., 1997. Studies on bubble dynamics. Shock Waves 7, 33–42.

Stokes, G., 1850. On the effect of the internal friction of fluids on the motion of pendulums. Trans. Camb. Phylos. Soc. 9.

Tomita, Y., Shima, A., 1986. Mechanisms of impulsive pressure generation and damage pit formation by bubble collapse. J. Fluid. Mech. 169, 535–564.

Vogel, A., Lauterborn, W., 1988. Acoustic transient generation by laser produced cavitation bubbles near solid boundaries. J. Acoust. Soc. Am. 84.

Zenit, R., Legendre, D., 2009. The coefficient of restitution for air bubbles colliding against walls in viscous liquids. Phys. Fluids 21.

A. The transport equations

We search a numerical solution of the transport equations which are a system of 6 first order ODEs.

$$\frac{d\mathbf{x}_B}{dt} = \mathbf{U}_B$$

$$\frac{d\mathbf{U}_B}{dt} = \frac{1}{\frac{\rho_B}{\rho_L} + \frac{1}{2}} \left[\frac{1}{2} \frac{D\mathbf{U}}{Dt} - \frac{1}{\rho_L} \nabla p_L + (\frac{\rho_B}{\rho_L} - 1)\mathbf{g} \right.$$

$$\left. + \left(\frac{3C_{drag}|\mathbf{U}_L - \mathbf{U}_B|}{8R} + \frac{3\dot{R}}{2R} \right) (\mathbf{U}_L - \mathbf{U}_B) + C_{lift}(\mathbf{U}_L - \mathbf{U}_B) \times \omega_L \right]$$

These equations are written in matrix form as

$$[X]' = [F]$$

$$X = \begin{bmatrix} x_1 \\ x_2 \\ x_3 \\ x_4 \\ x_5 \\ x_6 \end{bmatrix} = \begin{bmatrix} x_B \\ y_B \\ z_B \\ u_B \\ v_B \\ w_B \end{bmatrix} \qquad F = \begin{bmatrix} f_1 \\ f_2 \\ f_3 \\ f_4 \\ f_5 \\ f_6 \end{bmatrix} = \begin{bmatrix} u_B \\ v_B \\ w_B \\ f_4(u_B, v_B, w_B) \\ f_5(u_B, v_B, w_B) \\ f_6(u_B, v_B, w_B) \end{bmatrix}$$

where

$$f_4 = \frac{1}{\frac{\rho_B}{\rho_L} + \frac{1}{2}} \left[\frac{1}{2} \frac{Du_L}{Dt} - \frac{1}{\rho_L} \frac{\partial p}{\partial x} + \left(\frac{3C_{drag}|\mathbf{U}_L - \mathbf{U}_B|}{8R} + \frac{3\dot{R}}{2R} \right) (u_L - u_B) \right.$$

$$\left. + C_{lift} \left((v_L - v_B)\frac{\partial w_L}{\partial y} - (w_L - w_B)\frac{\partial v_L}{\partial z} \right) \right]$$

$$f_5 = \frac{1}{\frac{\rho_B}{\rho_L} + \frac{1}{2}} \left[\frac{1}{2} \frac{Dv_L}{Dt} - \frac{1}{\rho_L} \frac{\partial p}{\partial y} + \left(\frac{3C_{drag}|\mathbf{U}_L - \mathbf{U}_B|}{8R} + \frac{3\dot{R}}{2R} \right) (v_L - v_B) \right.$$

$$\left. + C_{lift} \left((w_L - w_B)\frac{\partial u_L}{\partial z} - (u_L - u_B)\frac{\partial w_L}{\partial x} \right) \right]$$

$$f_6 = \frac{1}{\frac{\rho_B}{\rho_L} + \frac{1}{2}} \left[\frac{1}{2} \frac{Du_L}{Dt} - \frac{1}{\rho_L} \frac{\partial p}{\partial z} + \left(\frac{3C_{drag}|\mathbf{U}_L - \mathbf{U}_B|}{8R} + \frac{3\dot{R}}{2R} \right) (w_L - w_B) \right.$$

$$\left. + C_{lift} \left((u_L - u_B)\frac{\partial v_L}{\partial x} - (v_L - v_B)\frac{\partial u_L}{\partial y} \right) \right]$$

The Jacobian matrix is

$$
J = \frac{\partial[F]}{\partial[X]} =
\begin{bmatrix}
0 & 0 & 0 & 1 & 0 & 0 \\
0 & 0 & 0 & 0 & 1 & 0 \\
0 & 0 & 0 & 0 & 0 & 1 \\
0 & 0 & 0 & \frac{\partial f_4}{\partial x_4} & \frac{\partial f_4}{\partial x_5} & \frac{\partial f_4}{\partial x_6} \\
0 & 0 & 0 & \frac{\partial f_5}{\partial x_4} & \frac{\partial f_5}{\partial x_5} & \frac{\partial f_5}{\partial x_6} \\
0 & 0 & 0 & \frac{\partial f_6}{\partial x} & \frac{\partial f_6}{\partial x_5} & \frac{\partial f_6}{\partial x_6}
\end{bmatrix} .
$$

and the components are

$$
\frac{\partial f_4}{\partial x_4} = \frac{-1}{\frac{\rho_B}{\rho_L} + \frac{1}{2}} \left[\frac{3C_{drag}|\mathbf{U}_L - \mathbf{U}_B|}{8R} + \frac{3\dot{R}}{2R} \right]
$$

$$
\frac{\partial f_4}{\partial x_5} = \frac{-1}{\frac{\rho_B}{\rho_L} + \frac{1}{2}} \left[C_{lift} \frac{\partial w_L}{\partial y} \right]
$$

$$
\frac{\partial f_4}{\partial x_6} = \frac{1}{\frac{\rho_B}{\rho_L} + \frac{1}{2}} \left[C_{lift} \frac{\partial v_L}{\partial z} \right]
$$

$$
\frac{\partial f_5}{\partial x_4} = \frac{1}{\frac{\rho_B}{\rho_L} + \frac{1}{2}} \left[C_{lift} \frac{\partial w_L}{\partial x} \right]
$$

$$
\frac{\partial f_5}{\partial x_5} = \frac{-1}{\frac{\rho_B}{\rho_L} + \frac{1}{2}} \left[\frac{3C_{drag}|\mathbf{U}_L - \mathbf{U}_B|}{8R} + \frac{3\dot{R}}{2R} \right]
$$

$$
\frac{\partial f_5}{\partial x_6} = \frac{-1}{\frac{\rho_B}{\rho_L} + \frac{1}{2}} \left[C_{lift} \frac{\partial u_L}{\partial z} \right]
$$

$$
\frac{\partial f_6}{\partial x_1} = \frac{-1}{\frac{\rho_B}{\rho_L} + \frac{1}{2}} \left[C_{lift} \frac{\partial v_L}{\partial x} \right]
$$

$$
\frac{\partial f_6}{\partial x_2} = \frac{1}{\frac{\rho_B}{\rho_L} + \frac{1}{2}} \left[C_{lift} \frac{\partial u_L}{\partial y} \right]
$$

$$
\frac{\partial f_6}{\partial x_3} = \frac{-1}{\frac{\rho_B}{\rho_L} + \frac{1}{2}} \left[\frac{3C_{drag}|\mathbf{U}_L - \mathbf{U}_B|}{8R} + \frac{3\dot{R}}{2R} \right]
$$

44

Mass transfer cavitation model with variable density of nuclei

A. Vallier[*], H. Nilsson[†] and J. Revstedt[*]

[*] Division of Fluid Mechanics Dept. Energy Sciences, Lund University, SE-22100 Lund, Sweden

[†] Applied Mechanics, Fluid Dynamics, Chalmers University of Technology, SE-412 96 Gothenburg, Sweden

Aurelia.Vallier@energy.lth.se, hakan.nilsson@chalmers.se and Johan.Revstedt@energy.lth.se

Keywords: Cavitation, Sauer's model, Variable nuclei density, Lagrangian Particle Tracking

Abstract

The performance of the mass transfer cavitation model of Sauer is investigated using a varying nuclei concentration. The Sauer model assumes a uniform nuclei distribution despite measurement of the non-homogeneous nucleus population. Here the nuclei density is studied and a non-homogeneous nuclei distribution in a modified Sauer model is implemented. It is used to study how the increased cavitation nuclei density in regions of low pressure affects the inception of cavitation. The interface between the water and the water vapor is tracked using a volume of fluid method and vaporization and condensation are described by the modified Sauer's mass transfer model. The nuclei in the liquid phase are modeled with a Lagrangian Particle Tracking method. The LPT computations yield to a non uniform nuclei distribution which consists of nuclei accumulation close to the leading edge and no nuclei on average in the boundary layer of the hydrofoil. The sensitivity of the modified Sauer model to nuclei distribution is proven. The shape of the sheet cavity and the volume of vapour are affected by the nuclei content.

Nomenclature

Roman symbols

g   gravitational constant (ms^{-1})
p   pressure (Nm^{-2})
U   velocity (ms^{-1})
D   diameter (m)
R   radius (m)
c_0 chord length (m)
k   turbulent kinetic energy $(\mathrm{m}^2\mathrm{s}^{-2})$

Greek symbols

α vapor volume fraction
ρ density (kgm^{-3})
μ viscosity $(kgm^{-1}s^{-1})$
τ relaxation time (s)
ϵ turbulence energy dissipation rate $(\mathrm{m}^2\mathrm{s}^{-3})$

Subscripts

P particle
v vapor
l liquid

Introduction

Recently, many mass transfer cavitation models have been introduced in the literature and general-purpose CFD codes in order to fully describe the observed phenomena on cavitating hydrofoils. The inception cavitation number is supposed to be given by the minimum value of the pressure coefficient. This law is barely suitable in the case of attached cavitation on a hydrofoil because viscosity, turbulence and water quality have a major influence on cavitation inception (Brennen (1995)). In particular, cavitation inception occurs at different pressure depending on the number of cavitation nuclei. Therefore, taking into account the non-homogeneous nuclei content of the water will improve the accuracy of the numerical simulations. Sauer (2000) included the nuclei density parameter n_0 in their cavitation model, specified as a constant . This assumption is not in accordance with experiments or the numerical results obtained by Huuva et al. (2007), where it is shown that the nuclei accumulate in certain regions close to the hydrofoil. Mass transfer models give very good predictions of the mechanism of the cavitation inception and development for cases of cavitating hydrofoils (Coutier-Delgosha et al. (2007)). These models successfully represent the attached sheet cavity, the re-entrant jet, the

break-off of the sheet, and the shedding of the break-off process. All these features agree with experimental observations. However, the models fail to resolve the transition between the attached sheet cavity and the cloud of vapor. In experiments, the transition forms a cloud of small vapor bubbles, while the numerical methods preserve a large coherent vapor region that is advected with the surrounding flow. The models cannot further handle the collapsing process of the small bubbles and the related erosive and acoustic processes. Indeed this important feature should at some point be included in the prediction as it is the main cause of erosion damage. The implosion of the bubble cloud when it reached a region of higher pressure generates pressure waves that influence the collapse of the surrounding bubbles, causing a chain reaction that amplifies the erosive process. As the model does not accurately predict regions containing a low vapor concentration, we study the relevance of the hypothesis made to simplify the model, i.e. the assumption of constant nuclei concentration. It is not obvious that the nuclei concentration is homogeneous in real application. Therefore it is of interest to investigate how a inhomogeneous distribution affects the inception and development of attached sheet cavities.

The Sauer cavitation mass transfer model is introduced with the nuclei density n_0, taking into account the water quality. Then the LPT method described is used to compute the cavitation nuclei distribution. Finally we present the results obtained for the LPT nuclei distribution and for the modified Sauer model where non homogeneity is included.

Geometry

The simulations were performed for 2D and 3D flows past a NACA0015 hydrofoil. Figure 1 illustrates the 125*270 C-grid used for the 2D computations. The hydrofoil has a chord length c_0=0.15m and is positioned at $4.5c_0$ from the inlet and $9c_0$ from the outlet. The height of the computational domain is $9c_0$. The angle of attack is 8 degrees. The grid points are clustered to the hydrofoil surface such that the first cell center near the hydrofoil surface starts at $\Delta y/c_0 \sim 0.1/\sqrt{Re} = 1.10^{-4}$ with an increase of 5% per layer. Hence, the first node away from the wall is on average positioned at $y^+ = 3$. In the case of the 3D simulation, 50 grid points are equally distributed in spanwise direction, with a total spanwise thickness of $1c_0$. The Reynolds number based on c_0 and the uniform inlet velocity 8m/s is Re=$1.2 \cdot 10^6$. The cavitation number σ is 1.2.
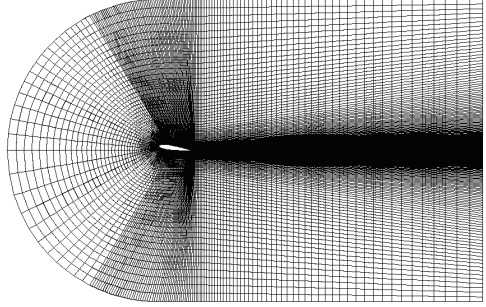
Figure 1: Computational grid for the NACA0015 airfoil

Sauer model

The Sauer model (Sauer (2000)) is a mass transfer model using the volume of fluid (VOF) approach. The fluid density and viscosity are scaled by the vapor volume fraction α

$$\rho = \alpha \rho_v + (1 - \alpha)\rho_l \qquad (1)$$

$$\mu = \alpha \mu_v + (1 - \alpha)\mu_l \qquad (2)$$

The transport equation for the vapor volume fraction reads

$$\frac{\partial \alpha}{\partial t} + \nabla \cdot (\alpha \mathbf{U}) = S_\alpha \qquad (3)$$

where the source term $S_\alpha = -\frac{\dot{m}}{\rho_v}$ accounts for the destruction and production of vapor. One can also derive a corresponding transport equation for the liquid volume fraction γ (where $\alpha + \gamma = 1$). The source term is then $S_\gamma = \frac{\dot{m}}{\rho_l}$ which accounts for the destruction and production of liquid. Summing the two transport equations results in the non divergence free continuity equation:

$$\nabla \cdot \mathbf{U} = (\frac{1}{\rho_l} - \frac{1}{\rho_l})\dot{m}$$

In order to derive the mass transfer rate, $\dot{m}$, the Sauer model states that the vapor volume fraction corresponds to a density n_0 of nuclei of radius R. Furthermore the dynamics of each bubble is governed by a simplified Rayleigh-Plesset equation. Hence the vapor volume fraction and the nuclei growth rate are written as

$$\alpha = \frac{\frac{4}{3}\pi R^3 n_0}{1 + \frac{4}{3}\pi R^3 n_0} \qquad (4)$$

$$\dot{R} = \sqrt{\frac{2}{3}\frac{|p(R) - p_\infty|}{\rho_l}}. \qquad (5)$$

The mass transfer rate $\dot{m}$ is then derived (see Sauer (2000)) as

$$\dot{m} = -\rho_v \frac{3\alpha}{R} sign(p_v - p)\sqrt{\frac{2}{3}\frac{|p_v - p|}{\rho_l}} \qquad (6)$$

Finally, the continuity and vapor transport equations are solved together with the momentum equation:

$$\rho\frac{\partial \mathbf{U}}{\partial t} + \rho(\mathbf{U} \cdot \nabla\mathbf{U}) = -\nabla p + \mu\nabla^2\mathbf{U} + \rho g \qquad (7)$$

Nuclei distribution

Lagrangian Particle Tracking

Lagrangian particle tracking (LPT) is a method to track individual particles (or bubbles) in a fluid flow. A particle P is defined by the position of its center, $\mathbf{x_P}$, its diameter, D_P, its velocity, $\mathbf{U_P}$ and its density, ρ_P.

The fluid phase is governed by the incompressible Navier-Stokes equations

$$\nabla \cdot \mathbf{U} = 0$$

$$\rho\frac{\partial \mathbf{U}}{\partial t} + \rho(\mathbf{U} \cdot \nabla\mathbf{U}) = -\nabla p + \mu\nabla^2\mathbf{U} + \rho g - \mathbf{S_P} \quad (8)$$

The additional source term in the momentum equation (8) is due to the influence of the particles on the flow. Here we consider the case of a dilute suspension ($\frac{\mathbf{x_{P_i}} - \mathbf{x_{P_j}}}{D_P} > 10$) with a volume fraction of particles lower than 10^{-6}. Hence the particles' effects on the flow and turbulence are negligible (see Elghobashi (1994)). This is usually denoted one-way coupling, i.e. the flow affects the particles but the particles don't affect the flow. Therefore the additional source term $\mathbf{S_P}$ in the momentum equation is neglected. As a consequence of the very low volume fraction of particles, inter-particle collisions are also neglected.

In a Lagrangian frame, each particle position vector $\mathbf{x_P}$ is calculated from the equation

$$\frac{d\mathbf{x_P}}{dt} = \mathbf{U_P} \qquad (9)$$

and the motion of each particle is governed by Newton's second law:

$$m_p\frac{d\mathbf{U_P}}{dt} = \sum \mathbf{F}, \qquad (10)$$

where the mass of each particle is $m_P = \frac{1}{6}\rho_P\pi D_P^3$.

In dilute flow, the dominant forces acting on the small particle is the drag from the fluid phase and the gravitational force:

$$\sum \mathbf{F} = \mathbf{F_D} + m_p\mathbf{g} \qquad (11)$$

The particle Reynolds number is defined as

$$\mathrm{Re}_P = \frac{\rho_f D_p|\mathbf{U} - \mathbf{U_P}|}{\mu_f} \qquad (12)$$

and the drag force can be expressed as

$$\mathbf{F_D} = -m_p\frac{\mathbf{U_P} - \mathbf{U}}{\tau_P} \qquad (13)$$

The relaxation time τ_p of the particles is the time it takes for a particle to respond to changes in the local flow velocity

$$\tau_p = \frac{4}{3}\frac{\rho_p D_p}{\rho_f C_D|\mathbf{U} - \mathbf{U_P}|} \qquad (14)$$

where the standard definition of the drag coefficient C_D for a spherical particle is given by Schiller and Naumann as

$$C_D = \begin{cases} \frac{24}{Re_p} & \text{if } \mathrm{Re}_p \leq 0.1 \\ \frac{24}{Re_p}(1 + \frac{1}{6}Re_p^{2/3}) & \text{if } 0.1 \leq Re_p \leq 1000 \\ 0.44 & \text{if } \mathrm{Re}_p > 1000 \end{cases} \qquad (15)$$

Since the fluid velocity $\mathbf{U}$, calculated in the Eulerian reference frame, is needed for the calculation of the drag force in the Lagrangian frame, it has to be interpolated to the position of the particle from the neighboring cells. The velocity at the particle position is denoted $\mathbf{U_{@P}}$.

Furthermore, each Eulerian time step is divided into a set of Lagrangian time steps that is specific to each particle. A Lagrangian time step is defined as the time it takes for a particle to leave the cell that it was occupying.

The velocity and position of a particle at the n-th Lagrangian time step Δt_n within an eulerian time step is evaluated as

$$\mathbf{U_P^{t+\sum_{i=1}^{n}\Delta t_i}} = \frac{\mathbf{U_P^{t+\sum_{i=1}^{n-1}\Delta t_i}} + \mathbf{U_{@P}^t}\frac{\Delta t_n}{\tau_p} + \mathbf{g}\Delta t_n}{1 + \frac{\Delta t_n}{\tau_p}} \qquad (16)$$

$$\mathbf{x_P^{t+\sum_{i=1}^{n}\Delta t_i}} = \mathbf{x_P^{t+\sum_{i=1}^{n-1}\Delta t_i}} + \mathbf{U_P^{t+\sum_{i=1}^{n-1}\Delta t_i}}\Delta t_n \qquad (17)$$

The collision of a particle with the wall is assumed to be inelastic. Hence, the velocities of the particle P before and after collision are written as

$$\mathbf{U}_P = U_P^n\mathbf{n} + U_P^t\mathbf{t} \qquad (18)$$

$$\mathbf{U}_P^{'} = U_P^{n'}\mathbf{n} + U_P^{t'}\mathbf{t} \qquad (19)$$

The unit vectors $\mathbf{n}$ and $\mathbf{t}$ are the normal and tangential to the wall, respectively. The normal and tangential components of the particle velocity after a collision with the wall are evaluated as

$$U_P^{n'} = -\epsilon_w U_P^n \qquad (20)$$

3

$$U_P^{t'} = (1 - \mu_w)U_P^t \qquad (21)$$

where $\epsilon_w \in [0, 1]$ and $\mu_w \in [0, 1]$) are the coefficient of restitution and friction of the wall.

Random Walk

In reality, small particles have a short relaxation time and respond quickly to the flow fluctuations. Turbulence diverts the particles from their trajectory and small particles are trapped in eddies for a certain period of time. Not accounting for this leads to that the particles will follow the stream lines of the mean flow. Here we use a random walk model (Gosman & Ioannides (1983)) to include the effect of turbulent dispersion of the particles, i.e. eddies are created randomly and affect the particle trajectory. In practice, a local fluctuating component is added to the fluid velocity at the position of the particle, i.e. $\mathbf{U}_{@P}$ becomes $\tilde{\mathbf{U}}_{@P} = \mathbf{U}_{@P} + \mathbf{U}_{@P}^{fluct}$. The local fluctuating velocity can be estimated by

$$\mathbf{U}_{@P}^{fluct} = \psi \sqrt{\frac{2}{3}k} \qquad (22)$$

where ψ is a random number generated from a Gaussian distribution of zero mean and variance 1 ($\psi \in N(0, 1)$) and $\sqrt{\frac{2}{3}k}$ is the local RMS fluid velocity fluctuations for isotropic turbulence. The eddy life time (t_e) and the time needed by the particle to traverse the eddy (transit time t_{tr}) are calculated as

$$t_e = \frac{C_\mu^{0.63} \frac{k^{1.5}}{\epsilon}}{|\mathbf{U}_{@P}^{fluct}|} \qquad (23)$$

$$t_{tr} = -\tau_P ln(1 - \frac{l_e}{\tau_P |\tilde{\mathbf{U}}_{@P} - \mathbf{U}_P|}). \qquad (24)$$

The random walk algorithm consists of evaluating $\mathbf{U}_{@P}^{fluct}$ according to equation (22) and a random number ψ, calculating the characteristics times t_e and t_{tr} and keeping $\mathbf{U}_{@P}^{fluct}$ constant during the interaction time $t_{int} = min(t_e, t_{tr})$.

Results

Nuclei density sensitivity to particle properties

Several cases (listed in Table 1) have been studied in order to investigate the sensitivity of the solution to particle diameter and particle density. Also, all these cases have been simulated both with and without the random walk model. Furthermore one 3D case was simulated with LES to see how the turbulence affects the particles distribution.
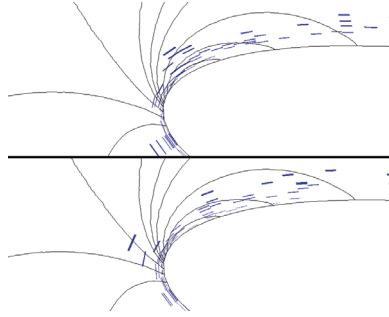

Figure 2: Instantaneous distribution of cells with a large nuclei density for cases $LPT6$ (top) and $LPT6_{RW}$ (bottom)
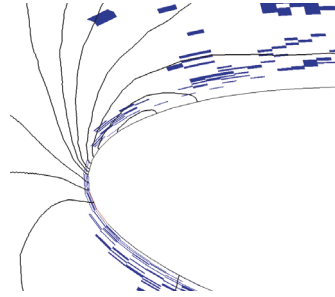

Figure 3: Instantaneous distribution of cells with a large nuclei density for case $LPT6_{LES}$, in the centerplane
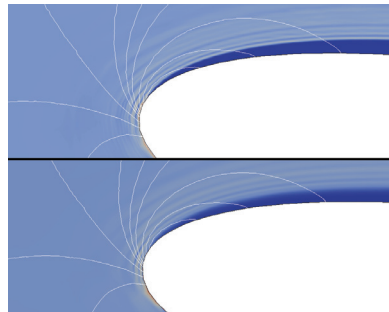

Figure 4: Average nuclei distribution for cases $LPT6$ and 6_{RW}

Table 1: Summary of the LPT cases.

ρ_P	D_P	2D RANS	2D RANS + RW	3D LES
1000	1	$LPT1$	$LPT1_{RW}$	
1000	10	$LPT2$	$LPT2_{RW}$	
1000	20	$LPT3$	$LPT3_{RW}$	
1000	30	$LPT4$	$LPT4_{RW}$	
1000	40	$LPT5$	$LPT5_{RW}$	
1000	50	$LPT6$	$LPT6_{RW}$	$LPT6_{LES}$
100	50	$LPT7$	$LPT7_{RW}$	
10	50	$LPT8$	$LPT8_{RW}$	
1	50	$LPT9$	$LPT9_{RW}$	

500 particles are injected per time step at a distance $1.5c_0$ in front of the hydrofoil.

Figures 2 and 3 highlight the cells which contain the largest number of nuclei for the RANS and LES computations. Two features are observed. First, a large number of nuclei are present at the leading edge. Obviously the density is highest at the stagnation point (colored in red) because the nuclei rebound against the wall and reside a longer time in this region of low velocity. Second, the presence of cells with a high nuclei content in the region of low pressure should be investigated. In this region the velocity is high and the residence time of a nuclei is therefore very short. From one instantaneous picture to another, the nuclei distribution is completely different. Thus we calculate an average of the positions occupied by the nuclei during their trajectory. Figure 4 shows the results for case $LPT6$ and $LPT6_{RW}$. The average nuclei distribution confirms the accumulation of nuclei at the stagnation point (colored in red) . A large number of nuclei are also observed in a part of the low pressure region near the leading edge. However the results show that the nuclei are not present on average in a layer close to the hydrofoil.

In order to compare the influence of the size and the density, as well as the turbulence modeling, the averaged nuclei distribution has been sampled on the vertical line which goes through the lowest pressure region (line 2 in Figure 5). The average number of nuclei is sampled in Figure 6, 7 and 8. It shows that the dark blue layer in Figure 4 corresponds to a nuclei content lower than the far field density (which is 2.1e8). This layer is thicker (around 0.5 mm instead of 0.1 mm) for nuclei larger than 10 μm. For large nuclei, the distribution is very dense on the surface, exactly in the low pressure cells. For small nuclei, the high density is located from 0.1 to 0.3 mm away from the surface, and the peak is much lower. Particle with lower density behave like particles with diameter smaller than 20 μm (Figure 7).

The random walk model has an impact on the nuclei

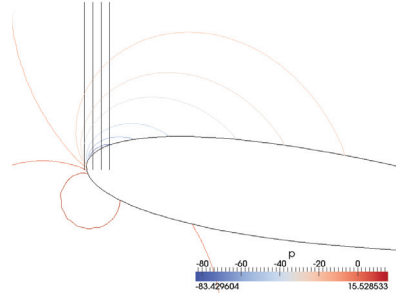**Figure 5:** Contour of pressure (2D, RANS). Sampling lines where the average nuclei distribution is investigated.
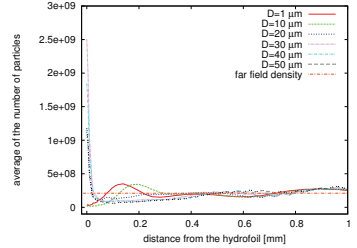

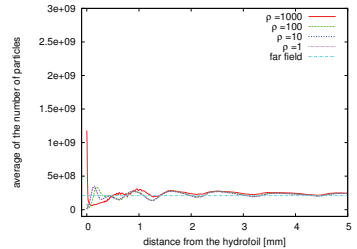**Figure 6:** Sensitivity to particle size, sampling line 2

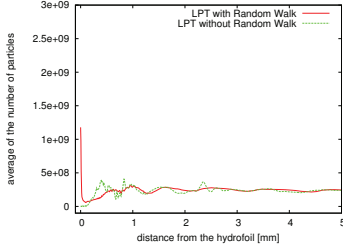**Figure 7:** Sensitivity to particle density, sampling line 2

5

Figure 8: Sensitivity to Random Walk model, sampling line 2

distribution, as shown in Figure 8. When turbulent dispersion is accounted for, the nuclei distribution is very dense on the surface of the hydrofoil while there is no nuclei on the first 0.2 mm near the surface without turbulent dispersion. Furthermore the oscillations away from the surface are damped.

Effect of inhomogeneous nuclei distribution

The Sauer model assumes a homogeneous nuclei distribution, and a value of 10^8 is generally used. Here the performance of the model is investigated using a varying nuclei concentration. Using the nuclei distributions obtained from the simulations presented in the previous section in the modified Sauer model did not yield any sheet cavitation. Instead, the cavity appeared somewhat above the hydrofoil and was not attached. Indeed the vapor production started where both crucial parameters existed, i.e. a low pressure and a high concentration of nuclei. This behavior is due to the lack of nuclei in the boundary layer discussed in the results of the LPT simulations. However, it has been shown experimentally that cavitation starts at the surface. This implies that the transported nuclei (called free stream nuclei) don't have as much importance as the surface nuclei, at least for cavitation inception. Surface nuclei are generally small bubble of gas trapped in wall rugosity (Brennen (1995)). Therefore it has also been studied how the nuclei content in the boundary layer affect cavitation inception and development. In those studies it is assumed that the nuclei concentration N is high (N=10^8) in a layer attached to the surface and low (N=10^2 or 10^4) everywhere else. The thickness of the layer δ_N varies from 0.5, 1,2 and 4 mm. The cases are summarized in Table 2.

Figure 9 shows the total volume of vapor in the entire computational domain during the cavitating process. In cases 1 and 5, the layer is 0.5 mm thick. The nuclei content is too low to enable the cavity to grow sufficiently. The production of vapor is lower during cavitation in-

Table 2: Summary of the cases with a prescribed non uniform nuclei distribution. N is the nuclei concentration in the domain. δ_N is the thickness of the layer with high concentration of nuclei, i.e. where N=10^8.

	δ_N=0.5	δ_N=1	δ_N=2	δ_N=4
N=10^2	case 1	case 2	case 3	case 4
N=10^4	case 5	case 6	case 7	case 8
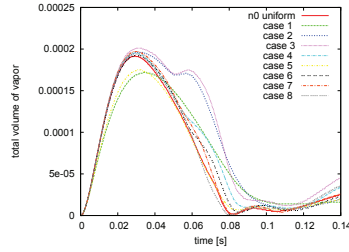
Figure 9: Total volume of vapor for cavitating flow with different nuclei distribution.

ception compare to the uniform case. In the other cases cavitation inception is similar to the case with uniform nuclei distribution. The same amount of vapor is created when the cavity grows. From t=0.02 s, the vapor production is slightly larger than in the uniform case. The cavity is broken by the reentrant jet, and from t=0.03 the vapor disappears at the same rate except for cases 2 and 3. For both cases, the volume of vapor decreases slower, grows again and then decreases as in the uniform case.

Figure 10 shows the cavitation process for the uniform case (left), case 7 (center) and case 3 (right). As mentioned, the inception is similar for all cases. The attached cavity has the same shape at t=0.02 s. Differences can be noticed from t=0.03 s, due to the re-entrant jet which has the same thickness as the layer of nuclei. For all the cases with $\delta_N \leq 2mm$, the cloud which is about to be detached is closer to the hydrofoil surface. Furthermore the re-entrant jet is faster. Thus it breaks the attached cavity at a position closer to the leading edge. As the point of detachment is closer to the leading edge, the length of the attached cavity is shorter and the cloud is more stretched. With a non-uniform nuclei distribution, the attached cavity is linked to the cloud by a thin layer of vapor. This line of vapor is still present when the cloud shrinks (t=0.06). It generates a second smaller, fuzzier cloud for the cases with N=10^2. This is the reason why the total volume of vapor increases around t=0.06 s for these cases.

6
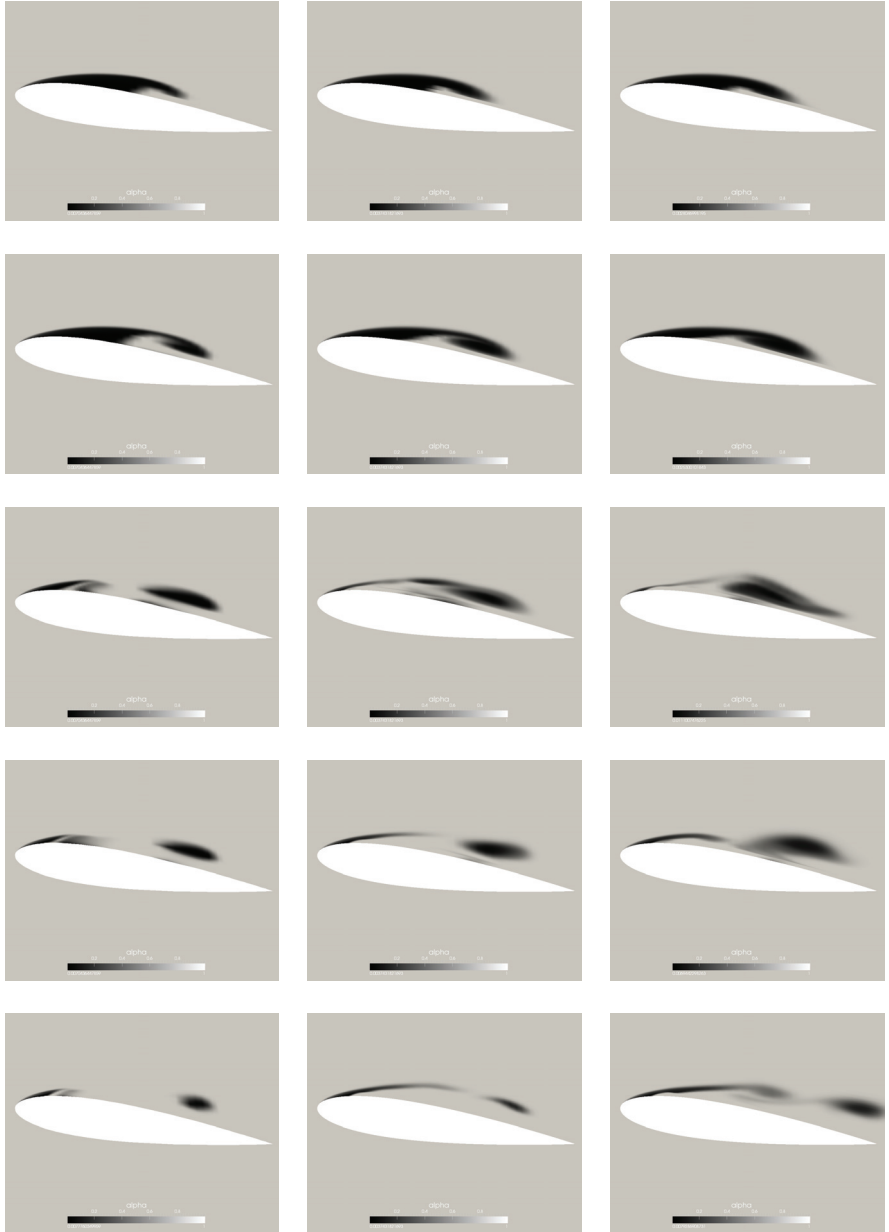
Figure 10: Vapor volume fraction α. First row t=0.02s, 2nd row t=0.03s, 3rd row t=0.05s, 4th row t=0.06s, 5th row t=0.07s. Left: N uniform, center: case 7 ($N = 10^4, \delta_N$=2 mm), right: case 3 ($N = 10^2, \delta_N$=2 mm)
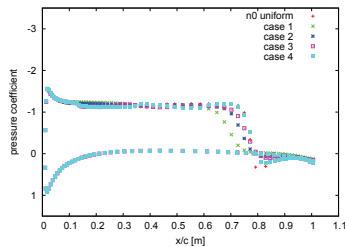
Figure 11: Pressure coefficient at t=0.03 s. Cases with N=10^2.

The differences between the curves of the pressure coefficient, shown in Figure 11, confirm that the non uniform cases have a shorter attached cavity already at t=0.03 as the the pressure increases at a position x/c_0 between=0.65 and 0.7 instead of 0.75 for the uniform case.

Conclusions

We studied the nuclei distribution over a NACA0015 hydrofoil. It was shown that the nuclei accumulate at the leading edge close to the low pressure region. However the nuclei were not present on average in the boundary layer. The Sauer model was modified to take into account this non uniform nuclei density and didn't yield to attached cavitation. It means that the transported nuclei influence is not as important as the one of the surface nuclei for cavitation inception. Then the performance of the modified Sauer model was investigated with a higher nuclei concentration near the surface. The attached cavity was shorter, the re-entrant jet was faster and thinner, and the cloud was stretched. A thin layer of vapor linked the attached cavity and the cloud of vapor. These features emphasize the importance of the nuclei distribution when modeling cavitation inception and developement.

Acknowledgements

References

Sauer J. and Schnerr G.H., Unsteady cavitating flow- A new cavitating model based on a modified front capturing method and bubble dynamics, Proceedings of 2000 ASME Fluid Engineering Summer Conference, Boston, MA, June 11-15, 2000

Huuva T., Cure A., Bark G. and Nilsson H., Computations of unsteady cavitating flow on wing profiles using a volume fraction method and mass transfer models. Proceedings of The 2nd IAHR International Meeting of the Workgroup on Cavitation and Dynamical Problems in Hydraulic Machinery and Systems, Scientific Bulletin of the "Polytechnica" University of Timisoara, Romania. Transactions on Mechanics, 52 (66) pp. 21-34, 2007

Coutier-Delgosha O., Deniset F., Astolfi J.A., Leroux J.-B., Numerical Prediction of cavitating Flw on a Two-Dimensional Symmetrical Hydrofoil and Comparison To Experiments, Journal of Fluids Engineering, march 2007, Vol. 129, 279-292.

Brennen C. E., Cavitation and Bubble Dynamics, New York Oxford University Press, 1995.

Clift R., Grace J.R and Weber M.E., Bubbles, Drops and Particles, Academic, New York,1978,

Gosman A.D. and Ioannides E., Aspects of computer simulation of liquid-fueled combustors, Journal of Energy,7, 482-490, 1983.

Elghobashi S., On predicting particle laden turbulent flows, Applied Scientific Research, 52, 309-329, 1994.

Numerical procedure for simulating the break-up of cavitation sheet

Aurélia Vallier[1], Johan Revstedt[1] and Håkan Nilsson[2]

[1]Fluid Mechanics/Energy Sciences, LTH Lund University
Lund, SE-221 00, Sweden, aurelia.vallier@energy.lth.se, johan.revstedt@enegy.lth.se
[2]Applied Mechanics/Fluid Dynamics, Chalmers University of Technology
Gothenburg, SE-412 96, Sweden, hani@chalmers.se

Abstract

Mass transfer cavitation models based on the Volume-Of-Fluid method (VOF) have a limitation of the resolution due to the grid size. Bubbles of the same size as the control volumes (or smaller) cannot be resolved. A new multi-scale approach is developed in the present work, which can model the presence of bubbles smaller than the grid size. The principle is to complement the VOF method with a two-way coupled Lagrangian particle tracking method (LPT). Using this approach for simulating cavitating hydrofoils lead to a better modelling of the mixture of vapor and liquid in the transition region between the attached cavity and the shedding cloud. The VOF-LPT coupling model is tested on simplified configurations for the breakup of an attached cavity. The results show that the model successfully captures the formation of small bubbles and gives a better description of the liquid/gas mixture.

Keywords: numerical simulation, VOF, LPT, multi-scale, cloud cavitation, OpenFOAM.

1. Introduction

In the last decades, numerous numerical cavitation models have been developed to describe the mechanisms of sheet and cloud cavitation on cavitating hydrofoils. A sheet cavity is a steady attached structure which covers a part of the hydrofoil. When the angle of attack is increased or the cavitation number decreased, cloud cavitation occurs which corresponds to foamy and unsteady structures. The cavity length oscillates because the rear part of the cloud is periodically detached from the cavity. The mass transfer models based on a Volume-Of-Fluid (VOF) formulation succeed to represent the attached sheet cavity, the re-entrant jet which breaks the sheet and the shedding of the cloud of vapour (Sauer and Schnerr [1], Kunz *et al.* [2]). However, these models give poor results regarding the break-up process and when bubble clouds are formed and advected.

The VOF method is designed to track the interface between two fluids. This method is therefore suitable for modeling large vapor structures, such as sheet cavitation. The drawback of this method is that it cannot describe structures that are smaller than the grid size. A higher resolution grid would be required to capture the small cavitation bubbles that are present in the case of cloud cavitation. This would increase excessively the computational cost. For modelling cloud cavitation, the appropriate method is to track individual bubbles in a Lagrangian frame. Furthermore, if the bubble dynamics is resolved by a Rayleigh-Plesset equation (Spång [3]), the collapse of individual bubbles which leads to the global collapse can be modeled. This would give a better understanding and a more accurate prediction of the collapse and its consequences such as pressure wave and pitting on the surface (Grekula [4]).

In order to improve the available cavitation models, the present work introduces a method that accounts for the entire spectrum of bubble sizes. The VOF and LPT methods are combined within a hybrid approach which uses the strength of the VOF method to model the large structures on a fine grid and the strength of the LPT method to model the small structures on a coarser grid.

2. Numerical approach

2.1 The VOF method with mass transfer cavitation model

The Volume-Of-Fluid method (VOF) is a numerical technique for tracking and locating the interface between two or more fluid phases (Hirt and Nichols [7]). It is useful for modeling large vapor structures and is therefore adopted for modeling sheet cavitation. VOF is used together with mass transfer cavitation models to take into account vaporization and condensation (Sauer and Schnerr [1], Kunz et al. [2]). In VOF, the liquid volume fraction α may vary from 0 to 1 within a computational cell. The interface exists in the cells with intermediate values. The mixture density ρ and viscosity μ are calculated using the volume fraction, as $\rho = \alpha \, \rho_l - (1-\alpha) \, \rho_g$ and $\mu = \alpha \, \mu_l - (1-\alpha) \, \mu_g$ where subscripts l and g stand for liquid and gas. The transport equation

for the volume fraction reads

$$\frac{\partial \alpha}{\partial t} + \nabla \cdot (\alpha \mathbf{U}) + \nabla \cdot (\alpha(1-\alpha)\mathbf{U_r}) = \mathbf{S}_\alpha , \qquad (1)$$

where $\mathbf{U}$ is the velocity of the mixture and $\mathbf{U_r}$ is the relative velocity between the two fluids. The third term in the l.h.s. of eq. (1) is an artificial compression term active only in the interface region. It was introduced by Rusche [8] to preserve the interface sharpness which is crucial in the VOF approach. In mass transfer cavitation models, the destruction and production of vapor is accounted for by the source term in eq. (1), as

$$\mathbf{S}_\alpha = \frac{-\dot{m}}{\rho_g} .$$

The mass transfer rate $\dot{m}$ between the liquid and the gas phase depends on the pressure, empirical parameters (Kunz *et al.* [2]) and on the nuclei number and size (Sauer and Schnerr [1]).
The mass and momentum equations read

$$\nabla \cdot \mathbf{U} = \left(\frac{1}{\rho_l} - \frac{1}{\rho_g} \right) \dot{m} , \qquad (2)$$

$$\frac{\partial \rho \mathbf{U}}{\partial t} + \nabla \cdot (\rho \mathbf{U} \otimes \mathbf{U}) = -\nabla p + \mu \nabla^2 \mathbf{U} - \mathbf{S}_{st} + \mathbf{S}_P , \qquad (3)$$

where p is the pressure of the mixture. The source term $\mathbf{S}_P$ is due to the influence on the flow of the bubbles tracked within the Lagrangian approach and is derived in the next section. The source term $\mathbf{S}_{st}$ models the effect of surface tension (Brackbill [9]), as
$$\mathbf{S}_{st} = \sigma_{st} \kappa \delta \, \mathbf{n} ,$$

where δ is the Dirac function which insures that the force is only applied at the interface, σ_{st} is the surface tension coefficient, $\mathbf{n}$
is the normal vector at the interface ($\mathbf{n} = \nabla \alpha / |\nabla \alpha|$) and κ is the curvature at the interface ($\kappa = \nabla \mathbf{n}$).

Instead of considering the interface as a sharp discontinuity, it is assumed to have a finite thickness which is a smooth transition from one fluid to the other. The dispersion of the surface tension across the transition region is obtained with the gradient of the volume fraction $\nabla \alpha$. Therefore the quality of the interface description depends on the grid size. Hence, capturing small bubbles requires grid refinement which leads to an increased computational effort. An alternative is to model the small bubbles with a Lagrangian Particle Tracking (LPT) method.

2.2 The LPT method for small bubbles

Small bubbles are modelled as Lagrangian point particles and are tracked by an LPT method in the fluid flow. This method is relevant for particles much smaller than the grid size such that the source terms from the particle can be approximated as a point source. The recommended particle size is usually ten times smaller than the Lagrangian grid size. Arlov *et al*. [5] showed that a particle could fill up to 22% of the Lagrangian cell and still satisfy LPT theory. A particle P is defined by the position of its center, $\mathbf{x_P}$, its diameter, D_p, its velocity, $\mathbf{U_P}$ and its density, ρ_P. Its volume is assumed to be the volume of a sphere $V_p = D_p^3 \pi / 6$ and its mass is $m_p = \rho_P V_P$.
In a Lagrangian frame, the particle position and motion are calculated from

$$\frac{d\mathbf{x_P}}{dt} = \mathbf{U_P} \quad \text{and} \quad m_P \frac{d\mathbf{U_P}}{dt} = \sum \mathbf{F} .$$

Several forces, **F,** are acting on the particle, such as drag, lift, added mass, inertia and buoyancy. In this preliminary study, only the drag force is considered, as

$$\mathbf{F}_D = m_P \frac{\mathbf{U} - \mathbf{U_P}}{\tau_P} , \quad \text{where} \quad \tau_P = \frac{4}{3} \frac{\rho_P D_P}{\rho C_D |\mathbf{U} - \mathbf{U_P}|} \quad \text{is the relaxation time of the particles, i.e. the time it takes for a particle to}$$

respond to changes in the local flow velocity. The drag coefficient C_D for a spherical particle is derived from experimental data (Clift [11]) and depends on the particle Reynolds number $Re_P = \rho\, D_p\, |\mathbf{U} - \mathbf{U_p}| / \mu$, as

$$\begin{cases} C_D = 24 / Re_P & \text{if} \quad Re_P < 0.1 \\ C_D = 24\, (1 + 1/6\, Re_P^{2/3}) / Re_P & \text{if} \quad 0.1 < Re_P < 1000 \\ C_D = 0.44 & \text{if} \quad Re_P > 1000 \end{cases}$$

The force $\mathbf{f_P}$ exerted by a particle on a unit volume of fluid V_{celli} is proportional to the difference in particle momentum between the instant it enters (t_{in}) and leaves (t_{out}) the control volume $cell_i$, as $\mathbf{f_P} \propto m_p\, (\mathbf{U_P}(t_{in}) - \mathbf{U_P}(t_{out}))$. The source term $\mathbf{S}_P$ in eq. (3) is the contribution of this force for each particle P_k which traveled in the control volume $cell_i$ of volume V_{celli}, as

$$\mathbf{S_P}[cell_i] = \frac{1}{V_{cell_i} \Delta t} \sum_k \mathbf{f_{P_k}}$$

2.3 Coupling between VOF and LPT

The new multi-scale approach is based on switching method in order to handle the presence of both large and small structures in a mixture of vapor and liquid. The VOF method is complemented with a two-way coupling LPT method which accounts for the small bubbles on a coarser grid. The multi-scale model requires
- a parameter and a critical value at which the switching between the VOF and LPT methods is activated,
- a strategy to handle the communication between the VOF and LPT methods such that mass and momentum are conserved.

The criterion parameter for switching method is simply related to the grid size limit for which LPT theory is valid. In other words, bubbles with a size small enough to be tracked by LPT are converted to point particles. The strategy is inspired from the technique used by Tomar *et al*. [6] to identify small droplets created during the break-up of a turbulent liquid jet in gas. At each time step, the bubbles described in the Eulerian frame are identified with a so-called *connected components technique*. It consists of associating the adjacent cells for which the volume fraction meets a given criterion. In the case of bubble break up, the condition is that the volume fraction is below a threshold value α_{lim}. The adjacent cells which fulfil this condition are stored together with the number of the bubble (bubbleID) they belong to. The algorithm efficiency is optimized by using a Hash Table which is a table with two parameters, a key and an associated value. Here the key is the cell label and the value is its bubbleID. In this way, it is easy and fast to retrieve data (cell label) because the searching algorithm doesn't use loops which are time consuming. Once the bubble identification is completed, the bubbles which can be handled in the Lagrangian frame because of their small volume are converted to particles. The position, size and velocity of these particles are deduced from the Eulerian data and the corresponding volume fraction is removed from the VOF calculations. The particles are tracked with the LPT method and the influence of the particles on the flow is taken into account through a source term in the Eulerian momentum equation.

The Lagrangian grid is coarser than the Eulerian grid in order to fulfil the condition of validity of the LPT theory. The Lagrangian grid size is arbitrarily set to be four times as large as the Eulerian grid size in each direction. The maximum volume for the bubble handled by the LPT model is set to be 10% of the Lagrangian cell volume. With these assumptions, the bubbles described by less than 6.4 Eulerian cells are candidates for being handled by the LPT method on the Lagrangian grid. These bubbles are small enough to be considered as spherical due to the surface tension. Therefore their diameter is derived from the equivalent volume of a sphere.

The particles are small enough to be considered as source points on the Lagrangian grid. On the other hand, each particle can fill several cells on the Eulerian grid such that the point particle approach may not be valid on the Eulerian grid. However the finer grid is still necessary to obtain accurate results with the VOF method. Therefore the VOF results are interpolated from the Eulerian to the Lagrangian grid. The overall results on the Lagrangian grid give a more realistic description of the whole range of bubble sizes.

The detailed algorithm of this coupling method implemented in the OpenFOAM C++ library is presented in Figure 1 and is illustrated by a 2D example in Figure 2.

1- Create a list (L) of cells whith $\alpha < \alpha_{lim}$.
2- Identify coherent bubbles:
    Initialize bubbleID counter (maxID=0)
    Create a Hash-Table HT which will contain (cell   label, bubbleID)
    For all cell_i $\in$ L
        Create a list (Ln) of neighbours
        If none element of Ln is a key of HT
        $\rightarrow$ Add cell_i's label as a new key in HT, with value bubbleID= maxID
        $\rightarrow$ maxID++
        If only one element of Ln (cell_k) is a key of HT
        $\rightarrow$ Get the value bubbleID_k associated to the key cell_k
        $\rightarrow$ Add cell_i's label as a new key in HT, with value bubbleID= bubbleID_k
        If several elements of Ln (cell_k, k=1,K; K>1) in Ln are keys in HT
        $\rightarrow$ Get the values bubbleID_k, k=1,K associated to the keys cell_k k=1,K
        $\rightarrow$ Find the minimum value minID=min{bubbleID_k, k=1,K}
        $\rightarrow$ Add cell_i's label as a new key in HT, with value bubbleID= minID
        $\rightarrow$ For all elements of Ln with associated value {bubbleID_k, k=1,K}> minID in HT,
            change the value to minID in HT (i.e. cell _i connects bubbles together)
3- For each bubble, get its properties
    Create a list (B) of cell label associated to the same bubbleID in HT
    Evaluate the bubble volume $V_P = \sum_B (1 - \alpha_{cell}) V_{cell}$

    Evaluate the bubble centroid position $\mathbf{x}_P = \frac{1}{V_P} \sum_B \mathbf{x}_{cell} (1 - \alpha_{cell}) V_{cell}$

    Find the lagrangian cell corresponding to the centroid position, get its volume V_{lag}
    If $V_P < V_{lag}/10$ (i.e. the bubble satisfies the criterion for LPT approach)

        $\rightarrow$ Evaluate the bubble velocity $\mathbf{U_P} = \frac{1}{V_P} \sum_B \mathbf{U}_{cell} (1 - \alpha_{cell}) V_{cell}$

        $\rightarrow$ Evaluate the bubble diameter $D_P = (6 V_P / \pi)^{1/3}$

        $\rightarrow$ add the small bubble as a new point particle $P(D_P, \mathbf{x_P}, \mathbf{U_P})$ for the LPT simulation

        $\rightarrow$ delete the corresponding bubble from the VOF simulation $\alpha_{cell \in B} = 1$

Fig. 1 Algorithm for the VOF to LPT coupling

The choice of the threshold value α_{lim} for bubble identification determines the degree of precision and the computational cost of the method. A value α_{lim} close to one means that almost all the cells are retained for the bubble identification. With a lower threshold value, the cells considered for bubble identification are fewer and therefore the computational time is decreased. On the other hand, neglecting the cells with very low gas content may induce errors for the size and the number of structures identified. Therefore a parameter sensitivity study is conducted and the influence of the threshold value on the bubbles distribution and size is presented in the results section.

(a)

Key = Cell label	Value= Bubble ID
4	0
5	0
14	0
15	0
16	0
30	1
33	2
34	2
38	3
39	3
40	1
41	1
42	1
43	

Key = Cell label	Value= Bubble ID
4	0
5	0
14	0
15	0
16	0
30	1
33	1
34	1
38	3
39	3
40	1
41	1
42	1
43	1

(c)

- The coloured cells are identified with α<0.95 (Figure 2.a).
- Set maxID = 0
- March trough the identified cells in increasing order.
- The cell labelled 4 has no neighbour in HT therefore the bubble ID 0 is assigned : put HT(4,0), and maxID is set to 1.
- The cell labelled 5 has one neighbour in HT, with bubbleID=0 therefore the bubble ID 0 is also assigned : put HT(5,0)
…
- The cell labelled 30 has no neighbour in HT therefore the bubble ID 1 is assigned : put HT(30,1), and maxID is set to 2.
…
- The cell labelled 33 has no neighbour in HT therefore the bubble ID 2 is assigned : put HT(33,2), and maxID is set to 3.
…
- The cell labelled 43 has two neighbours in HT. The cell 42 with ID=1 and cell 33 with ID=2. The lowest bubble ID, 1, is assigned : put HT(43,1), and the bubble ID of cells 33 and   34 are set to 1 (Figure 2.c).
…

(b)

Fig. 2 (a) Illustration of the identification of bubbles on a 2D Eulerian grid. (b) Description of the steps to create the HashTable.
(c) Illustration of the HashTable when cell 43 merges two identified bubbles.

3. Results

In order to validate the VOF–LPT coupling method for future application to cavitation modeling, numerical simulations of the breakup of an air bubble in water are performed. The geometrical set-up is shown in Figure 3. It consists of a box filled with water and an air bubble staying on the bottom (i.e. no gravity is included). The grid and fluid properties are given in Table 1.

Case 1 (Figure 3a) is similar to the set-up of the simulations performed by Gopala *et al.* [12] and the experiments of Andersson and Andersson [13] where a water jet impacts the bubble from above. In case 2 (Figure 3b), the same grid is used but the inlet is situated under the air bubble. The direction of the jet velocity is inclined by 30 degrees such that this configuration is a simplified representation of the re-entrant jet which breaks the attached cavity in the context of cloud cavitation.

(a)   **(b)**

Fig. 3 Geometrical set-up (a) case 1, (b) case 2. Inlet is on the top or bottom boundary, outlets are on the sides boundaries and the bubble is a hemisphere.

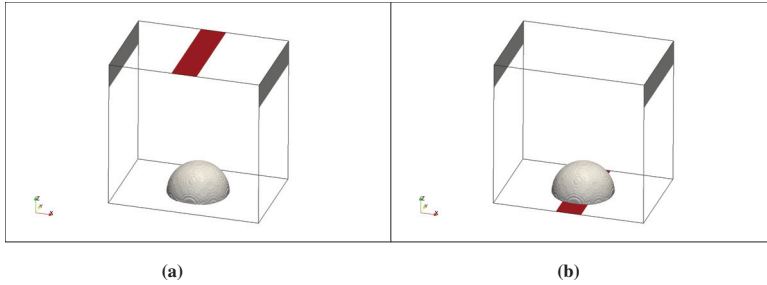| Density [kg/m^{-3}]	$\rho_l = 997$ $\rho_g = 1$
Viscosity [kg/ms]	$\mu_l = 1e^{-5}$ $\mu_g = 2e^{-5}$
Surface tension	0.072
Inlet velocity [m/s]	$|\mathbf{U}| = 0.5$
Dimensions in (x,y,z) direction [m]	$0.03 \times 0.02 \times 0.03$
Number of cells in (x,y,z) direction	$96 \times 64 \times 96$
Inlet dimension in (x,y) direction [m]	0.02×0.005
Outlet dimension in (y,z) direction [m]	0.02×0.005
Bubble diameter [m]	0.01

Table 1 Physical and grid properties

4.1 Case 1

The bubble is stretched under the influence of the jet velocity (Figure 4a). Then the extremities grow and the middle part becomes thinner. Two children bubbles are formed and are linked by a thin strip (Figure 4b). This connecting strip is eventually detached from the two bubbles which continue to move apart from each other. These results are in agreement with both experiments [13] and numerical simulations [12]. In the numerical simulations of Gopala *et al.* [12], the pure VOF method predicted that the connecting strip evolved into two small bubbles. Thanks to the coupling VOF-LPT, the present simulation also capture these two small bubbles and furthermore succeeds to identify a number of even smaller bubbles (Figure 5). This shows a gain of accuracy in the modeling of bubble breakup.
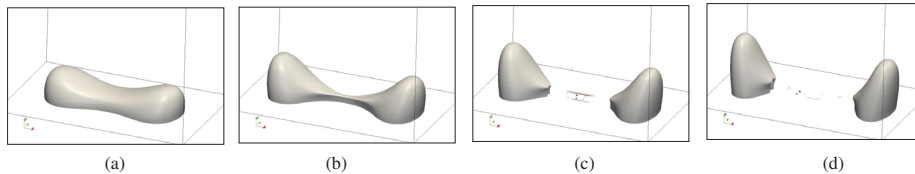

(a)   (b)   (c)   (d)

Fig. 4 Isosurface α=0.5. Instantaneous pictures of the bubble deformation and breakup.
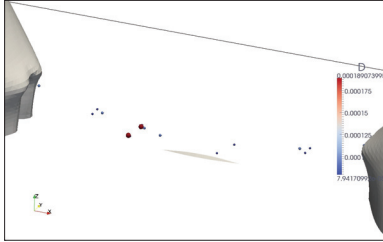
Fig. 5 Close-up of Figure 4d. The two larger bubbles in the sides of the figure are modeled by the VOF method (isosurface α=0.5) and the small bubbles are identified by the coupling method and modeled by the LPT method.

4.2 Case 2

The bubble breakup resulting from a jet impacting the bubble from underneath is illustrated in Figure 6. The presence of small bubbles is successfully captured by the coupling method. The influence of the value of α_{lim} is studied by comparing the results obtained for α_{lim} =0.95 with the results obtained with α_{lim} =0.9 or 0.99. Figure 7 describes the influence of this parameter on the number of bubbles treated by the LPT method as well as their size. When α_{lim} is increased, the method is more accurate and produces more particles and their sizes are smaller. With α_{lim} =0.99, the algorithm accounts also for the cells with a lower gas content, i.e. the cells with $\alpha \in$ [0.95, 0.99[are not neglected, compared to the case α_{lim} =0.95. Such a cell is either isolated or adjacent to cells that belong to identified bubbles. In the first scenario, a particle which has a very small diameter is created from this very low volume of gas. In the second scenario, the cell connects several identified bubbles such that the resulting bubble has a volume which doesn't satisfy LPT theory anymore. Therefore the distinct bubbles which were candidates for the LPT approach when α_{lim} =0.95 are now identified as one large bubble which can still be treated by the Eulerian approach. With α_{lim} =0.9, the cells with a gas content corresponding to α>0.9 are not accounted for, therefore the smallest bubbles are not detected by the algorithm. This parameter study highlights the sensitivity of the identification method to the threshold value α_{lim} which needs further investigations.
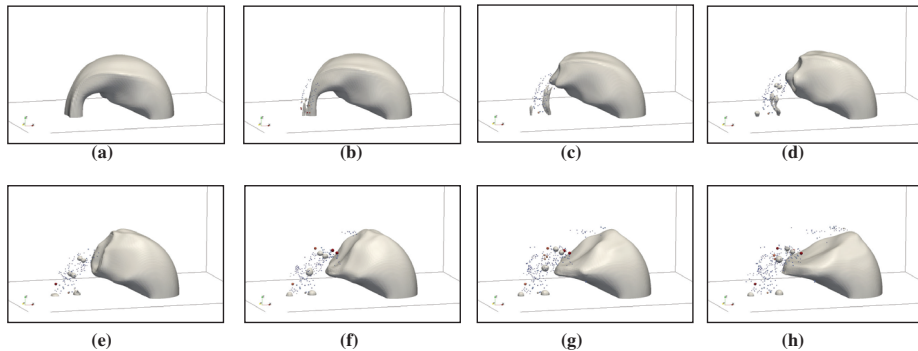

Fig. 6 Instantaneous pictures of the bubble modeled by the VOF method (isosurface α=0.5 colored in grey) and the small bubbles identified by the coupling method and modeled by the LPT method .
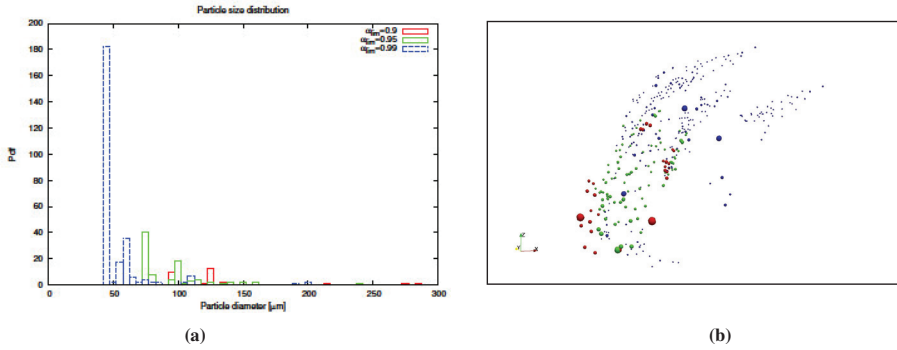
(a)   **(b)**

Fig. 7 Size of the particles for different threshold value α_{lim}, at t=0.0185 which corresponds to Figure 6.d. (a) Probability density function. (b) Snapshot of the particles distribution.

4. Conclusion

Since a model based on the VOF method fails to capture structures that are smaller than the grid size, it cannot model the small cavitation bubbles without investing an enormous computational effort. These bubbles are present in the case of cloud cavitation and influence the global dynamics of the flow. For this type of cavitation, tracking individual bubbles is more relevant. In order to improve the existing mass transfer cavitation models based on the VOF method, a new hybrid method has been developed. This multi-scale approach switches from an Eulerian to a Lagrangian frame in order to account for the small bubbles that a pure VOF method cannot simulate. An algorithm for identifying small bubbles has been implemented in OpenFOAM and the coupling method has been tested on two simple cases of an air bubble breaking up under the impact of a water jet. The second configuration is a simplified model of the re-entrant jet that breaks the attached cavity in the context of a cavitating hydrofoil. The results show the ability of the algorithm to detect small bubbles and track them in the Lagrangian frame. The multi-scale approach is therefore an improvement to the modeling of the transition from sheet to cloud cavitation.

Nomenclature

C_D	Drag coefficient [-]		α	Volume fraction [-]
D	Diameter [m]		κ	Curvature [m^{-1}]
F	Force [N]		μ	Dynamic viscosity [kg m^{-1}s^{-1}]
g	Gravitational constant [ms^{-2}]		ρ	Density [kg m^{-3}]
m	Mass [kg]		σ	Surface tension coefficient [Nm^{-1}]
p	Pressure [Nm^{-2}]			
Re	Reynolds number [-]		l	Liquid (water)
t	Time [s]		g	Gas (vapor or air)
U	Velocity [ms^{-1}]		P	Particle
V	Volume [m^3]			

References

[1] Sauer J. and Schnerr G.H., 2000, "Unsteady cavitating flow- A new cavitating model based on a modified front capturing method and bubble dynamics", Proceedings of 2000 ASME Fluid Engineering Summer Conference.

[2] Kunz, R.F., Boger, D.A., Stinebring, D.R., Chyczewski, T.S., Lindau, J.W., Gibeling, H.J., Venkateswaran, S., and T.R. Govindan, 2000, "A Preconditioned Navier-Stokes Method for Two-Phase Flows with Application to Cavitation Predication", Computers and Fluids, 29, pp. 849-875.

[3] Spång J., 2008, "Indicating Cavitation Using Bubble Dynamics", MSc. Thesis, Uppsala University, Sweden.

[4] Grekula, M., 2010, "Cavitation Mechanisms related to erosion, Studies on Kaplan turbines, foils and propellers", PhD thesis, Chalmers University of Technology, Sweden.

[5] Arlov D., Revstedt J. and Fuchs L., 2007, "A different approach for handling large bubbles in a square cross-sectioned bubble column combining Large Eddy Simulation with Lagrangian Particle Tracking", 6th International Conference on Multiphase Flow.

[6] Tomar G., Fuster D., Zaleski S. and Popinet S., 2010, "Multiscale simulations of primary atomization", Computers & Fluids, 39(10), pp. 1864-1874.

[7] Hirt, C.W. and Nichols, B.D., 1981, "Volume of Fluid (VOF) Method for the Dynamics of Free Boundaries", J. Comp. Phys., Vol. 39, pp. 201-225.

[8] Rusche H., 2002, "Computational fluid dynamics of diversed two phase flows at high phase fraction", PhD thesis, University of London , England.

[9] Brackbill J.U., Kothe D.B.and Zemach C., 1992, "A continuum Method for Modeling surface Tension", J. Comp. Phys., 100, 335-354.

[10] Huuva T., Cure A., Bark G. and Nilsson H., 2007, "Computations of unsteady cavitating flow on wing profiles using a volume fraction method and mass transfer models", Proceedings of   the 2nd IAHR International Meeting of the Workgroup on Cavitation and Dynamical Problems in Hydraulic Machinery and Systems, Scientific Bulletin of the "Polytechnica" University of Timisoara, Romania. Transactions on Mechanics, 52 (66) pp. 21-34.

[11] Clift R., Grace J.R and Weber M.E., 1978, "Bubbles, Drops and Particles", Academic, New York,

[12] Gopala V.R., van Wachem B.G.M. and Andersson B, 2007, "Analysis and Validation of the Breakup of Fluid Particles using Volume of Fluid Method", 6th International Conference on Multiphase Flow.

[13] Andersson, R. and Andersson, B, 2006, "Modeling the breakup of particles in turbulent flows", AIChE Journal, 52(6), pp. 2031-2038

A new multi-scale approach for modelling cavitation on hydrofoils

Aurélia Vallier [1] * , Johan Revstedt [1] and Håkan Nilsson[2]

[1] *Division of Fluid Mechanics Dept. Energy Sciences, Lund University, SE-22100 Lund, Sweden*
[2] *Applied Mechanics, Fluid Dynamics, Chalmers University of Technology, SE-412 96 Gothenburg, Sweden*

SUMMARY

Cavitation on hydrofoils comprises several physical processes. Cavitation nuclei are transported to regions of low static pressure, where they grow and contribute to the formation of large-scale vapour cavities. The large-scale structures may periodically deform and break up into smaller cavitation bubbles. The cavitation bubbles are transported to regions of higher static pressure, where they implode and may erode the material of the hydrofoil.

Large-scale cavitation inception, development and break-up is frequently modelled using the Volume-Of-Fluid (VOF) method together with a mass transfer model for the vaporization and condensation. The VOF method is limited to the modelling of structures that are larger than the computational control volume cell size, and is thus unable to resolve the cavitation nuclei and the small bubbles that break off the large structure. On the other hand, the transport of the cavitation nuclei is frequently modelled using the Discrete Bubble Model (DBM), which tracks spherical bubbles that are much smaller than the cell size. A Rayleigh-Plesset bubble dynamics model may then be used to estimate the evolution of the spherical bubble radius as the surrounding pressure is changing. The DBM approach is thus unable to model the large-scale non-spherical structures.

The present work develops a new multi-scale approach which can model both the small spherical bubbles, the large non-spherical structures, and the transition between those regimes. The principle of the approach is to couple an Eulerian cavitation model (VOF method with a mass transfer model) with a Lagrangian cavitation model (DBM that includes four-way coupling and the Rayleigh-Plesset bubble dynamics model). The approach is tested for the development of an attached cavity on a hydrofoil. The results show that the approach successfully predicts the formation of small bubbles in the attached cavity and the shedding cloud and gives a better description of the mixture of liquid, vapour and gas.
Copyright © 0000 John Wiley & Sons, Ltd.

Received ...

KEY WORDS: Cavitation; mass transfer model; bubble dynamics; new multi-scale approach.

---

*Correspondence to: E-mail: aurelia.vallier@energy.lth.se

Prepared using **fldauth.cls** *[Version: 2010/05/13 v2.00]*

1. INTRODUCTION

In the last decades, numerous numerical cavitation models have been developed to describe the mechanisms of sheet and cloud cavitation on hydrofoils. A sheet cavity is a large attached structure which covers a part of the hydrofoil, while cloud cavitation corresponds to a large number of small bubbles being transported with the flow. The sheet cavity length may oscillate if the rear part is periodically detached from the cavity, and the detached part turns into a cloud of small bubbles. The large-scale cavitation inception, development and breakup is frequently modelled using the Volume-Of-Fluid (VOF) method, with a mass transfer model for the vaporization and condensation [1, 2]. In the mass transfer model developed by Sauer and Schnerr [3], the vaporization is governed by the number of cavitation nuclei per unit volume in the fluid. The cavitation inception is modelled by a linearised Rayleigh-Plesset equation for the rate of growth of the nuclei. Together with an appropriate turbulence model, the dynamic of the flow is well described and the approach successfully predicts the attached sheet cavity, the re-entrant jet which breaks up the cavity, and the shedding process. The part of the cavity that breaks off is however transported downstream as a large coherent structure rather than a cloud of bubbles.

The VOF method is designed to track the interface between two fluids [4]. This method is therefore suitable for modelling large resolvable vapour structures, such as sheet cavitation. The drawback of this method is that it can not describe structures that are smaller than the cell size. It would therefore be very impractical to use VOF to capture the small cavitation bubbles that are present in the case of cloud cavitation, due to the extremely high mesh resolution required. If also the bubble dynamics at the collapse phase is to be resolved by VOF (and in that case also including compressibility effects), the required mesh resolution would rapidly grow out of reach. That is the reason why the VOF method does not give sufficiently accurate results regarding the breakup process when bubble clouds are formed and advected.

In the present work, the VOF method with the Sauer and Schnerr mass transfer model is improved to give a more realistic prediction of the whole range of bubble sizes. Small bubbles are identified from the VOF representation and transferred to a Lagrangian frame. The method for transition from the Eulerian to the Lagrangian frame is inspired from the technique used by Tomar et al. [5] when identifying small droplets created during the breakup of a turbulent liquid jet in gas. The small bubbles are tracked individually with the Discrete Bubble Model and the bubble dynamics is resolved by a Rayleigh-Plesset equation in order to model the collapse of individual bubbles. The interaction between the bubbles is accounted for and the flow is affected by the presence of the bubbles. The bubbles may also be transferred back from the Lagrangian to the Eulerian frame, based on the size of the Lagrangian bubbles or on their distance to the interface of the VOF structures.

The present multi-scale approach thus uses the strength of the VOF method to model the large structures in the Eulerian framework, and the strength of the DBM approach to model the small bubbles in the Lagrangian framework.

2. THE VOF METHOD WITH A MASS TRANSFER CAVITATION MODEL

The Volume-Of-Fluid (VOF) method, introduced by Hirt and Nichols [4], is a numerical technique for tracking the sharp interface between two or more fluid phases. It is useful for modelling large vapour structures and is therefore frequently adopted for modelling sheet cavitation. In VOF, the liquid volume fraction α takes values between 0 to 1 within a computational cell. The interface is defined to exist in the cells with intermediate values. The mixture density ρ and viscosity μ are calculated using the liquid volume fraction α, as

$$\rho = \alpha \rho_l + (1 - \alpha)\rho_v, \tag{1}$$

$$\mu = \alpha \mu_l + (1 - \alpha)\mu_v,$$

where subscripts l and v stand for liquid and vapour. In the mass transfer cavitation model of Sauer and Schnerr [3], the continuity, momentum, and liquid volume fraction transport equations read

$$\nabla \cdot \mathbf{U} = (\frac{1}{\rho_v} - \frac{1}{\rho_l})\dot{m}, \tag{2}$$

$$\frac{\partial \rho \mathbf{U}}{\partial t} + \nabla \cdot (\rho \mathbf{U} \otimes \mathbf{U}) = -\nabla p + \nabla \cdot [\mu(\nabla \mathbf{U} + \nabla \mathbf{U}^T)] + \rho \mathbf{g} - \mathbf{S}_{st} + \mathbf{S}_B, \tag{3}$$

$$\frac{\partial \alpha}{\partial t} + \nabla \cdot (\alpha \mathbf{U}) + \nabla \cdot (\alpha(1 - \alpha)\mathbf{U}_r) = -\frac{\dot{m}}{\rho_l}, \tag{4}$$

where $\mathbf{U}$ and p are the mixture velocity and pressure, respectively. The mass transfer rate, $\dot{m}$, accounts for the destruction and production of water vapour. The source term $\mathbf{S}_{st}$ models the effect of surface tension. According to Brackbill [6], it is expressed as $\mathbf{S}_{st} = \sigma_{st}\kappa\delta\mathbf{n}$, where σ_{st} is the surface tension coefficient, δ is the function that ensures that the force is only applied at the interface ($\delta = |\nabla\alpha|$), $\mathbf{n}$ is the normal vector at the interface ($\mathbf{n} = \frac{\nabla\alpha}{|\nabla\alpha|}$) and κ is the curvature at the interface ($\kappa = -\nabla \cdot \mathbf{n}$). The additional source term $\mathbf{S}_B$ in the momentum equation (3) is due to the influence of the Lagrangian bubbles on the flow. In the volume fraction transport equation (4), the third term on the l.h.s. is an artificial compression term that is active only in the interface region, and where $\mathbf{U}_r$ is the relative velocity between the liquid and the water vapour. This term was introduced by Rusche [7] to preserve the interface sharpness, which is crucial in the VOF approach.

In order to derive the mass transfer rate, $\dot{m}$, Sauer and Schnerr [3] stated that the inception of cavitation is due to the presence and growth of nuclei in the liquid. The nuclei are assumed to be spherical micro-bubbles filled solely with water vapour. These micro-bubbles are supposed to be

uniformly distributed in the liquid and to have the same radius, R_{nuc}. The number of micro-bubbles per unit volume is denoted n_{nuc} and the vapour volume fraction is therefore expressed as

$$(1 - \alpha) = \frac{\frac{4}{3}\pi R_{nuc}^3 n_{nuc}}{1 + \frac{4}{3}\pi R_{nuc}^3 n_{nuc}}. \tag{5}$$

Furthermore, Sauer and Schnerr [3] assumed that the dynamics of each micro-bubble is governed by a simplified Rayleigh-Plesset equation, obtained by neglecting the second-order derivative, the viscosity and the surface tension. The pressure inside the nuclei is the saturated vapour pressure, p_v, and the liquid pressure at the micro-bubble position is set to the local mixture pressure, p. Thus, the nuclei growth rate is given by

$$\dot{R}_{nuc} = sign(p_v - p)\sqrt{\frac{2}{3}\frac{|p_v - p|}{\rho_l}},$$

which yields a mass transfer rate of

$$\dot{m} = \frac{\rho_v \rho_l}{\rho}(1 - \alpha)\alpha \frac{3\dot{R}_{nuc}}{R_{nuc}}. \tag{6}$$

If $p < p_v$, the mass transfer rate is positive, and the source term $-\frac{\dot{m}}{\rho_l}$ is negative in the liquid volume fraction transport equation (4), which corresponds to evaporation.

The results obtained with this model agree well with experimental data for cavitation on hydrofoils, as shown by Huuva et al. [1], Lu [2] and Senocak [8]. Together with an appropriate grid resolution and turbulence model, the dynamic of the flow is well described and the cavitation model predicts the inception, the development into a sheet cavity, the re-entrant jet breaking up the cavity, and the shedding of the breakup process. However, it is unable to predict the generation, transport and dynamics of the small bubbles that eventually collapse and cause strong pressure waves and surface pitting. The detached vapour region shrinks when it comes to a region with higher pressure, but as it is simply predicted as a region of intermediate volume fraction, the collapse of individual bubbles is not represented. As these physical processes are crucial for cavitation erosion prediction, their effect should be included. The present work suggests that bubbles that are too small for the VOF resolution requirements should be transferred to the Lagrangian framework, tracked using DBM, and develop under the Rayleigh-Plesset equation.

3. TRANSITION BETWEEN THE FRAMEWORKS

The present work develops a new multi-scale approach that enables the transfer of bubbles that are too small for the VOF resolution requirements, to the Lagrangian framework and a coarser mesh for the DBM tracking. An overview of the approach is given in section 3.1, while a detailed description of the algotithm, implemented in the OpenFOAM C++ library, is presented in Appendix A. The requirements and the methodology for transferring the Lagrangian bubbles back to the Eulerian frame, are discussed in section 3.2

3.1. Lagrangian bubble detection

The strategy used to identify the bubbles is inspired from the technique used by Tomar et al. [5] when identifying small droplets created during the breakup of a turbulent liquid jet in gas. At each time step, the droplets are identified with a so-called connected components technique. It consists in associating the adjacent cells for which the liquid volume fraction meets a given criterion. The size of the coherent liquid structures can be estimated and small structures are transformed into droplets. In the case of breakup of vapour structures, the condition used for the connected components technique is that the cell contains vapour, i.e, the liquid volume fraction is below a threshold value, $\alpha_{lim} < 1$. The adjacent cells that fulfill this condition are stored together with the number of the bubble (bubbleID) they belong to. The algorithm efficiency is optimized by using a hash table, which is a table with two parameters; a key and an associated value. Here the key is the cell label and the value is its bubbleID. In this way, it is easy and fast to retrieve data (cell label) because the search algorithm does not use time consuming loops. Once the bubble identification is completed, the bubbles that are too small to be resolved by VOF are converted to Lagrangian bubbles. The minimum number of connected cells required to represent the smallest vapour structure is denoted N_{E-L}. Thus, it is assumed that a VOF vapour structure that occupies less than N_{E-L} Eulerian cells is a candidate for being handled in the Lagrangian frame. The position, $\mathbf{x}_B$, radius, R, and velocity, $\mathbf{U}_B$, of the identified Lagrangian bubbles are deduced from the Eulerian representation, from which the corresponding vapour volume fraction is removed. The bubbles are considered small enough to be spherical due to the surface tension, and their diameters are thus derived from the equivalent volume of a sphere. Bubbles of that size does not fulfill the DBM requirement that the bubble should be smaller compared to the cell size, on the mesh used in the Eulerian representation (referred to as the Eulerian mesh). The Lagrangian bubbles are thus tracked on a much coarser Lagrangian mesh.

The choice of the threshold value, α_{lim}, for bubble identification determines the accuracy and the computational cost of the detection method. A value close to one means that almost all the cells are retained for the bubble identification. With a lower threshold value, the cells considered for bubble identification are fewer and therefore the computational time is decreased. On the other hand, neglecting the cells with very low vapour content may induce errors for the size and the number of structures identified. The influence of the threshold value on the bubble distributions and sizes was investigated in a previous work [9].

3.2. Transfer of the Lagrangian bubble to the Eulerian frame

A bubble described in the Lagrangian frame may become very large. It can happen after a coalescence event or due to an explosive growth when the bubble is subjected to a pressure lower than its critical pressure. Bubbles that are too large for the DBM requirements, or large enough to be tracked by VOF, should be moved to the Eulerian framework. The criterion for this is that the

bubble has a volume larger than a group of N_{L-E} neighbouring Eulerian cells, where the innermost cell hosts the bubble centroid. The threshold value N_{L-E} is a model parameter that is chosen larger than N_{E-L}. Thus, the Lagrangian bubbles can grow, and it is possible to capture the collapse and rebounds following the growth phase.

The transition from Lagrangian to Eulerian also happens when a bubble comes close enough to the Eulerian isosurface where $\alpha = 0.5$. The method to determine if a bubble is close to an Eulerian isosurface consists in estimating the location of the Lagrangian bubble surface at the six points with coordinates $(x_B \pm R, y_B \pm R, z_B \pm R)$. If $\alpha \leq 0.5$ in any of those points, the Lagrangian bubble is in contact with a resolved vapour structure, and is converted to the Eulerian representation.

The method for the conversion from Lagrangian to Eulerian framework consists in filling with vapour the Eulerian cell hosting the centroid $\mathbf{x}_B$ and some of its neighbours. The number of cells concerned depends on the volume V_B and also on the volume available in these cells that can be converted into vapour. A detailed description of this method is given in Appendix C.

4. LAGRANGIAN BUBBLE MODELLING

In the discrete bubble model (DBM), a bubble is considered as a point source when modelling its transport in the surrounding fluid and it is modelled as a finite volume sphere when modelling its dynamics, the interactions with the flow, solid surfaces and other bubbles. These features are presented in detail here.

4.1. Bubble motion

In a Lagrangian frame, each bubble position vector $\mathbf{x}_B$ is calculated from the equation

$$\frac{d\mathbf{x}_B}{dt} = \mathbf{U}_B, \tag{7}$$

and the motion of each bubble is governed by Newton's second law

$$m_B \frac{d\mathbf{U}_B}{dt} = \mathbf{F}_a + \mathbf{F}_p + \mathbf{F}_{buoy} + \mathbf{F}_{drag} + \mathbf{F}_{lift}. \tag{8}$$

The forces acting on the bubble are the added mass force, the pressure gradient force, the buoyancy force, the drag force and the lift force.

$$\mathbf{F}_a = \tfrac{1}{2}\rho\tfrac{m_B}{\rho_B}\left(\tfrac{D\mathbf{U}}{Dt} - \tfrac{d\mathbf{U}_B}{dt}\right),$$

$$\mathbf{F}_p = -\tfrac{m_B}{\rho_B}\nabla p,$$

$$\mathbf{F}_{buoy} = m_B(1 - \tfrac{\rho}{\rho_B})\mathbf{g},$$

$$\mathbf{F}_{drag} = C_{drag}\rho\frac{m_B}{\rho_B}\frac{3}{8R}(\mathbf{U} - \mathbf{U}_B)|\mathbf{U} - \mathbf{U}_B|,$$

$$\mathbf{F}_{lift} = C_{lift}\rho\frac{m_B}{\rho_B}(\mathbf{U} - \mathbf{U}_B) \times \omega.$$

Empirical relations of drag, lift and added mass effect for spherical non-rotating particles are considered in this model. $\frac{D\mathbf{U}}{Dt}$ is the total acceleration of the fluid as seen by the bubble. $\mathbf{g}$ is the gravitational acceleration. The vorticity of the fluid is $\omega = \nabla \times \mathbf{U}$ and C_{lift} is the lift coefficient, assumed to take the value 0.5 according to Auton [10]. The drag coefficient C_{drag} depends on the bubble Reynolds number

$$\mathrm{Re}_B = \frac{2\rho R|\mathbf{U} - \mathbf{U}_B|}{\mu}.$$

For very small Reynolds number (≤ 0.1), the drag coefficient is $C_{drag} = \frac{24}{Re_B}$. For larger Reynolds number it is estimated by an empirical law [11], given by

$$C_{drag} = \frac{24}{Re_B}\left(1 + 0.15Re_B^{0.687}\right) \ \text{ for } 0.1 < Re \leq 1000,$$

$$= 0.44 \ \text{ for } Re > 1000.$$

4.2. Bubble dynamics

A bubble, B, identified for being handled in the Lagrangian frame is small enough to be considered as a spherical bubble of radius $R(t)$. Its rate of growth and its interface acceleration are denoted $\dot{R} = \frac{dR(t)}{dt}$ and $\ddot{R} = \frac{d^2R(t)}{dt^2}$. The density ρ_B and the internal pressure $p_B(t)$ are assumed to be uniform inside the bubble. It is assumed that the fluid in the far field is composed of water and a certain amount of non-condensable gas. This gas is present in any fresh water and corresponds to small bubbles of air that did not have time to diffuse or to travel up to the free surface. The presence of non-condensable gas is neglected in the Eulerian frame, since the nuclei are solely composed of vapour in the Sauer and Schnerr model. It is however included in the present work, when the bubbles are modelled in the Lagrangian frame, because its presence has a crucial role at the last stage of a collapse. Indeed, the gas ensures that a collapsing bubble can not disappear, i.e. $R(t) > 0$. It implies that the collapse phase ends when the compression stops and is followed by a rebound of the bubble. Thus, this approach does not account for the possibility that a Lagrangian bubble may disappear or split into smaller bubbles upon collapse.

A bubble, B, identified with the connected component technique has a volume V_B and its centroid is located at the position $\mathbf{x}_B$. It is subjected to the mixture pressure p, interpolated at the location $\mathbf{x}_B$. It is assumed that in the far field, where the liquid pressure is the constant reference pressure p_0, this bubble will be in equilibrium ($\dot{R} = \ddot{R} = 0$) and it contains only gas. The corresponding equilibrium radius is R_0 and its mass is $m_{g0} = \frac{4}{3}\pi R_0^3 \rho_{g0}$ where ρ_{g0} is the density of air at pressure p_0. It is assumed that the mass of the non-condensable gas is constant during the evolution of the

bubble size. Therefore each Lagrangian bubble contains a volume V_v of water vapour to which is artificially added an amount of non-condensable gas whith a constant mass.

During its trajectory, the Lagrangian bubble is affected by the mixture pressure which evolves with space and time. It acts as a disturbance on the bubble stability and influences the radius of the bubble $R(t)$. The bubble dynamics is modelled by the Rayleigh-Plesset [12] equation

$$R\ddot{R} + \frac{3}{2}\dot{R}^2 = \frac{1}{\rho}\left[p_B(t) - 4\mu\frac{\dot{R}}{R} - \frac{2\sigma_{st}}{R} - p(\mathbf{x}_B, t)\right], \qquad (9)$$

where the pressure inside the bubble, $p_B(t)$, is the sum of the saturated vapour pressure p_v and the gas pressure $p_g(t)$. It is related to the gas pressure p_{g0} at the equilibrium state, (R_0, p_0), as $p_g(t) = p_{g0}\left(\frac{R_0}{R(t)}\right)^{3\gamma}$. Moss [13] suggested to use different values for the polytropic coefficient γ during the process of growth and collapse. The bubble growth phase preceding a collapse is sufficiently slow to be assumed isothermal and during this process, when $R \geq R_0$, γ is unity. On the other hand, the collapse occurs within an extremely short time, therefore the compression of gas is assumed adiabatic during this phase and γ takes the value of the ratio of the heat capacities of the gas, $\gamma = 1.4$, when $R < R_0$. Writing equation (9) at the equilibrium state, (R_0, p_0), the gas pressure p_{g0} is expressed as

$$p_{g0} = p_0 + \frac{2\sigma_{st}}{R_0} - p_v. \qquad (10)$$

In practice, the known parameters when solving equation (9) are the initial radius R, the initial mixture pressure interpolated at the location $\mathbf{x}_B$ and the reference pressure p_0. It is important to make sure that the bubble is initially in equilibrium in order to avoid unphysical oscillations at the early stage of bubble lifetime. As shown in a previous work [14], it is necessary to determine the equilibrium radius R_0 corresponding to the reference pressure p_0 that satisfies the condition

$$R_0^{3\gamma} + \frac{2\sigma_{st}}{p_0 - p_v}R_0^{3\gamma-1} + \frac{R^{3\gamma}}{p_0 - p_v}\left(p_v - \frac{2\sigma_{st}}{R} - p(\mathbf{x}_B, t)\right) = 0. \qquad (11)$$

When the bubble grows, the contribution of the vapour is included for the calculation of the bubble mass. However, during a collapse, when $R(t) \leq R_0$, it is assumed that the mass is solely due to the non-condensable gas. Therefore the mass of the bubble is evaluated as

$$m_B(t) = \begin{cases} m_{g0} & \text{if } R(t) \leq R_0, \\ m_{g0} + \rho_v(V_B(t) - V_g(t)) & \text{if } R(t) > R_0. \end{cases} \qquad (12)$$

Here V_B is the total volume of the bubble, the volume of gas is $V_g = m_{g0}/\rho_g$ and ρ_g is obtained from $p_g/\rho_g^\gamma = p_{g0}/\rho_{g0}^\gamma$. When solving for the bubble dynamics, the pressure $p(\mathbf{x}_B, t)$ in equation (9) is the mixture pressure interpolated at the centroid position if the bubble is smaller than the host cell in the Eulerian mesh. If the bubble is larger than this cell, the pressure, p, in equation (9) is calculated as the average of the liquid pressures interpolated at the Eulerian cells containing the bubble volume. This yields a more realistic approximation of the forces over the bubble surface.

4.3. Bubble-flow interaction

The influence of the Lagrangian bubbles on the flow is taken into account through the source term S_B in the momentum equation (3). According to the Lagrangian theory, a momentum source contribution is generated by a Lagrangian bubble in each cell visited along its path. Each bubble B_i which is in a cell $cell_k^0$ of volume V_k^0 generates a contribution during a time specific to this bubble, $\Delta t_{k,i}$. Thus, the contribution of all bubbles B_i, $i = 1 : I$, crossing the cell $cell_k^0$ is commonly written as

$$\mathbf{S}_B[cell_k^0] = \frac{-1}{V_k^0} \sum_{i=1}^{I} m_{B_i} \frac{\Delta \mathbf{U}_{B_i}}{\Delta t_{k,i}}. \tag{13}$$

In the present work, the multi-scale approach is performed on two grids. The Lagrangian bubbles are tracked on a coarse Lagrangian mesh, and their influence on the flow is accounted for in a finer Eulerian mesh. In the Lagrangian mesh, the cell hosting the bubble centroid is $cell_B$ and it contains several Eulerian cells, as shown in Figure 1(a). Applying the source term at the center of $cell_B$ or at the center of all the Eulerian cells inside $cell_B$ yields erroneous results, as shown by Arlov et al. [15]. In the Eulerian mesh, the cell hosting the bubble centroid is $cell_k^0$. If the volume of the bubble is smaller than $cell_k^0$, then equation (13) is accurate. However, if the volume of the bubble is larger than $cell_k^0$, then the point-particle theory is violated in the Eulerian frame. This shortcoming is a common issue when modeling Lagrangian bubbles in a turbulent flow because both approaches imply conflicting assumption on the grid size. The point-particle theory requires that the cells are much larger than the bubbles while the turbulent modelling requires very small cells. In order to account for the fact that the bubble is not a point-particle but has a finite volume, the contribution S_B is also distributed in the neighbouring Eulerian cells of $cell_k^0$, $\{cell_k^j, j = 1 : J\}$, yielding

$$\mathbf{S}_B[cell_k^j] = \frac{-1}{V_k^j} \sum_{i=1}^{I} m_{B_i} \frac{\Delta \mathbf{U}_{B_i}}{\Delta t_{k,i}} H(\mathbf{x}_B - \mathbf{x}_k^j) \text{ for } j = 0 : J \tag{14}$$

where $\mathbf{x}_k^j$ is the center of cell $cell_k^j$ and the function H is a Gaussian function centred in $\mathbf{x}_B$ with variance R,

$$H(\mathbf{x}_B - \mathbf{x}_k^j) = \frac{1}{(R\sqrt{2\pi})^3} exp\left(-\frac{1}{2}\left[\frac{|\mathbf{x}_k^j - \mathbf{x}_B|}{R}\right]^2\right). \tag{15}$$

If the contribution is applied to the cells that fulfill $|\mathbf{x}_B - \mathbf{x}_k^j| < 3R$, then 99.9% of the source term is distributed with this approach. However, in order to limit the computational cost of this method, the neighbouring cells $\{cell_k^j, j = 1 : J\}$ are restricted to those that share a vertex with $cell_k^0$, as shown in Figure 1(b). This choice is still more accurate than if S_B was only applied in $cell_k^0$ because it accounts for the finite volume of the bubble.
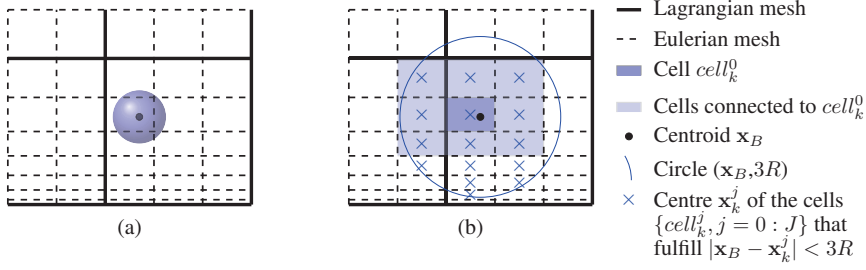
Figure 1. (a) Lagrangian bubble, Lagrangian and Eulerian mesh. (b) The source term S_B is applied in the coloured Eulerian cells. The circle with center $\mathbf{x}_B$ and radius $3R$ showing the zone of influence of the function $H(\mathbf{x}_B - \mathbf{x}_k^j)$ for $|\mathbf{x}_B - \mathbf{x}_k^j| < 3R$, in 2D.

4.4. Bubble-wall interaction

A bubble colliding with a wall either bounces, sticks or slides depending whether inertia or dissipation dominates the process. Experiments show the presence of a liquid film between the bubble and the wall at collision [16]. Zenit [17] showed that the behavior of a bubble colliding with a wall is different from that of a solid sphere due to the liquid film and the bubble deformation. It was found that the coefficient of restitution ϵ_w depends on the capillary number $Ca = \frac{\mu_l U^{0n}}{\sigma_{st}}$ and the modified Stokes number $St^* = \frac{(\rho_B + \frac{1}{2}\rho_l)2RU^{0n}}{9\mu_l}$, it reads

$$\epsilon_w = e^{-30\sqrt{Ca/St^*}}.$$

In practice, an impact with a wall is modeled when the bubble trajectory crosses a face f_w of the wall boundary. Neglecting the actual flattening of the bubble when it approaches a surface boundary, it is assumed that a collision occurs when the distance from the spherical bubble center to the center of the face is equal to the bubble radius. Denoting the normal and tangential unit vectors of f_w as $\mathbf{n}_w$ and $\mathbf{t}_w$, respectively, the bubble velocity before the impact is written as

$$\mathbf{U}_B^0 = U_B^{0n}\mathbf{n}_w + U_B^{0t}\mathbf{t}_w.$$

The normal component of the bubble velocity after the impact is evaluated as $U_B^n = -\epsilon_w U_B^{0n}$ and the tangential component is unchanged as friction is neglected.

The Eulerian mesh used to compute the fluid flow is chosen fine enough to capture the flow details and it is refined in the vicinity of the wall in order to resolve the boundary layer. The tracking of the bubbles is done on a coarser mesh to ensure that the condition for wall collision is fulfilled. Wall collisions are properly modelled solely for bubbles with their centroid located in a cell connected to the wall surface. This implies that the bubble radius has to be smaller than the wall-normal edges of the Lagrangian host cell connected to the wall, even when the initially small bubbles grow up

to several orders of magnitude. Therefore, a mesh that is coarser in the wall-normal direction is necessary to resolve properly the wall collision events.

4.5. Bubble-bubble interaction

In order to reduce the cost of collision detection, collision partners are searched in the vicinity of each bubble. In the present work, the bubble motion is solved together with the bubble dynamics which requires very small time steps. This implies that the bubbles travel only a small fraction of a Lagrangian cell per time step. Therefore there is no loss of accuracy in limiting the search for the collision partners to the Lagrangian owner cell $cell_B$ and its neighbours that are closest to $\mathbf{x}_B$. As shown in Figure 2, these neighbours are sharing the vertex of $cell_B$ that is the closest to the centroid position $\mathbf{x}_B$. A deterministic model for collision detection and its outcome are described in Appendix B.
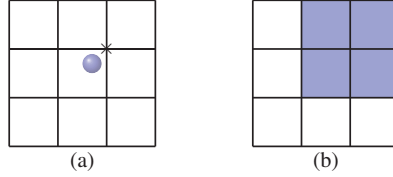

(a) (b)

Figure 2. (a) Lagrangian bubble and vertex (symbol $\times$) of $cell_B$ closest to the bubble centroid. (b) Lagrangian cells (coloured) selected for searching collision partner, in 2D.

4.6. Pressure wave

The main purpose of the multi-scale approach is to include the prediction of the dynamics of the small bubble as they are transported with the flow. The pressure emitted by a collapsing bubble, and the distance of the bubble from the solid surface, are important features for estimating the collapse intensity and its damaging effects. Therefore, the pressure of the acoustic wave radiated by the bubble collapse, p_a, is studied. It is estimated by Mettin et al. [18] as

$$p_a(r) = \frac{\rho}{r}(R^2\ddot{R} + 2R\dot{R}^2),\tag{16}$$

where $r \geq R$ is the distance from the center of the bubble.

5. TEST CASE AND NUMERICAL SET-UP

The multi-scale approach is tested for the cavitating flow past a NACA0015 hydrofoil, with an angle of attack of 8 degrees. Figure 3(a) shows the Eulerian and Lagrangian computational domains, while Figure 3(b) shows the Lagrangian mesh. The hydrofoil has a chord length (and a span-wise width) c_0=0.15 m, and is positioned at $4.5c_0$ from the inlet and $9c_0$ from the outlet of the Eulerian domain. The height of this computational domain is $9c_0$. The Eulerian mesh is clustered to the hydrofoil surface such that the first cell center is on average positioned at $y^+ = 3$, and the expansion ratio is 1.05. In the span-wise direction, 50 grid points are equally distributed. Wall boundary conditions are applied on the back and front of the domain. The uniform inlet velocity is $\mathbf{U}_{in} = 8$ m/s. The reference pressure, $p_0 = 40.7$ kPa, is the liquid pressure of the undisturbed flow, i.e. the value imposed at the outlet boundary. The Reynolds number based on c_0 and $\mathbf{U}_{in}$ is $1.2 \cdot 10^6$. The nuclei concentration is set to $n_{nuc} = 10^8$ nuclei/m^3 water and the nuclei size is set to $R_{nuc} = 10^{-6}$ m which yields an initial vapour volume fraction $(1 - \alpha) \sim 4 \cdot 10^{-10}$.

The attached cavity shown in Figure 4 is obtained from an LES simulation with the Smagorinsky model, and the original mass transfer model of Sauer and Shnerr [3]. These results are used as initial conditions when applying the multi-scale approach. The purpose is to identify the Lagrangian bubbles and model their dynamics in the region where the re-entrant jet breaks up the sheet cavity. Therefore, the Lagrangian domain needs to cover only the cavitating zone, and it is chosen smaller than the Eulerian domain, as shown in Figure 3(a). The Lagrangian bubbles are expected to appear in the recirculation zone, where the cloud is detached from the sheet cavity. Furthermore, the Lagrangian approach is not suitable at the leading edge, where the Eulerian description is more adapted for predicting the inception of the attached cavity. Therefore, the transition from the Eulerian to the Lagrangian description is limited to the region downstream the leading edge, $x > \frac{1}{15}c_0$. The plane $x = \frac{1}{15}c_0$ is shown in Figure 3(b) together with the Lagrangian mesh. The points of the Lagrangian mesh on the hydrofoil surface are distributed identically to the Eulerian mesh such that the curvature of the hydrofoil surface in not altered. The mesh is coarser downstream the hydrofoil for simplicity, and in the normal direction in order to satisfy the requirement for bubble-wall collision. The parameters used for the bubble detection and the framework transitions are $\alpha_{lim} = 0.95$, $N_{E-L} = 5$ and $N_{L-E} = 27$. The choice for N_{L-E} is due to the restriction used in the present work for distributing S_B in the 27 cells around the bubble centroid, as explained in section 4.3. It simplifies also the implementation of the algorithm for the transition from the Lagrangain to the Eulerian frame because only the host cell and its closest neighbours need to be considered for being filled with vapour.
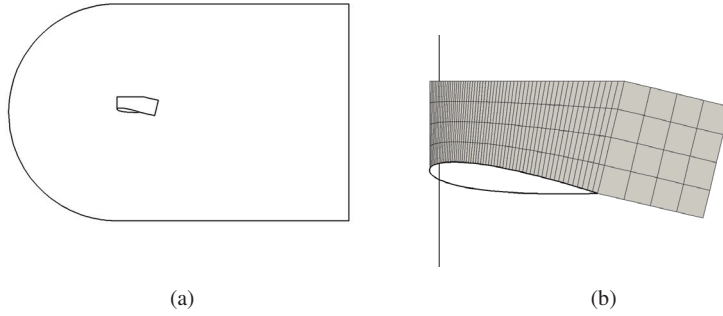
Figure 3. (a) The Eulerian and Lagrangian domain. (b) The Lagrangian mesh and the plane $x = \frac{1}{15}c_0$.
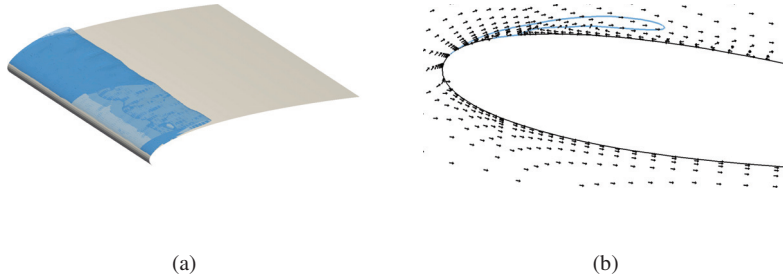

Figure 4. Attached cavity obtained with the original model of Sauer and Shnerr [3], at $t = 0.006$ s which is the initial time for the computations with the multi-scale approach. (a) Isosurface $\alpha = 0.5$. (b) Isosurface $\alpha = 0.5$ and vector plot in the middle plane $z = \frac{1}{2}c_0$.

The multi-scale approach is applied to three different cases. The first case includes the full approach described in this work, i.e. a four-way coupled DBM that accounts for the bubble interactions, their influence on the flow and their interaction with the Eulerian description (Case 4wc). In order to investigate the importance of these features on the results, computations are also performed for one way coupling (Case 1wc), and without the conversion from the Lagrangian to the Eulerian framework (Case 1wc⋆).

6. RESULTS

In section 6.1, the effects of the bubble-bubble and bubble-flow interactions, as well as the transfer of the Lagrangian bubbles back to the Eulerian frame, are studied in order to clarify their importance in the multi-scale approach. In section 6.2, the behavior of the Lagrangian bubbles is investigated for Case 1wc⋆. The radius, trajectories and collapse properties are presented in order to predict the regions that are the most exposed to erosion.

6.1. Sensitivity of different parts of the model

Figure 5(a)-(b) shows that the multi-scale model successfully identifies Lagrangian bubbles in all cases. Bouncing and coalescence events are few, even when the total number of Lagrangian bubbles present in the domain is several hundreds (see Figure 6(a)-(b)). The number of Lagrangian bubbles increases at each time step for $t \in [8, 13]$ ms, and the computational time spent for finding the collision partners is increased whereas it results in few collisions. Occasionally, two or three collision events are detected within one time step. The computation applying the one-way coupling algorithm is 2.5 times faster (Case 1wc compared to Case 4wc in Table I).

For Case 1wc, the number of bubbles decreases at t∼0.014 s and t∼0.017 s, due to successive conversions of Lagrangian bubbles into the Eulerian frame. However, Figure 6(c) shows that at each time step, a maximum of two Lagrangian bubbles are converted to VOF, while the computational time is more than three time higher with this method (Case 1wc⋆ compared to Case 1wc in Table I).

At $t = 0.013$ s, the same amount of Lagrangian bubbles is present in the domain for all cases. However, Figure 7(a) shows that their spatial distribution differs. On the other hand, at t=0.019 s, there are less bubbles for Case 1wc compared to Case 1wc⋆ (Figure 5(b)) while the bubble distributions are in good agreement in Figure 7(b).

These results show that both the 4-way coupling method and the transition from Lagrangian to Eulerian approach are computationally expensive and their impact on the results accuracy needs further investigations. The instant and location of the inception of the first Lagrangian bubbles are compared for each case. It suggests that the first bubble that is created in Case 4wc affects locally the flow and thus, the inception of the following Lagrangian bubbles. Therefore, the discrepancies observed in the shape of the attached cavity and the Lagrangian bubble distributions (Figures 5(a)-(b) and 7) may rather be attributed to the bubble-flow interactions than to the bubble-bubble interactions or their removal from the Lagrangian framework.

In order to estimate the importance of the bubble interactions in the model, the number of bubbles that are overlapping another bubble is calculated a posteriori, for the Case 1wc⋆. It gives an estimation of the error introduced when the bubble interactions are neglected. Similarly, the number of bubbles located inside a VOF structure are sampled in order to estimate the importance of the

Table I. Computational time for the three different cases. The case denoted 1wc⋆ corresponds to one-way coupling without transition from Lagrangian to Eulerian frame.

t [s]	Case 4wc [h]	Case 1wc [h]	Case 1wc⋆ [h]
[0.0061, 0.0129]	326	119	35
[0.0129, 0.0189]	-	255	72
[0.0189, 0.0325]	-	-	216

model for the transition from the Lagrangian to the Eulerian framework. The results in Figure 8 show that a large numbers of bubbles overlap while the number of bubbles inside the VOF structures is negligible. The observed locally dense concentration of bubbles implies that the bubble interaction must be taken into account. Moreover, the importance of the influence of the bubbles on the flow is confirmed because a localy dense suspension enhances the production or dissipation of turbulence [19].

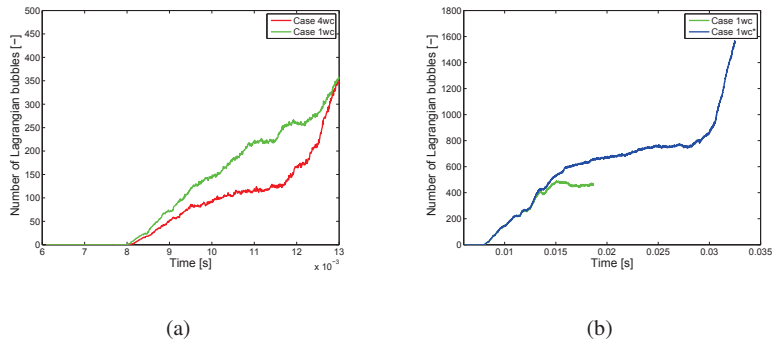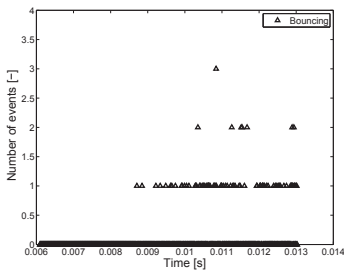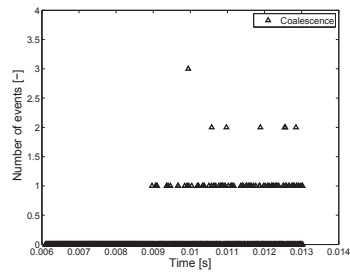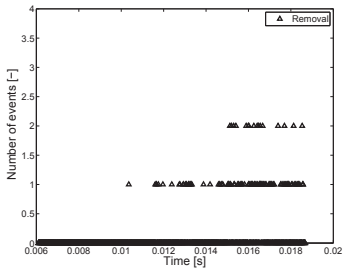(a)   (b)

Figure 5. Number of Lagrangian bubbles present in the domain for different cases.

(a)

(b)

(c)

Figure 6. (a)-(b) Collision events treated for the case 4wc, i.e. four way coupling. (c) Removal events (conversion from Lagrangian bubble to the VOF description) treated for the case 1wc, i.e. one way coupling.
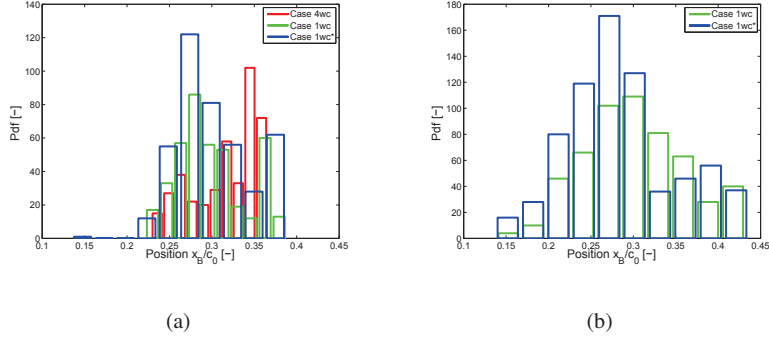
(a)

(b)

Figure 7. Probability density function of the position of the Lagrangian bubbles,
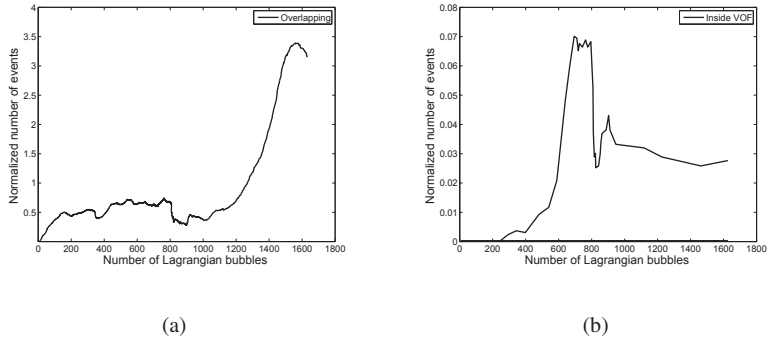at (a) t=0.013 s, and (b) t=0.019 s.

(a)

(b)

Figure 8. (a) Number of overlapping Lagrangian bubbles ($|\mathbf{x}_{Bi} - \mathbf{x}_{Bj}| < (R_i + R_j)$) normalized with the
total number of bubbles in the domain at each time step.
(b) Number of Lagrangian bubbles inside a VOF structure ($\alpha[cell[\mathbf{x}_B]] < 0.5$) normalized with the total
number of bubbles in the domain at each time step. Case 1wc⋆, i.e. one way coupling without transition
from Lagrangian to Eulerian frame, for t∈[0.0061, 0.0325].

6.2. Erosion prediction

The algorithm for the one-way coupling approach without the transition from Lagrangian to Eulerian is fast enough for studies of the evolution of the Lagrangian bubbles when the cloud of vapour is transported downstream the attached cavity. Despite the lower accuracy in this case due to the absence of the bubble interactions and their influence on the flow, as stressed above, the following study gives an overview of the results that can be obtained with the new cavitation model.

Figure 9 shows instantaneous pictures of the attached cavity and the shedding cloud described in the Eulerian frame as well as the Lagrangian bubbles. The bubbles first appear where the re-entrant jet breaks off the attached cavity. Then they are transported upstream with the re-entrant jet. Further on, they are either trapped in the recirculation zone, or continue downstream with the detached cloud of vapour. These trajectories are illustrated in Figure 10(a)-(b) for two different bubbles that are created under very similar conditions, at almost the same position and within a small interval of time. For these bubbles, the radius and the pressure emitted, $p_a(R)$, are shown in Figure 10(c)-(f). The trajectory combined with the pressure emitted are important features for estimating the region that are the most exposed to erosion. For instance, the bubble that stays near the leading edge (left column) is located very close to the hydrofoil surface and emits large peak pressure during its rebounds. On the other hand, the bubble that follows the shedding cloud (right column) yields less direct damages on the solid surface because it undergoes weaker rebounds and is further away from the hydrofoil surface.

Figure 11 shows the location of the Lagrangian bubbles at the end of their first collapse. They occur mainly near the leading edge, especially close to the center line ($z \in [0.37c_0, 0.5c_0]$, denoted zoneCL), and also near the front wall ($z \in [0.9c_0, c_0]$, denoted zoneFW). These results are also shown in Figure 12(a), where the probability density function of the first collapse against the position x_B highlights the region exposed to erosion due to the successive collapses, $x_B \in [0.1c_0, 0.7c_0]$. Most of the first collapses occur close to the surface of the hydrofoil, $\delta \in [0, 0.04c_0]$ (Figure 12(b)). The pdf are also sampled in the regions zoneCL and zoneFW. The trend observed on Figure 12(a)-(b) are emphasized in the region zoneCL, where all the collapses occurs close to the leading edge ($x_B < 0.3c_0$) and 50% of them happen in the first cells near the hydrofoil surface ($\delta < 0.005c_0$). However, near the front wall, the collapses are distributed along two third of the length of the hydrofoil (Figure 12(c)). In this region, the collapses may damage the front wall, and the probability density function is therefore sampled against the distance to this wall, δ_w (Figure 12(d)).

The strength of the multi-scale approach lies in giving information about the location and the intensity of the collapses which are damaging the solid surfaces. However, post-processing the properties $\{\mathbf{x}_B(t), R(t), p_a(r, t)\}$ of each Lagrangian bubbles is expensive in terms of computational

time and memory. It is therefore necessary to find an efficient way to estimate the regions that are the most exposed to the successive collapses and rebounds. For instance, the residence time of the Lagrangian bubbles gives a good prediction of erosion risk. Indeed, Figure 13 shows that the regions where the bubbles stay and rebound are similar to the regions zoneCL and zoneFW which host the largest number of first collapse (Figure 11 and 12). The darker region is therefore the most exposed to erosion as it was observed that the intensity of the rebounds increased with time in this region (Figure 10(e)). Furthermore, it appears that, for the time range of the present simulations, the bubble stay mostly in the recirculation zone, where the pressure is lower and the collapses are stronger.
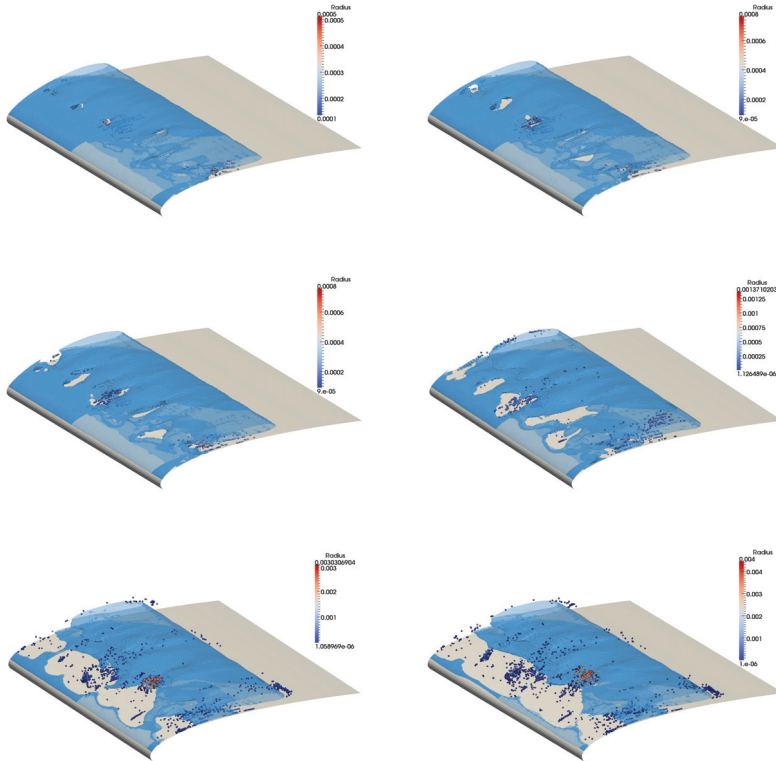

Figure 9. Instantaneous picture of the Eulerian isosurface $\alpha = 0.5$ and the Lagrangian bubbles obtained with the multi-scale approach. Case 1wc, i.e. one way coupling without transition from Lagrangian to Eulerian frame.
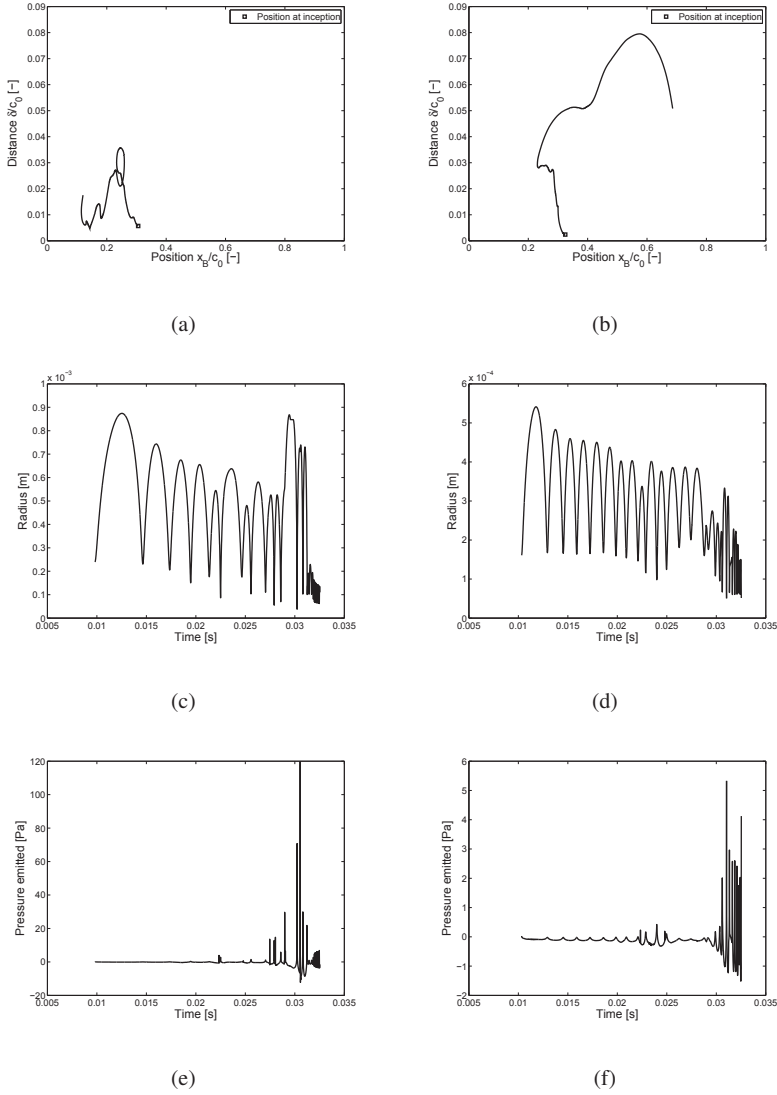
Figure 10. Temporal evolution of two Lagrangian bubbles that are created almost at the same position and time. (a)-(b) Trajectory, δ is the distance to the hydrofoil. (c)-(d) Radius. (e)-(f) Acoustic pressure emitted during the collapses at the bubble surface, $p_a(R)$.
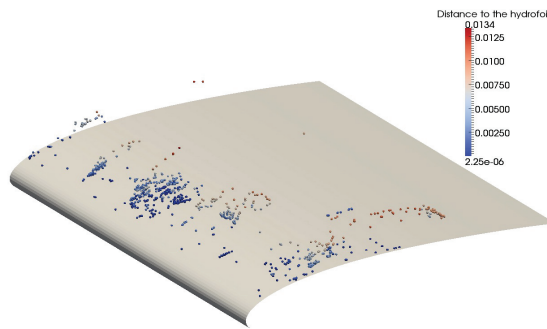
Figure 11. Position of the Lagrangian bubbles recorded at first collapse. Case 1wc⋆, i.e. one way coupling without transition from Lagrangian to Eulerian frame, for t∈[0.0061, 0.0325].
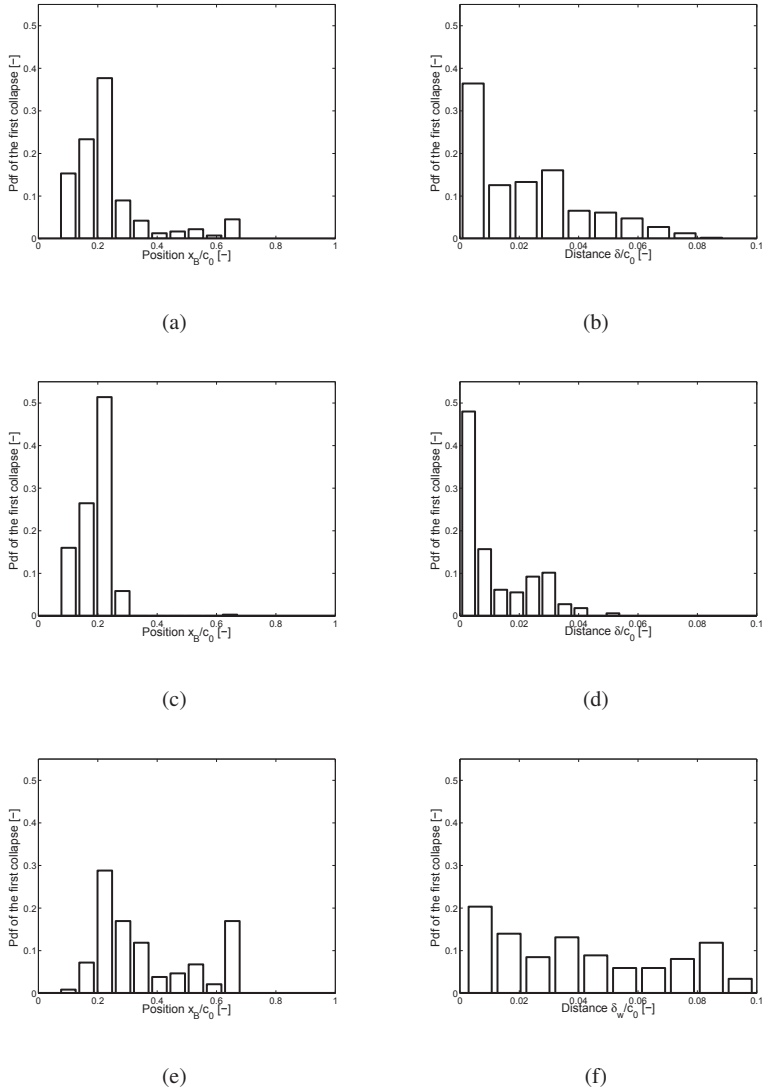
(a)

(b)

(c)

(d)

(e)

(f)

Figure 12. Normalized probability density function of the position of the Lagrangian bubbles when their first collapse occurs. (a)-(b) Results over the whole domain $z \in [0, c_0]$. (c)-(d) Results for the region zoneCL, $z \in [0.37c_0, 0.5c_0]$. (e)-(f) Results for the region close to the front wall, zoneFW, $z \in [0.9c_0, c_0]$. The figures on the left depict the position along the x-axis normalized with the chord length c_0. The figures on the right column depict the distance to the hydrofoil (δ) and front wall (δ_w) normalized with the chord length c_0. Case 1wc$\star$, i.e. one way coupling without transition from Lagrangian to Eulerian frame, for t$\in$[0.0061, 0.0325] s.
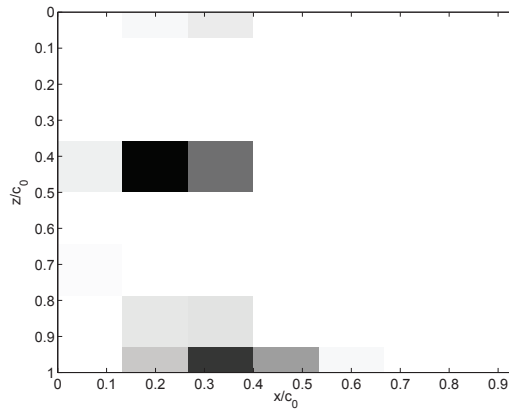
Figure 13. Residence time of the Lagrangian bubbles shown on the hydrofoil surface and coloured from the highest value in black to the lowest in white. Case 1wc⋆, i.e. one coupling without transition from Lagrangian to Eulerian frame, for t∈[0.0061, 0.0325] s.

7. CONCLUSION

Since a model based on the VOF method fails to describe structures that are smaller than the cell size, it can not model the small cavitation bubbles without investing an enormous computational effort. These bubbles are present in the case of cloud cavitation and influence the global dynamic of the flow. For this type of cavitation, tracking individual bubbles is more relevant. In order to improve the existing mass transfer cavitation model based on the VOF method, a new multi-scale method has been developed. This multi-scale approach switches from an Eulerian to a Lagrangian frame in order to account for the small bubbles that a pure VOF method can not simulate. An algorithm for identifying Lagrangian bubbles have been implemented in OpenFOAM. The bubble dynamics is resolved using the Rayleigh-Plesset equation. The collision events are described by a deterministic model, the bubbles affect the flow, and the transition from the Lagrangian to the Eulerian frame is included. The multi-scale approach is applied to a cavitating hydrofoil and describes the re-entrant jet that breaks the attached cavity and yields the formation of Lagrangian bubbles. The importance of the bubble influence on the flow and the bubble interactions are highlighted by comparing the bubble distributions and the cavity shape for different cases. The bubble locations at their first collapse, the bubble trajectories, and the pressure wave emitted during the collapses and rebounds are crucial features for predicting erosion damages on the hydrofoil surface. However, these features, presented here, are computationally expensive to post-process. A more efficient approach consists in studying the residence time of the bubbles, which gives a good estimation of the regions exposed to successive collapses and rebounds. The multi-scale approach is therefore an improvement to the modelling of the transition from sheet to cloud cavitation and the modelling of cavitation erosion risk.

NOMENCLATURE

Roman symbols

m   Mass [kg]

n   Unit normal vector [−]

p   Pressure [Nm^{-2}]

R   Radius [m]

t   Time [s]

U   Velocity [ms^{-1}]

V Volume [m^3]

x   Position [m]

Greek symbols

α Liquid volume fraction [−]

γ Polytropic coefficient $[-]$

μ Dynamic viscosity $[\mathrm{kgm^{-1}s^{-1}}]$

ρ Density $[\mathrm{kgm^{-3}}]$

σ_{st} Surface tension coefficient $[-]$

Subscripts

B bubble

g Non-condensable gas

l Liquid water

nuc Nuclei (vapour inclusion)

v Water vapour

REFERENCES

1. Huuva T, Cure A, Bark G and Nilsson H. Computations of unsteady cavitating flow on wing profiles using a volume fraction method and mass transfer models *Proceedings of the 2nd IAHR International Meeting of the Workgroup on Cavitation and Dynamical Problems in Hydraulic Machinery and Systems, Scientific Bulletin of the "Polytechnica" University of Timisoara, Romania. Transactions on Mechanics* 2007; **52**(66): 21-34 .

2. Lu N-X. Modelling Cavitation Mechanisms Using LargeEddy Simulation. *PhD. Thesis, Chalmers University of Technology, Sweden* 2013.

3. Sauer J and Schnerr GH. Unsteady cavitating flow- A new cavitating model based on a modified front capturing method and bubble dynamics. *Proceedings of 2000 ASME Fluid Engineering Summer Conference* 2000.

4. Hirt CW and Nichols BD. Volume of Fluid (VOF) Method for the Dynamics of Free Boundaries. *J. Comp. Phys.* 1981; **39**: 201-225.

5. Tomar G, Fuster D, Zaleski S and Popinet S. Multiscale simulations of primary atomization. *Computers & Fluids* 2010; **39**(10):1864-1874.

6. Brackbill JU, Kothe DB and Zemach C. A continuum Method for Modeling surface Tension. *J. Comp. Phys.* 1992; **100**: 335-354.

7. Rusche H. Computational fluid dynamics of dispersed two phase flows at high phase fraction. *PhD thesis, University of London , England* 2002.

8. Senocak I. Computational methodology for the simulation of turbulent cavitating flows. *PhD. thesis, University of Florida* 2002.

9. Vallier A, Revstedt J and Nilsson H, Procedure for the break-up of cavitation sheet. *4-th International Meeting on Cavitation and Dynamic Problems in Hydraulic Machinery and Systems, Belgrade, Serbia* 2011.

10. Auton TR. The lift force on a spherical body in a rotational flow. *J. Fluid Mech* 1987; **183**: 199-218.

11. Schiller L and Nauman AZ. A drag coefficient correlation. *Ver. Deut. Ing.* 1993; **77**: 318-320.

12. Plesset MS and Prosperetti A. Bubble dynamics and cavitation. *Annu. Rev. Fluid. Mech.* 1977; **9**: 145-185.

13. Moss WC, Levantin JL and Szeri AJ. A new damping mechanism in strongly collapsing bubbles. *Proceedings Mathematical, Physical and Engineering Sciences* 2000; **456**: 2983-2994.

14. Vallier A, Revstedt J and Nilsson H. Modelling of bubble dynamics related to cavitation. *Submitted to Int. Journal of Multiphase Flow* 2013

15. Arlov D, Revstedt J and Fuchs L. A different approach of handling large bubbles in a square sectioned bubble column combining large eddy simulation with lagrangian particle tracking *Proceedings of the 6th International Conference on Multiphase Flow* 2007.

16. Podvin B, Khoja S, Moraga F and Attinger D. Model and experimental visualizations of the interaction of a bubble with an inclined wall. *Chemical Engineering Science* 2008; **63**:1914-1928.

17. Zenit R and Legendre D, The coefficient of restitution for air bubbles colliding against walls in viscous liquids. *Phys. Fluid* 2009; **21**.

18. Mettin R, Akhatov I, Parlitz U, Ohl CD and Lauterborn W. Bjerknes forces between small cavitation bubbles in a strong acoustic field. *Physical review* 1997; **56**(3).

19. Elghobashi S, An updated classification map of particle-laden turbulent flows. *Proceedings of the IUTAM Symposium on Computational Multiphase Flow* 2006; 3-10.

20. Allen MP, Frenkel D and Talbot J. Molecular dynamics simulation using hard particles. *Comput. Phys. Rep.* 1989; **9**: 301-353.

21. Duineveld PC. Bouncing and coalescence of two bubbles in water. *PhD. thesis, University of Twente, the Netherlands* 1994.

22. Chesters AK, The modeling of coalescence processes in fluid-liquid dispersions - a review of current understanding. *Trans. I. Chem. E 69 (part A)* 1991; 353-361.

23. Sommerfeld M, Bourloutski E and Bröder D. Euler/Lagrange calculations of bubbly flows with consideration of bubble coalescence. *Can. J. Chem. Eng.* 2003; **81**: 508-518.

24. Chesters AK and Hofman G. Bubble coalescence in pure liquids. *Appl. Sci. Res.* 1982; **38**: 353-361.

A. COUPLING METHOD FROM EULERIAN TO LAGRANGIAN FRAME.

The algorithm of the coupling method implemented in the OpenFOAM C++ library is presented in detail.

- Create a list (L) of cells that contains vapour. i.e. with $\alpha < \alpha_{lim}$.
- Identify coherent bubbles:

    1. Initialize bubbleID counter (maxID=0).
    2. Create a Hash-Table HT that will contain the couples (cell label, bubbleID).
    3. For all cell$_i \in$ (L), create a list (Ln) of neighbours.
        (a) If none element of (Ln) is a key of HT,
            i. Add cell$_i$ label as a new key in HT, with value bubbleID= maxID,
            ii. Increment maxID.
        (b) If only one element of (Ln), (cell$_k$), is a key of HT,
            i. Get the value bubbleID$_k$ associated to the key cell$_k$,
            ii. Add cell$_i$ label as a new key in HT, with value bubbleID= bubbleID$_k$.

(c) If several elements of (Ln), (cell$_k$, k=1:K; K¿1), are keys in HT

    i. Get the values bubbleID$_k$, k=1:K associated to the keys cell$_k$, k=1:K,

    ii. Find the minimum value minID=min(bubbleID$_k$, k=1:K),

    iii. Add cell$_i$ label as a new key in HT, with value bubbleID= minID.

    iv. For all elements of (Ln) with associated value bubbleID$_k$¿ minID in HT, change the value to minID in HT (i.e. cell$_i$ connects bubbles together)

- For each coherent bubble identified, get its properties:

  1. Create a list (L_B) of cell labels cell$_j$, j=1:J, associated to the same bubbleID in HT.

  2. If $J < N_{E-L}$ (i.e. the bubble is too small to be described by the Eulerian approach),

    (a) Evaluate the bubble volume on the Eulerian mesh, $V_B = \sum_j (1 - \alpha[cell_j]) V[cell_j]$.

    (b) Evaluate the bubble centroid position $\mathbf{x}_B = \frac{1}{V_B} \sum_j \mathbf{x}[cell_j](1 - \alpha[cell_j]) V[cell_j]$.

    (c) Evaluate the bubble velocity $\mathbf{U}_B = \frac{1}{V_B} \sum_j \mathbf{U}[cell_j](1 - \alpha[cell_j]) V[cell_j]$.

    (d) Evaluate the bubble radius $R = \left(\frac{3V_B}{4\pi}\right)^{\frac{1}{3}}$.

    (e) Add the bubble in the Lagrangian cloud.

    (f) Delete the corresponding bubble from the VOF simulation, $\alpha[cell_j] = 1$, j=1:J.

B. BUBBLE-BUBBLE INTERACTIONS

A deterministic model for collision detection and its outcome are described here. The subscript B, related to the Lagrangian bubble properties, is dropped here for simplicity.

B.1. Collision detection

Consider a bubble pair with respective radius R_1 and R_2, respective initial velocities $\mathbf{U}_1^0$ and $\mathbf{U}_2^0$, and at a distance $\mathbf{x}_1^0 - \mathbf{x}_2^0 = d_{12}^0 > (R_1 + R_2)$ from each other. The final positions are denoted $\mathbf{x}_1$ and $\mathbf{x}_2$. The purpose of the model is to determine if collision can occur within the time dt. Let bubble 2 be the new coordinate reference system, then bubble 2 has relative velocity $\mathbf{U}_{22} = 0$ and bubble 1 has velocity $\mathbf{U}_{12} = \mathbf{U}_1^0 - \mathbf{U}_2^0$
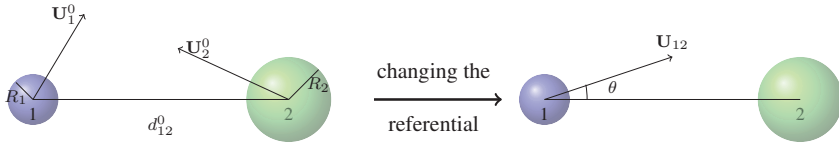

Figure 14. From general referential to the referential with bubble 2 as centre.

The angle between line (1,2) and $\mathbf{U}_{12}$ is denoted θ.

$$\cos\theta = \frac{\mathbf{U}_{12}}{|\mathbf{U}_{12}|} \cdot \frac{\mathbf{x}_2^0 - \mathbf{x}_1^0}{|\mathbf{x}_2^0 - \mathbf{x}_1^0|}$$

If $\cos\theta < 0$ then the bubbles are obviously moving apart. However in the case $\cos\theta > 0$, there exists a critical value θ_c such that if $\theta < \theta_c$ then the collision is possible.
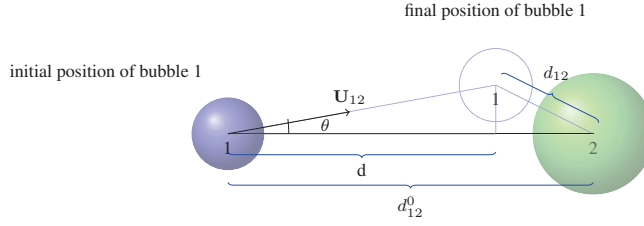
Figure 15. The distance d is the projection on the line (1,2) of the distance traveled by the bubble 1 with respect to the bubble 2.

The distance d is the projection on line (1,2) of the distance traveled during the time step dt, as sketched in figure 15 :

$$d = |\mathbf{U}_{12}| \cos \theta dt$$

Then bubble 1 should travel long enough during this time step to impact bubble 2. So there exists also a critical distance d_c such that if $d > d_c$ then the collision occurs. Collision occurs if $d_{12} < R_1 + R_2$ where d_{12} is the final distance between bubble 1 and 2. In the new reference system, the initial and final positions of the bubbles are $(x_2^0, y_2^0) = (x_2, y_2) = (0, 0)$, $(x_1^0, y_1^0) = (-d_{12}^0, 0)$ and $(x_1, y_1) = (x_1^0 + d, y_1^0 + d \tan \theta)$. Therefore the distance between bubble 1 and 2 is

$$d_{12} = \sqrt{(-d_{12}^0 + d)^2 + (d \tan \theta)^2}$$

And the condition for collision is

$$\sqrt{(-d_{12}^0 + d)^2 + (d \tan \theta)^2} < (R_1 + R_2)$$

which is equivalent to

$$(1 + \tan^2 \theta)d^2 - 2d_{12}^0 d + (d_{12}^0)^2 - (R_1 + R_2)^2 < 0$$

The distance d is solution of the equation of the 2nd degree in d, $f(d) = 0$ with

$$f(d) = (1 + \tan^2 \theta)d^2 - 2d_{12}^0 d + (d_{12}^0)^2 - (R_1 + R_2)^2$$

This equation has no solution if there is no collision (i.e. if $\theta > \theta_c$), see Figure 16(a). When the angle θ is decreased until $\theta = \theta_c$, the bubbles become tangent (see figure 16(b)) and the equation has one solution. If $\theta < \theta_c$, then there is a collision and the trajectory of the bubble is such that they really meet each other. They first impact and then they overlap. The first intersection is the smallest root of the equation. The overlapping period corresponds to the interval for which $f(d) < 0$ and the second root corresponds to the moment when the bubbles would leave each other if they didn't interact (see figure 16(c)).

The determinant of the equation $f(d) = 0$ is

$$\Delta = \left(2d_{12}^0\right)^2 - 4\left(1 + \tan^2 \theta\right)\left((d_{12}^0)^2 - (R_1 + R_2)^2\right)$$

- For $\Delta = 0$, we obtain $\theta = \theta_c$

$$(d_{12}^0)^2 - \left(1 + \tan^2 \theta_c\right)\left((d_{12}^0)^2 - (R_1 + R_2)^2\right) = 0$$
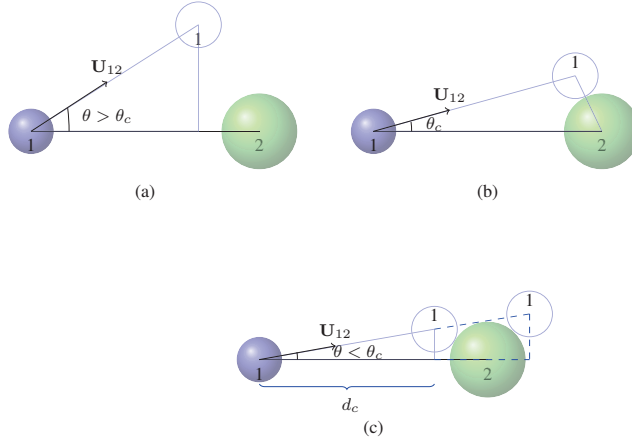
Figure 16. Different cases for the bubble pair interaction. (a) the angle $\theta > \theta_c$ and there is no collision, (b) $\theta = \theta_c$ and bubble 1 is tangent to bubble 2, (c) $\theta < \theta_c$, there is collision.

$$\tan \theta_c = \frac{R_1 + R_2}{\sqrt{(d_{12}^0)^2 - (R_1 + R_2)^2}}$$

$$\theta_c = \arctan \left(\frac{R_1 + R_2}{\sqrt{(d_{12}^0)^2 - (R_1 + R_2)^2}} \right)$$

There is one solution

$$d_c = \frac{d_{12}^0}{(1 + \tan \theta_c^2)} = \frac{\left(d_{12}^0\right)^2 - (R_1 + R_2)^2}{d_{12}^0}$$

- For $\Delta > 0$, i.e. $\theta < \theta_c$, there are 2 solutions

$$\frac{2d_{12}^0 \pm \sqrt{\Delta}}{2 \left(1 + \tan^2 \theta\right)}$$

The smallest root is in $[0, d_{12}^0]$ and it is the critical distance d_c for this collision:

$$d_c = \frac{d_{12}^0 - \sqrt{\left(d_{12}^0\right)^2 - (1 + \tan \theta^2)\left(\left(d_{12}^0\right)^2 - (R_1 + R_2)^2\right)}}{(1 + \tan \theta^2)}$$

This collision detection algorithm consists in finding the possible binary collision partner of bubble 1 (i.e. $\theta < \theta_c$ and $d \geq d_c$) at the end of the Lagrangian time step dt specific to bubble 1. The limitation is that the bubble considered can collide only once during this time step. The inherent inaccuracy of this time driven method is assumed to be negligible when using a sufficiently small time step. A more rigorous approach would be to list all the possible collisions during this time step, sort them in a priority list and treat the first occurring collision, update all the bubble at the time of this event and repeat these four steps until the end of the Lagrangian time step. In that case, it is appropriate to evaluate the collision time t_c instead of the critical distance of collision. This is simply done by using $d = U_{12} \cos \theta dt$ such that f(d)=0 becomes an equation of

the second degree in t, for which the solution is

$$t_c = \frac{d_{12}^0 U_{12} \cos\theta - \sqrt{(d_{12}^0 U_{12} \cos\theta)^2 - (U_{12})^2 \left(\left(d_{12}^0\right)^2 - (R_1 + R_2)^2\right)}}{(U_{12})^2}$$

This approach is widely used in the field of molecular dynamics [20]. However the computational cost of such a event driven method is extremely high and this approach doesn't appear relevant for the present model.

B.2. Collision outcome

The outcome of a collision between a bubble pair is either bouncing or coalescence depending on two parameters: the size of the bubbles and the collision speed. Experimental results [21] suggest that coalescence is enhanced when both parameters have a small value. This corresponds to a small Weber number. The Weber number based on the equivalent diameter, $D_{eq} = \frac{4R_1 R_2}{R_1 + R_2}$, is given by

$$We_{eq} = \frac{\rho |\mathbf{U}_{B2}^n - \mathbf{U}_{B1}^n|^2 D_{eq}}{2\sigma_{st}}, \tag{17}$$

where the collision speed is $|\mathbf{U}_{B2}^n - \mathbf{U}_{B1}^n|$, and $\mathbf{U}_{Bi}^{0n}$ is the normal component of the velocities before impact, as shown in Figure 17.
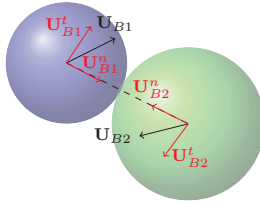

Figure 17. Decomposition of the velocities into normal and tangential components.

The theoretical models that have been developed to predict the coalescence efficiency (i.e. the probability that a collision results in coalescence) are based on the observation that a liquid film is trapped between the bubbles at impact [22, 23]. The bubbles coalesce if the liquid film has time to drain during the time the bubble pair interacts. The outcome of collision is therefore assumed to be a function of two time-scales: the interaction time t_i and the drainage time t_d. The resulting coalescence probability for a head-on collision is theoretically $P_c = 0$ if $t_i < t_d$ and $P_c = 1$ if $t_i \geq t_d$. In order to account for the the fact that the collision may not be frontal, a smooth semi-empirical function is used [22], and the coalescence probability is expressed as $P_c = e^{-t_d/t_i}$. If a uniform random number in the range [0,1] becomes smaller than the coalescence probability then coalescence occurs, otherwise bouncing happens. According to Chester [24], the time-scales are given by $t_i = \left(\frac{\rho D_{eq}^3}{16\sigma_{st}}\right)^{\frac{1}{2}}$ and $t_d = \frac{\rho |\mathbf{U}_{B2}^n - \mathbf{U}_{B1}^n| D_{eq}^2}{8\sigma_{st}}$. Thus, the probability is given by

$$P_c = e^{-\sqrt{\frac{We_{eq}}{2}}}. \tag{18}$$

The effects of a collision on the bubble pair are described here, for both bouncing and coalescence.

B.2.1. Bouncing In the case of bouncing, the momentum and trajectory of both bubbles are altered. It is assumed that bubble deformation and friction are neglected in the present work. Using the notations of Figure 17, the unit normal vector is given by

$$\mathbf{n}_{12} = \frac{\mathbf{x}_{B2}^0 - \mathbf{x}_{B1}^0}{|\mathbf{x}_{B2}^0 - \mathbf{x}_{B1}^0|},$$

and the velocity normal components are expressed as

$$\mathbf{U}_{Bi}^{0n} = (\mathbf{U}_{Bi}^0 \& \mathbf{n}_{12}) \cdot \mathbf{n}_{12}.$$

The normal component of the velocities after impact changes according to

$$\mathbf{U}_{Bi}^n = \frac{m_{Bi}\mathbf{U}_{Bi}^{0n} + m_{Bj}\mathbf{U}_{Bj}^{0n} - m_{Bj}\epsilon(\mathbf{U}_{Bi}^{0n} - \mathbf{U}_{Bj}^{0n})}{m_{Bi} + m_{Bj}}, \tag{19}$$

where ϵ is the coefficient of restitution, and the tangential component is unchanged after collision when friction is neglected.

B.2.2. Coalescence In the case of coalescence of two bubbles, 1 and 2, a new bubble is formed with properties R, $\mathbf{x}_B$ and $\mathbf{U}_B$. Conservation of mass, momentum and energy yields

$$R = \left(R_1^3 + R_2^3\right)^{\frac{1}{3}},$$

$$\mathbf{x}_B = \frac{m_{B1}\mathbf{x}_{B1} + m_{B2}\mathbf{x}_{B2}}{m_{B1} + m_{B2}},$$

$$\mathbf{U}_B = \frac{m_{B1}\mathbf{U}_{B1} + m_{B2}\mathbf{U}_{B2}}{m_{B1} + m_{B2}}.$$

The equilibrium radius R_0 for this new bubble, is evaluated with equation (11).

C. COUPLING METHOD FROM LAGRANGIAN TO EULERIAN FRAME.

The detailed algorithm of the coupling method implemented in the OpenFOAM C++ library is presented.

- Find the Eulerian cell, $cell_k$, hosting the centroid position.
- Determinate the volume of liquid of this cell $V_{dispo} = \alpha[cell_k]V[cell_k]$.
- If $V_{dispo} \geq V_B$, fill only the hosting cell :
    1. Update the liquid volume fraction, $\alpha[cell_k] = \alpha[cell_k] - V_B/V[cell_k]$
- Otherwise, fill the hosting cell and its neighbours:
    1. Update the liquid volume fraction, $\alpha[cell_k] = \alpha[cell_k] - V_{dispo}/V[cell_k]$.
    2. The remaining volume of vapour to be converted in the Eulerian frame is
        $V_{B,left} = V_B - V_{dispo}$.
    3. Fill the neighbour cells $cell_j$ until $V_{B,left} = 0$:
        (a) Determinate the volume of liquid of the neighbour cell $cell_j$,
            $V_{dispo}^j = \alpha[cell_j]V[cell_j]$
        (b) Update the liquid volume fraction,
            $\alpha[cell_j] = \alpha[cell_j] - min(V_{dispo}^j, V_{B,left})/V[cell_j]$.
        (c) Update the remaining volume of vapour to be converted in the Eulerian frame,
            $V_{B,left} = V_{B,left} - min(V_{dispo}^j, V_{B,left})$.